SCALING UP SARDON CATCHMENT GROUNDWATER RECHARGE INTO *DEHESA* (*MONTADO*) HARD ROCKS OF IBERIAN PENINSULA

YONAS WELDAY TEKLE
WREM: s6025471
February, 2017

SUPERVISORS:
Dr. X. Chen (Xuelong)
Dr. Maciek W. Lubczynski

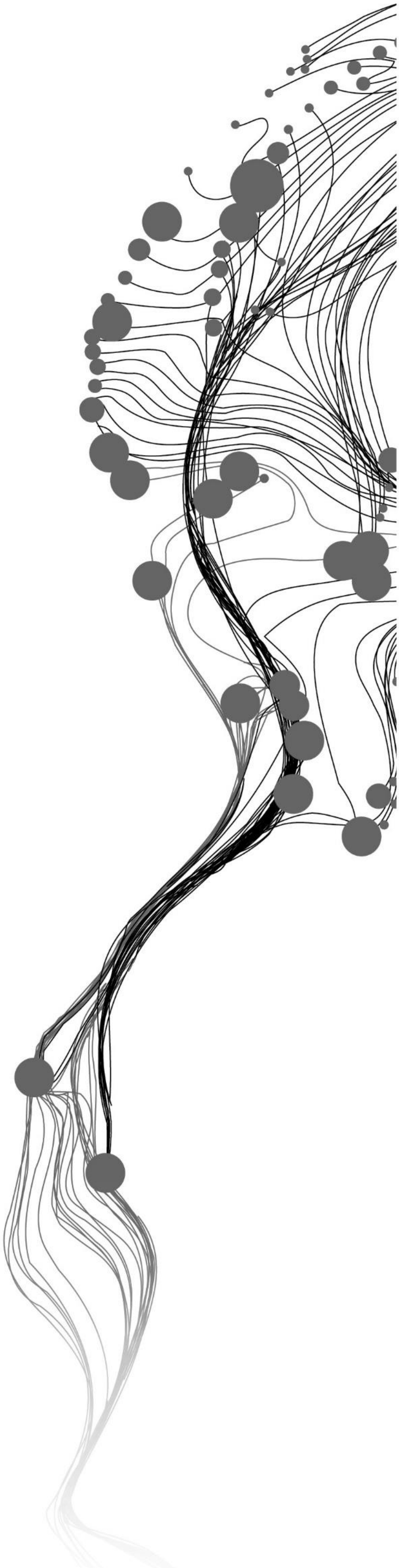

SCALING UP SARDON CATCHMENT GROUNDWATER RECHARGE INTO *DEHESA* (*MONTADO*) HARD ROCKS OF IBERIAN PENINSULA

YONAS WELDAY TEKLE
WREM: s6025471

Enschede, The Netherlands, February, 2017

Thesis submitted to the Faculty of Geo-Information Science and Earth Observation of the University of Twente in partial fulfilment of the requirements for the degree of Master of Science in Geo-information Science and Earth Observation.
Specialization: [Name course (e.g. Applied Earth Sciences)]

SUPERVISORS:
Dr. X. Chen (Xuelong)
Dr. Maciek W. Lubczynski

THESIS ASSESSMENT BOARD:
Dr. Ing. T.H.M. Rientjes (Chair)
Dr. Yaping, Liu (External Examiner, College of Resource Environment and Tourism, Capital Normal University)

ABSTRACT

Groundwater in water-limited hard rock environments of the Iberian Peninsula, is a vital resource and its recharge assessment is important in the analysis of water resources replenishment. The recharge assessment is difficult due to heterogeneities and anisotropies of such aquifers and due to large spatiotemporal variability of rainfall and evapotranspiration.

This study aimed at scaling up daily net recharge (*Rn*) of the pilot Sardon Catchment (SC) area (80 km2) into the large water limited Dehesa-Montado Hard Rock (DMHR) area (141,430 km2), with combination of satellite-based daily rainfall (*Psat*) and daily evapotranspiration (*ETsat*). The remote sensing *Psat* was obtained from Climate Hazards Group InfraRed Precipitation with Station Data (CHIRPS) while the remote sensing *ETsat* from Land Surface Analysis Satellite Application Facility (LSA-SAF). The *Rn* for scaling up was derived by updating the existing transient calibrated SC model applying spatiotemporally variable model inputs (year 2011 to 2013), and a similar simulation that has been tested for the year 2014. Various correlations between Rn and different combinations of satellite-based water fluxes (*Psat*, *ETsat*) or potential recharge (PR = *Psat* -*ETsat*) were tested.

The daily *Rn* was scaled up from SC into DMHR area by applying a multivariate nonlinear regression with *Psat* and *ETsat*. That regression resulted in R^2 = 0.63. The scaled, spatiotemporally variable Rn of the DMHR area has high spatiotemporal variability. The mean annual *Rn* in years 2011 to 2014 ranges from -3.9 mm $year^{-1}$ to 35.3 mm $year^{-1}$. Spatially, the *Rn* generally increase from east to west and is the lowest in the southern parts of the study area mainly because the rainfall is the lowest in that area. The dry season *Rn* is generally negative, ranging from -28.4 mm to -23.9 mm. The wet season *Rn* is positive ranging from 59.2 mm to 24.5 mm. This revealed that the *Rn* in the DMHR is generally low, and it occurs in the wet season.

Key words: Hard rocks, dehesa (montado), Iberian Peninsula, groundwater, spatiotemporal recharge, transient model simulation, scaling up, net recharge, groundwater fluxes, and satellite-based flux inputs.

THIS WORK IS DEDICATED TO MY BELOVED FAMILY

ACKNOWLEDGEMENTS

Praise be to the name of the almighty God for giving me health, strength, wisdom and filling my heart with hope to successfully complete this research. I also thank God for giving me the "International Christian Fellowship (ICF)" that was a place to worship Him and nourish myself spiritually, while I'was away from home.

I would like to address my gratitude to the Joint Japan/World Bank Graduate Scholarship Program (JJ/WBGSP) for granting the financial support to study in the University of Twente, ITC. My thanks is as well due to the Debub Region Administration and the Ministry of Agriculture of the State of Eritrea for giving permission to pursue my MSc study.

I would like then to give my heartfelt thanks to my first advisor, Dr. X. Chen (Xuelong), for his invaluable support and encouragement from the beginning to the end of my research work. Particularly, I'm thankful for encouraging me to learn and use advanced image processing MATLAB techniques that has been useful in my research. I'm very honoured as well to acknowledge my second supervisor, Dr. ir. Maciek Lubczynski, who has always allowed this paper to be my own work, however, led me in the right direction whenever he thought I needed it. His warm approach and well organized way of following up my pace in time is something I wouldn't pass without mentioning it.

I am glad to extend my sincere appreciation to: Mehreteab Yohannes Weldemichael, a former ITC student for providing helpful information about the Sardon Catchment model and data; Petra Budde from education and research in ITC who assisted me in the *.ftp server and MSG ToolBox installation and usage; Carla Barroso from Surface Analysis Satellite Application Facility (LSA-SAF) help desk who has been answering technical questions about the evapotranspiration data up on my request; Femi Ojambati from the University of Twente for his support in modifying some of my MATLAB scripts; and Richard Winston from the USGS for answering technical questions on the use of Modflow Model Muse software.

I am grateful to the "Department of Water Resources and Environmental Management" course director, Mr Arno van Lieshout, and the staff members in the department for all their esteemed collaboration during my study period in ITC.

Lastly, my profound gratitude goes to my family and friends who have been encouraging me throughout my study period.

TABLE OF CONTENTS

LIST OF FIGURES

LIST OF TABLES

LIST OF ABBREVIATIONS

ADAS	Automatic Data Acquisition System
BF	Bias Factor
CHIRPS	Climate Hazards Group InfraRed Precipitation with Station data
DEM	Digital Elevation Model
DM	Dehesa in Spanish (montado in Portuguese)
DMET	Daily Evapotranspiration Product from LSA-SAF
ET	Evapotranspiration
ETg	Groundwater Evapotranspiration
ET_o	Reference Evapotranspiration
ETsat	Satellite based Evapotranspiration
Exf_{gw}	Groundwater Exfiltration
EXTDP	Extinction depth
F	False bias
GW	Groundwater
H	Hit bias
HR	Hard rock
I	Canopy Interception
IP	Iberian Peninsula
Kc	Crop Coefficient
LSA-SAF	Land Surface Analysis Satellite Application Facility
M	Miss bias
MAE	Mean Absolute Error
ME	Mean Error
MODFLOW	Modular Three-Dimensional Finite-Difference Groundwater Flow Model
MSE	Mean Squared Error
P	Rainfall
PET	Potential Evapotranspiration
PR	Potential Recharge
Psat	Satellite-based Rainfall
q	Stream discharge at the catchment outlet
q_g	Lateral groundwater outflow
Re	Effective Recharge
Rg	Gross Recharge
RMSE	Root Mean Square Error
Rn	Net Recharge
RUF	Recharge Upscaling Function
SC	Sardon Catchment
UZF	Unsaturated-Zone flow package in MODFLOW
WLHRA	Water Limited Hard Rock Areas
RS	Remote sensing

1. INTRODUCTION

1.1. General background

Groundwater (GW) resources in hard rocks (HR), which are associated with fractures and weathering, are vital in all parts of the world. In GW, the accurate estimation of recharge and assessing the fundamental controlling factors are of utmost importance to protect GW systems (Zomlot et al., 2015). This means the knowledge of the recharge processes in HR is helpful for analysis of water resources (Sharp and Troeger, 2014)). Likewise, the American Geological union (AGU) elaborates the importance of recharge assessment in the management of GW.

In HR, movement of GW is dominantly controlled by fractures and fissures (Zhang et al., 2002). For this, the recharge assessment of these rocks is more difficult than in other aquifers because of higher discontinuity, anisotropy, and heterogeneity of the medium. Consequently, this leads to scale dependence of the assessment parameters (Zomlot et al., 2015; Lubczynski & Gurwin, 2005). As the USGS GWRP (2016) puts on its web page, it is almost impossible to measure GW recharge by direct means. In similar terms, determination of recharge rates in HR is neither easy nor straightforward (Bhuiyan et al., 2016; Obakeng et al., 2007). Moreover, Zomlot et al. (2015), referring to Anderson & Woessner (1992), described recharge in HR to be one of the most poorly controlled hydrological parameters in GW flow and transport models. In addition, Healy & Scanlon (2010) and Krásný & Sharp (2007) indicated that recharge rates are the least understood, largely because they vary widely in space and time. Therefore, careful selection of recharge estimation methods is required in GW, particularly in HR.

Groundwater recharge processes can be assessed using different methods like a tracer, hydrological monitoring, and transient GW modelling (Thivya et al., 2016; Lubczynski & Gurwin, 2005). Recharge can be also estimated by calculating GW (hydrological) budget from evapotranspiration (ET) and precipitation (*P*) (Anderson, Woessner & Hunt, 2015). Several authors have used GW budget to assess recharge. Many of these works, however, used empirical formulas or non-integrated spatiotemporal variables (e.g., Mohammadi et al., 2014; Herrmann et al., 2015; Wang et al., 2016; Zomlot et al., 2015; Herrmann et al., 2016). Such approaches that do not account for good spatial and temporal fluxes in GW recharge estimations may lead to higher uncertainties. For example, in an event-based study of recharge made by Guber et al. (2011) in the semi-arid parts of USA, high uncertainty was found on all water budget components. This was due to spatiotemporal variations in *ET* and *P*. This means, the recharge estimation from empirical based or point measurement *P* and *ET* may lead to relatively higher uncertainties.

Recharge estimation is challenging due to limited accuracy and lower relevance of available measurements, particularly when it comes to upscaling the point recharge measurements to regional scales. In line with this, L. Zhang et al. (2002) emphasizes the necessity of careful understanding of its spatial variability of recharge when scaling up to large catchment; as water can move laterally and *P*, vegetation & soil are spatially variable. The simplest method is to extrapolate/upscale ground water recharge from point based inputs to a regional scale by averaging data inputs of the point measurements. However this gives less reliable spatial distribution, and other methods like hydrograph analysis and geostatistical tools are believed to give relatively better results (Healy and Scanlon, 2010). Recharge estimation and up-scaling methods like: (1) use of a linear fraction of *P* (2) zoned *P* values multiplied by assigned weights (3) linear regressions (multiplication of independent watershed characteristic parameters and coefficients) are also indicated by Healy & Scanlon, (2012). Nevertheless, most of these methods make recharge estimate based on point measurements and are prone to uncertainties.

However, the latest advancements in remote sensing to measure *P* and *ET* have enabled not only to estimate recharge but also to upscale/extrapolate the recharge estimates made from point data to a larger area where ground data are not available (Healy and Scanlon, 2010). In this regard, Reyes-Acostaa (2013) has used remote sensing to scale up tree transpiration in the Sardon Catchment. Moreover, remote sensing solution of energy balance is applied in the quantification of *ET* at large scales and scale-up of GW recharge as for example done by Boegh *ET* al. (1999), Nagler *ET* al. (2007), Murray *ET* al. (2009) and Cristóbal *ET* al. (2011).

Very recently, Gemitzi et al. (2017) have used remote sensing and regression equations by correlating recharge from a calibrated Soil and Water Assessment (SWAT) model with effective precipitation from ground data, and actual evapotranspiration (AET) of the model with AET from remote sensing MODerate Resolution Imaging Spectrometer (MODIS). The results indicate that groundwater recharge can be estimated from MODIS evapotranspiration data without numerical modelling, especially where data are scarce. However, the groundwater recharge component which has been regressed (gross, net or effective recharge) is not clearly indicated. As explained by Lubczynski and Gurwin (2005) the net recharge give a good indication of climatic changes. Similarly, Rossman et al., 2014) has used MODIS based precipitation and evapotranspiration estimates to study the effect of vadous zone in groundwater recharge potential of the present century. The MODIS based surface temperature was used to derive *ET* (applying linear transformations) there by calculate potential GW recharge by subtracting the *ET* from *P*. Additionally, Brunner et al. (2004) have scaled up monthly recharge using the correlation between the recharge from chloride method and the potential recharge (*P-ET*) from remote sensing. The study as well indicated the difficulty of using the recharge and *P - ET* correlation in arid and semi-arid regions. Moreover, Wang et al. (2016) used remote sensing in comparing the relationship of groundwater recharge estimation of a surface hydrological model with evapotranspiration from the model and model recharge with evapotranspiration from other techniques. Apart from this, Macdonald and Edmunds (2014) indicates the possibility of using remote sensing rainfall to estimate GW recharge in semi-arid Zimbabwe. However, all these studies have not specifically estimated the net recharge (*Rn*), and the recharge potential estimates are at monthly temporal scales.

This study aims to scale up the numerical GW output net recharge (*Rn*) estimate of Sardon Catchment to other parts of the water limited hard rocks (WLHR) in the Iberian Peninsula (IP), and using satellite-based rainfall (*Psat*) & satellite-based evapotranspiration (*ET*sat) data. The dehesa areas, located in the central and southwest parts of Spain and in eastern Portugal where they are known as montado (Fig. 1) further referred as DM, are woodlands with a large contribution of open grasslands. The recharge potential, the Gross Recharge (*Rg*) or *Rn* of these HR has not been studied, and therefore, this study is vital in the proper management of water resources in the area.

1.2. Research setting

1.2.1. Research problem

The main problem of this research is to evaluate the unknown regional recharge potential of hard rocks of the large DM area (141,430 km^2) based on recharge estimation done in Sardon Catchment (pilot area of 80 km^2). Recharge estimation in HR is difficult due to the heterogeneities & anisotropies of the HR dominating the DM area. In addition, the assessment of recharge is a challenge because of the scarcity of reliable ground rainfall *(P)* and evapotranspiration *(ET)* data. Moreover, the challenges are bigger when trying to upscale recharge from a small catchment into a larger catchment.

1.2.2. Research objectives

Overall Objective

The overall objective of this research is to understand the spatiotemporal dynamics of recharge in the DM areas of the IP.

Specific Objectives

The specific objectives of this research are:

i. To define study area extent, common for water-limited dehesa montado (DM) land cover type and hard rock (HR) areas, further referred as DMHR area.
ii. To derive spatiotemporally variable *P*;
iii. To derive spatiotemporally variable *ET*;
iv. To derive spatiotemporally variable potential recharge PR computed as *P-ET*;
v. To improve Sardon Catchment's model by applying spatiotemporally variable input fluxes from Oct 2011 to Sept 2014;
vi. To define net recharge (*Rn*) upscaling function (RUF) applying *Psat*, *ETsat*, and PR applicable for DMHR area;
vii. Using the RUF, to scale up the *Rn* of SC into DMHR area.
viii. To understand and analyze spatiotemporal dynamics of groundwater recharge over the DMHR area.

1.2.3. Research questions

Main research question

What is spatiotemporal dynamics of groundwater (GW) recharge in the DMHR area of the Iberian Peninsula (IP)?

Specific research questions

The following specific research questions will be answered at different stages during the processes of this study.

1) What is the spatiotemporal distribution of rainfall (*P*) over the DMHR?
2) What is the spatiotemporal distribution of evapotranspiration (*ET*) over the DMHR
3) What is the spatiotemporal distribution of potential recharge (*P-ET*) over the DMHRs?
4) What is the spatiotemporal distribution of net recharge (*Rn*) of Sardon Catchment?
5) What is the best recharge upscaling function (RUF) to scale up SC net recharge into the DMHR area using RS-based fluxes (*Psat*, *ETsat*, & *Psat-ETsat*)?
6) What is the spatiotemporal net recharge in the DMHR area?
7) What is the spatiotemporal groundwater recharge dynamics in the DMHR area?

1.2.4. Research assumptions

- The climatic, land cover, hydrological, and hydrogeological conditions of the DMHR areas are similar to Sardon Catchment conditions where spatiotemporal recharge is known.
- The recharge of urban areas in the DMHR is zero.
- Precipitation is assumed to be the only GW input, through diffused GW recharge;
- Lateral GW inflows/outflows are negligible;
- River GW inflows/outflows are either negligible or balanced among each other;

- The RS-based *Psat* and *ETsat* as well as Sardon model recharge, are valid and accurate.
- The rainfall interception rate is constrained by plant dependent interception fraction (spatiotemporally dependent I_f). In other words, the rainfall interception rate of the tree canopies is independent of rainfall intensities and extreme rainfall amounts.

1.2.5. Novelties of the study

The novelties of this study are:

1) The previous GW studies (recharge estimate in this case) were done in the pilot area (~80 km^2), i.e., in the Sardon Catchment. However, the current research targets to study the GW *Rn* in much larger areas of dehesa (montado) hard rocks in the western Iberian Peninsula (IP), so called DMHR area.
2) This study represents first time combined use of remote sensing, GIS, and MATLAB for processing time series *P* and *ET* images followed by regression analysis to estimate the potential recharge (PR) and scale up net recharge (*Rn*) of the SC into the DMHR area.
3) The scaling up technique proposed in this study (using remote sensing) is original.
4) This study is the first time characterization of the DMHR recharge dynamics.

2. MATERIALS

2.1. Description of the study area

This study aims on the assessment of GW net recharge (*Rn*) of the dehesa-montado hard rock (DMHR) areas of the Iberian Peninsula (IP), which is a typical area with water limited semi-arid environments; (Leonardo & Lubczynski, 2013; Francés et al., 2014; Hassan et al., 2014; Lubczynski & Gurwin, 2005). The IP includes the countries of Andorra, Portugal, Spain, and the British Crown colony of Gibraltar. The geographic location of the DMHR is 42° 43' 12" N to 37° 8' 60" N and 8° 47' 24" W to 2° 32' 60" W. The study that is done in a pilot area of Spain (Sardon Catchment) indicates that the area is characterized by shallow water table, weathered and fractured granite rocks of relatively low storage, dense drainage networks, and high *P* intensity (Hassan et al., 2014). In addition, human impact is insignificant in this area (Reyes-Acosta and Lubczynski, 2013). Most parts of the DMHR have similar environmental characteristics with Sardon Catchment. Therefore, this similarity is important in understanding the natural GW recharge processes and the impact of climatic change on water resources over the DMHRs in the IP. The location map of the study area (DMHR) is shown in Fig. 1. The total area is 141,430 km-2

The study area is defined by combining geological and aridity map of the IP (dehesa/montado). Two layers of geological maps are used to delineate the DMHR area. These were a detailed geological map prepared by USGS that is retrieved from http://portal.onegeology.org/OnegeologyGlobal as well as a simplified map of hard rocks (HR) prepared by EURARE project and the British Geological Survey http://www.eurare.eu/countries/spainAndPortugal.

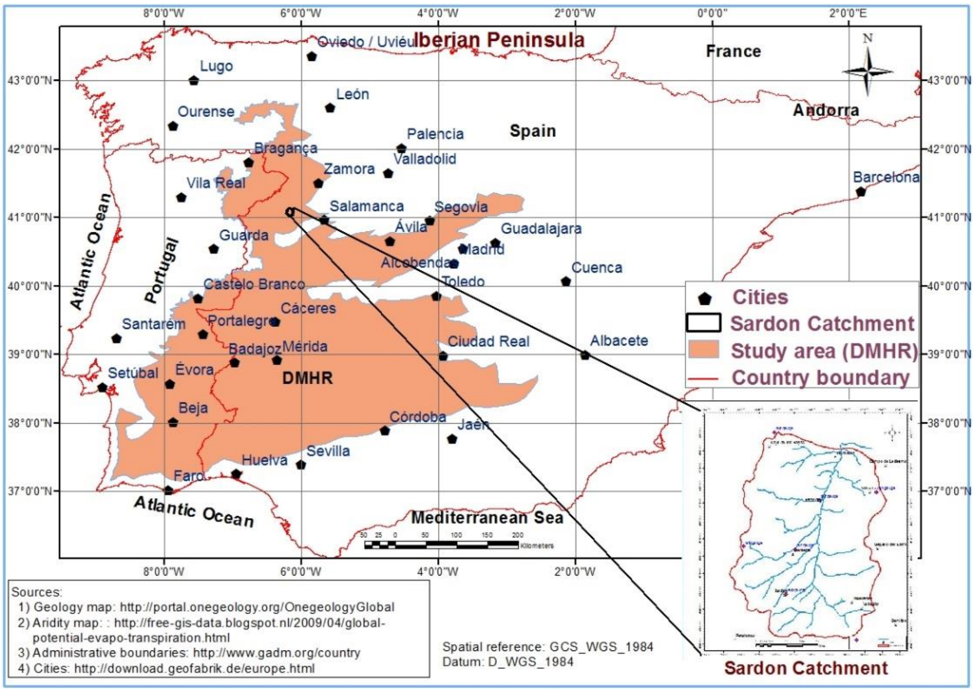

Figure 1: Location map of the water limited dehesa (montado) hard rock (DMHR) area; defined by retrieving geology map from the USGS website, exporting it to google earth as *.kml, digitizing HR areas on Google Earth, exporting the digitized map to ArcGIS as .kml & combining it with aridity map using spatial analysis tools in ArcGIS that is finally classified with a threshold of 0.75 aridity index.

2.1.1. Boundary of the study area

The IP is bordered by the Atlantic Ocean in the north, west, and southwest, while the Mediterranean Sea in the eastern and southern. The Pyrenees Mountain ranges also border the north-eastern peripheries of the IP. The Strait of Gibraltar separates the IP from the African landmass. Within the IP, the boundaries of the study area are defined by the occurrence of HR and aridity index. Therefore, the boundaries of the study area include the HR areas (in the IP) which are water limited (aridity index < 0.75).

2.1.2. Climate

The IP, in which the DM covers its large part, is found in the climatic transition zone of the mid-latitudes and the subtropical climates (García-Barrón et al., 2015). According to Moreno et al. (2012), in which they cited Sumner et al., (2001), the IP has generally a dry and hot summer because of the influence of the subtropical high atmospheric pressure belt, and winter rains due to mid-latitude storms entering the region of the Atlantic Ocean. Depending on the influence of topographic and geographic locations the IP is divided into three climatic regions as: (i) the inland moderate continental climate; (ii) the Mediterranean climate; and (iii) the Atlantic Ocean climate in the north and northwest parts (Sumner et al., 2001). Therefore, the DM can be generally considered as arid and semiarid Mediterranean climate. The temperature varies from 0°C to 37°C.

The climatic conditions in an area can be estimated by an aridity index. Aridity index, expressed as the annual potential evapotranspiration (*PET*) divided by annual *P* (Arora, 2002; Salvati et al., 2013), gives a good estimate of the climatic water stress. The fact that the aridity index takes into account both physical phenomena (*P* & *PET*) and biological processes (plant transpiration), it is a good estimator of bioclimatic changes (Salvati et al., 2013). This index is used to define the study area by combining it with HR areas from a geologic map. The global aridity map downloaded from http://free-gis-data.blogspot.nl is produced with the support of International Water Management Institute (IWMI). Fig. 2 shows aridity index map of the DM in the IP.

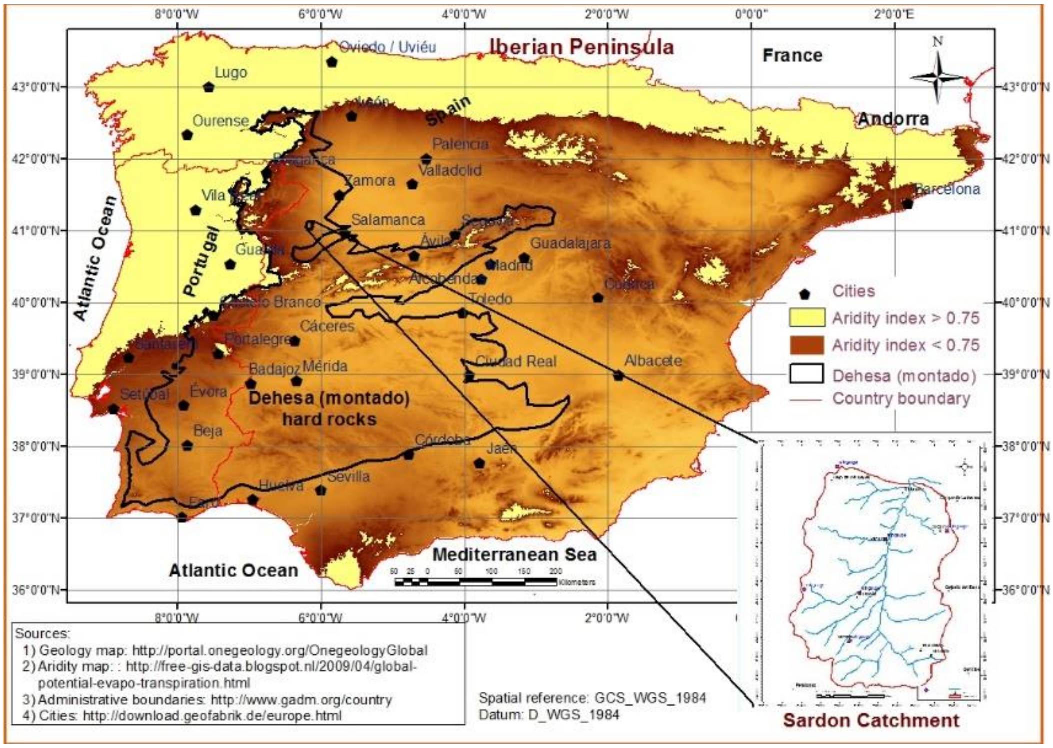

Figure 2: DM aridity map classified in Arc GIS as water limited and non-water limited areas applying a threshold of 0.75; areas in brownish colour represent water limited & areas in yellow represent non-water limited.

Precipitation in the IP is low with high evaporative demand, in which the low summer *P* usually coincides with the high *PET* (Campos et al., 2013). Most of the areas in the region show high variability of *P*. They experience wet years mixed with recurrent droughts, high concentrations of *P* over a few days with low *P* during the summer; which is the characteristics of the Mediterranean climate. Referring to Lionello et al. (2006); and Martín-Vide & Olcina. (2001), García-Barrón et al. (2015) described the *P* in the IP to be mixed wet years with recurrent droughts, high *P* concentrating over a few days, and low *P* during the summer. This is typical of the Mediterranean climate. The annual *P* in the study area is ~500mm (based on the 23 years average estimate of a station in Sardon Catchment). However, the amount and distribution vary along the coasts, north, and south parts of the IP. The study area has two distinct seasons; the wet season that includes months Oct to May and the dry season comprising June to Sept (Hassan et al., 2014). The rest of the months receive fewer *P* showers than the main wet months.

2.1.3. Vegetation

The vegetation of the IP is mostly dominated by oak woodlands, commonly termed as dehesa in Spain and montado in Portugal. Referring to the Mid-Atlantic Regional Meeting (MARM 2008), Campos et al. (2013) have defined the DM as an oak woodland mixed with grassland and shrubs. The DM region is dominated by two main oak tree species. These are the deciduous *Pyrenean oak* (*Q. pyrenaica*) found at low elevations of higher latitudes and the small leaved semi-deciduous holm oak (*Q. ilex*) species that dominate most parts of the IP (Campos et al., 2013). The *Q. ilex* are mostly associated with siliceous and calcareous soils, where *P* can go as low as 300mm or 100mm. The *Q. pyrenaica* are common to areas of siliceous soils, where *P* is relatively higher.

From the field observation, it is noted that the main tree species in Sardon Catchment are the evergreen oak (*Quercus ilex*) found mostly in the northeast parts of the Catchment, and the deciduous broad-leaved oak (*Quercus pyrenaica*) common along the stream channels. The *Quercus pyrenaica* are also abundant in the south and southwest parts of Sardon Catchment. Fig. 3 shows the main tree species in the DMHR.

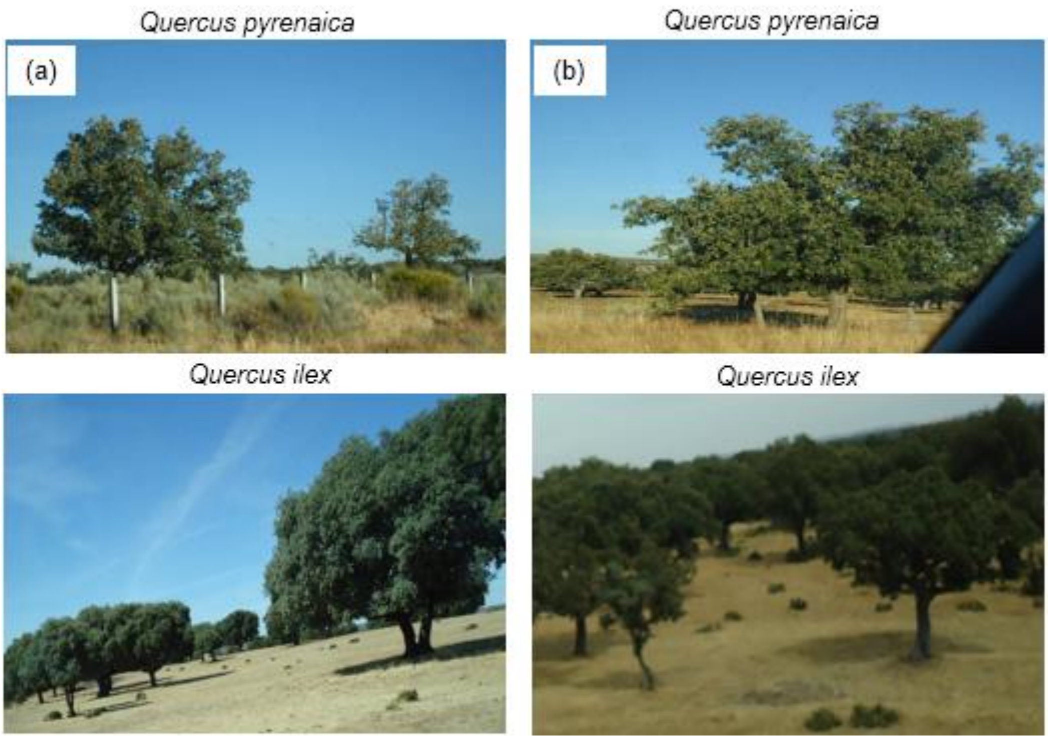

Figure 3: Vegetation in dehesa of southern Spain: a) *Quercus pyrenaica* (top) & *Quercus ilex* (bottom) in SC and b) *Quercus pyrenaica* (top) & Quercus ilex (bottom) between Sardon Catchment (SC) and Ledesma.

In general, the Quercus ilex species are relatively more abundant in the Ledesma areas (a town in the southern part of DMHR) than the other areas that are visited. As you move from Sardon Catchment (south of Ledesma town) towards Salamanca city, towards the north of the DMHR, the Quercus pyrenaica species are more common.

2.1.4. Topography

Based on slope analysis of a Digital Elevation Model (DEM) 30 meter resolution, the altitude of the IP ranges from 0 to 3466m. The low altitudes predominate the western parts and areas along the coasts. The northeast parts including some areas in the central southeast of the DMHR areas have high altitudes. To the north, the DMHR is surrounded by the Pyrenean and Cantabrian mountains. The slope ranges from flatlands of ~0° (green colour in map) up to steep slopes (red in the map) > 75° (Fig. 4). The steep slopes are high elevation areas as well. The DMHR areas are steeper than the rest central parts of the IP.

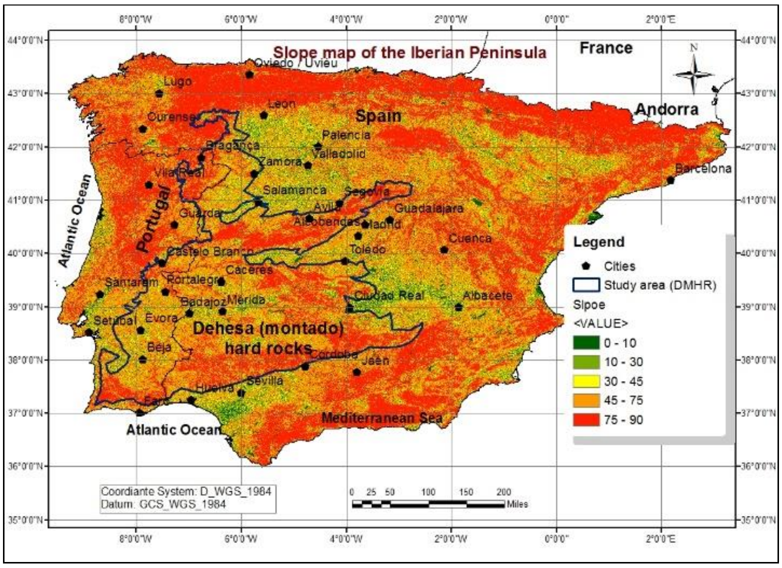

Figure 4: Slope map of the Iberian Peninsula (IP) derived from DEM 30m downloaded from the USGS website available as tiles of 1° longitude by 1° latitude, merged in Arc Map 10.4.1 and clipped by the IP (Spain and Portugal) boundary maps. The slope is then computed in the spatial analyst surface tool.

2.1.5. Drainage

The IP has five major drainage basins (river systems): the Ebro, Tajo, Guadalquivir, Guadiana and Duero (Santisteban and Schulte, 2007), of which the latter four are in the study area. All these rivers (except the Ebro) finally carry their water to the Atlantic Ocean and the Ebro to Mediterranean Sea (Fig. 5). These rivers show seasonal variations of flow. Hassan et al. (2014) describe the drainage in Sardon Catchment, which is representative to the other parts of the DMHR areas, to be characterized by rapid overland flow and interflow due to high *P* intensity and saturation excess runoff related to perennial GW discharge areas.

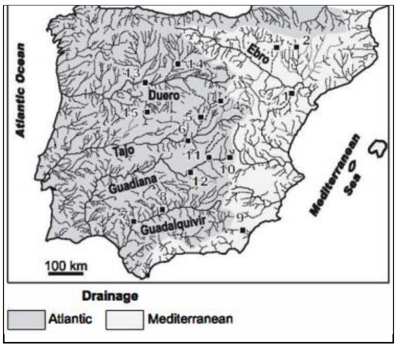

Figure 5: The Iberian Peninsula (IP) major drainage networks (taken from Santisteban & Schulte, 2007).

The drainage network is dense mostly with intermittent flows. Many outcrops of water flow over the fractured granites along the small stream channels, and sometimes surprisingly along the slopes outside the channels. The source for the later water outcrops water could be the mountains in the north and northeast of the catchment with fractured hard rocks (HR) that replenish the low elevation areas. The water table, as measured from the loggers that have been installed in the boreholes and piezometers in SC, ranges from less than 1 m to ~4 m depth in the driest season. The amplitude (the rise & fall of the water table depth) is ~2 m. Apart from the intermittent flows, streams with a large volume of water flowing throughout the year like Rio Torness River are also found in the DMHR area. This river that initiates in Avila province (a province bordering Salamanca province in the west) and crosses the Salamanca region near Salamanca city is the main water carrier to the Almendera dam located near the border of Portugal. Most of the streams in the study area flow from north and northeast to the south and southwest of Spain and then to Portugal.

2.1.6. Hydrogeology

Previous studies in the IP (e.g. Izquierdo, 2014; Mahmoudzadeh et al., 2012) show that DMHR areas of the IP are characterized by fractures, fissures, and faults with the shallow water table. A study by Custodio et al., (2016) in a pilot area of the IP show that GW storage depletion is high, exceeding recharge by *P*. The hydrogeological framework of Sardon Catchment by Lubczynski & Gurwin (2005) and also that was explained by Hassan et al. (2014)) has identified two permeable layers (top unconsolidated and lower fractured granite layer). Similarly, Francés et al. (2014) have classified the hydrogeology of SC into two main hydrostratigraphic layers: a saprolite top layer of weathered & alluvial deposits and a fissured layer which are intersected and drained by fault zones that control the hydrogeology of the catchment. Lubczynski & Gurwin (2005) have described the average depth of water table in the fractured HR of SC to be 0 – 5 m, and exceptionally up to 10 m. The hydrostratigraphy in the DM that have similar surface geology is expected to be similar to SC. The movement of water in these aquifer systems is mainly controlled by the faults, fractures, and fissures (see Fig. 7) in the granitic rocks (secondary porosity). The fractures (depending on their geometry, density, and chronology) and fissures in these DMHRs may operate as effective drainage lines along dense stream networks.

The hard rock (HR) areas are defined in this study by combining two geologic maps: (1) detailed geology map showing geologic units from http://portal.onegeology.org/OnegeologyGlobal/ (Fig 6b), and (2) simplified geologic map of HR (Fig. 6a) from http://www.eurare.eu/countries/. Many studies like Picos & Formation, (2011); Posada, (2016) and Vázquez-Vílchez et al. (2015) have used this simplified HR map. Plum color in Fig. 6a brown and gray colors in Fig. 6b represent HR areas. The Iberian Massif (see plum colour areas in Fig. 6a) that are the major hard rocks areas in the IP are resulted by the collision between the Gondwana and Laurasia in the late Paleozoic era, followed by polyphaser deformation, magnetism, and extensional orogenic collapse exhumed high-grade granitoids (Fernández and Pereira, 2016).

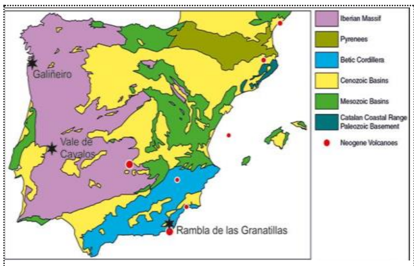

(a) Simplified geologic map

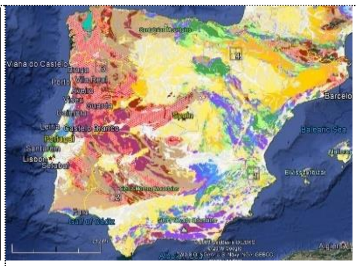

(b) Geological units of IP

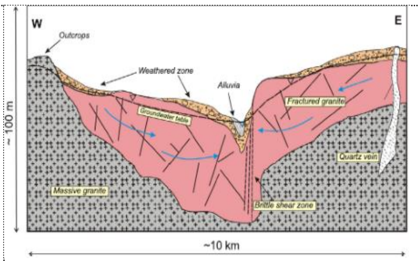

Schematic geologic cross-section

Figure 6: Geologic Maps of the Iberian peninsula (IP): a) Simplified map of hard rocks (HR); plum colour are HR areas, the Iberian massif b) Geologic map of geological units by USGS geological survey; dark brownish and pinkish colours are HR areas.

Figure 7: Schematic geologic cross-section of the Sardon Catchment (after Lubczynski & Gurwin, 2005).

The geological formations in SC are dominated by fractured granites, where there are outcrops in many parts (Fig. 8a, b & c). These rocks are usually found to be weathered on the top part and fractured bottom underlain by massive granitic bedrocks. The top weathered parts of these outcropped granitic rocks usually appear as green decays. Quartzite rocks are also found in the eastern parts of the SC. In addition, hard schists are observed in some parts. The soil type in these areas, in general, have a shallow depth and are relatively less fertile. Similar geologic formations extend between SC (Ledesma area in general) up to a few miles when you drive to the Salamanca city. As you move further from the city of Salamanca to the north the rock types are dominated by sandstones. The soil types around Salamanca are relatively deep and more fertile as compared to Ledesma areas. Black soils are also found in small localities of these areas.

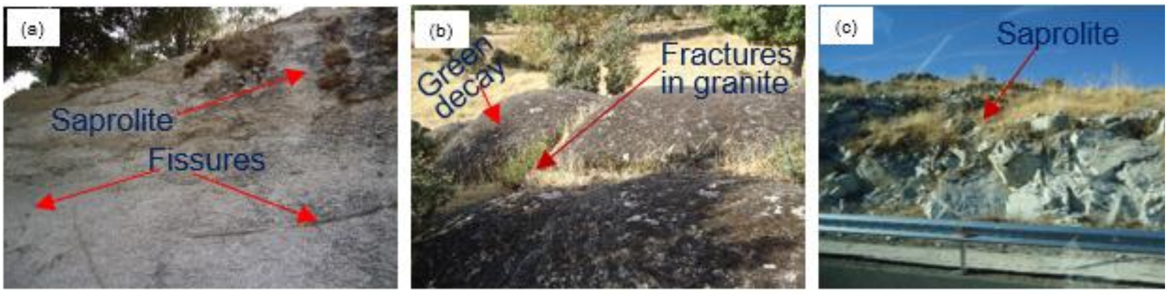

Figure 8: Typical rock types in dehesa (montado) hard rock (DMHR) area; a) Fractured granite overlain by saprolite weathered top in Sardon Catchment (SC), b) Hard granite rock with top dark green decay (SC), and c) Fractured granite overlain by saprolite weathered top (Near Salamanca). The fractures and fissures shown in the figures play a dominant role in controlling the recharge potential movement groundwater in these areas.

2.1.7. Artificial waterbodies

Many farm ponds of mostly less than ~5000 m^3 storage capacity are found in Sardon Catchment and other parts of the DM. These ponds still stored water during the fieldwork that was done in the driest season (Sept). This is because of the shallow water table outcrops (Fig. 9 to Fig. 11) to the surface. Apart from this, big dams are constructed near the borders of Portugal. One of these dams, called Almendra dam was visited during this field work. It stores 2.5 billion m^3 of water. It is found towards the end of the present study area (DMHR), and therefore its effect on recharge of the current research is not significant.

Figure 9: Outcrops of GW in Sardon Stream in the dry season. These serve as drinking water for livestock even in the dry seasons.

Figure 10: Small ponds harvesting the shallow water table outcropping through rock fractures along the slopes in Sardon Catchment (SC). The rocks are grooved by the inhabitants to provide water for their livestock in the dry season.

Figure 11: Farm ponds built in SC that harvest the flowing outcrops of water during the dry season for livestock.

2.1.8. Urbanization

In the study area, cities like Salamanca, Avila, Badajoz, Évora, and Castelo Branco are found (shown in Fig. 1). Cities and towns including some villages are covered with concretes, pavements, and tarmac. These do not allow rainwater to infiltrate into the ground. So, recharge in such settlements is expected to be zero. Therefore, for better recharge estimate, these cities need to be excluded (or assumed to be no recharge) from the final recharge map. However, this is not done in this study.

2.2. Data sets

2.2.1. Ground data

The ground data inputs like *P*, potentiometric heads, inputs for PET, infiltration, and other necessary data used in the transient model of SC by Weldemichael (2016) are adopted in the present model simulation by adjusting with spatiotemporally variable inputs (from year 2011 to 2013).

2.2.2. Remote sensing data

Rainfall

There are different satellite rainfall *(P)* products at varying spatial and temporal resolutions on different websites. Some of these products are available globally and some for a certain region. Climate Hazards Group InfraRed Precipitation with Station data (CHIRPS) rainfall product spinning in 50°S-50°N is selected. The CHIRPS rainfall product (*Psat*) is downloaded from http://chg.geog.ucsb.edu/data/ website. This product is available in hourly, daily, pentad, monthly, yearly, and decadal temporal resolutions, and 0.25° & 0.05° spatial resolutions. The daily (unit in mm) product of 0.05° is selected for this study with 0.05° (~5 km) spatial resolutions because it is the highest resolution of this product available for the IP. The daily temporal resolution is chosen because the Model Muse uses daily *P* and *ET* inputs, and gives daily fluxes like the *Rg* and *Rn*. Based on this the *Rg* and *Rn* can be scaled up from SC to the DM on a daily basis to give better (detailed) information on the GW recharge dynamics. Therefore, a daily global *Psat* product from Jan 2007 to Aug 2016 is downloaded. Fig. 12 shows the pixels of CHIRPS representing SC. The study area, the DMHR, is covered by 5842 pixels of CHIRPS.

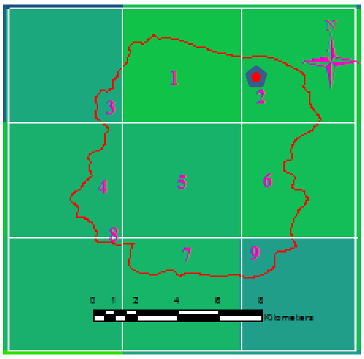

Figure 12: CHIRPS daily rainfall (*Psat*), 9 pixels covering SC. The dot in pixel 2 is where Trabadillo station is located

Daily evapotranspiration (ET)

Daily satellite-based evapotranspiration (*ETsat*) product (Jan 2011 to Aug 2016) is downloaded from Land Surface Analysis Satellite Application Facility (LSA-SAF): https://landsaf.ipma.pt/security/login.jsp. Daily evapotranspiration product from LSA-SAF (DMET) is available from the end of Dec 2010 onwards. This DMET is based on MeteOp/AVHRR or MSG/SEVIRI. It is available in 30 minutes & daily temporal resolutions with units of mmh^{-1} and mmd^{-1} respectively. The spatial resolution for Europe is ~3.1 km. The DMET product is produced from radiative data derived from Meteosat Second Generation (MSG) geostationary satellites and recent land-cover information from ECOCLIMAP database with ancillary meteorological data from ECMWF forecasts. The DMHR area is covered by 19,512 DMET pixels.

DEM

A digital elevation model (DEM) of 30 m resolution (SRTM30) is retrieved for the study area from http://earthexplorer.usgs.gov. This DEM has a spatial reference of GCS_WGS_1984 and datum of D_WGS_1984. It is available in tiles. One tile covers 1º longitude by 1º latitude. Then, ArcGIS is used to merge all the tiles and subset to the study area.

3. RESEARCH METHOD

Many studies have been done to estimate groundwater (GW) recharge in a small part of the IP, called Sardon Catchment (e.g., Francés et al., 2014; Hassan et al., 2014; Mahmoudzadeh et al., 2012). In these studies, remote sensing techniques were not applied. Lubczynski & Gurwin (2005), however, integrated spatiotemporal data from remote sensing, sap flow, chloride mass balance, automated climate monitoring, depth of water table, and river discharges to estimate water budget in the Sardon Catchment (SC). All the previous studies (in the IP) focused on a small catchment. Therefore, this study uses remote sensing *P* and *ET* to scale up the recharge from the calibrated model in the pilot area (Sardon Catchment) to the large DMHR area in the IP by defining an upscaling function (RUF).

The transient model of SC, calibrated with spatially uniform (but temporally variable) input fluxes by Weldemichael (2016) applying the staratiform concept of Francés et al. (2014), is now updated by applying spatiotemporally variable inputs from the year 2011 to 2013. Additionally, the simulation tested applying spatiotemporally variable inputs by Weldemichael (2016) for the year 2014 is adopted in this study. These inputs are the crop factor, extinction depth, and interception.

Finally, the present study intends to use the correlation/regression between net recharge (*Rn*) from the model (from Oct 2011 to Sept 2014) and the corresponding satellite-based spatiotemporal fluxes: *Psat*, *ETsat*, and PR (*Psat* - *ETsat*)to scale up the *Rn* of SC over the DMHR areas in the IP.

Flowchart of the summary of procedures

The procedures followed in this study to answer the research questions and meet the research objectives are summarized in the flow chart in Fig 13.

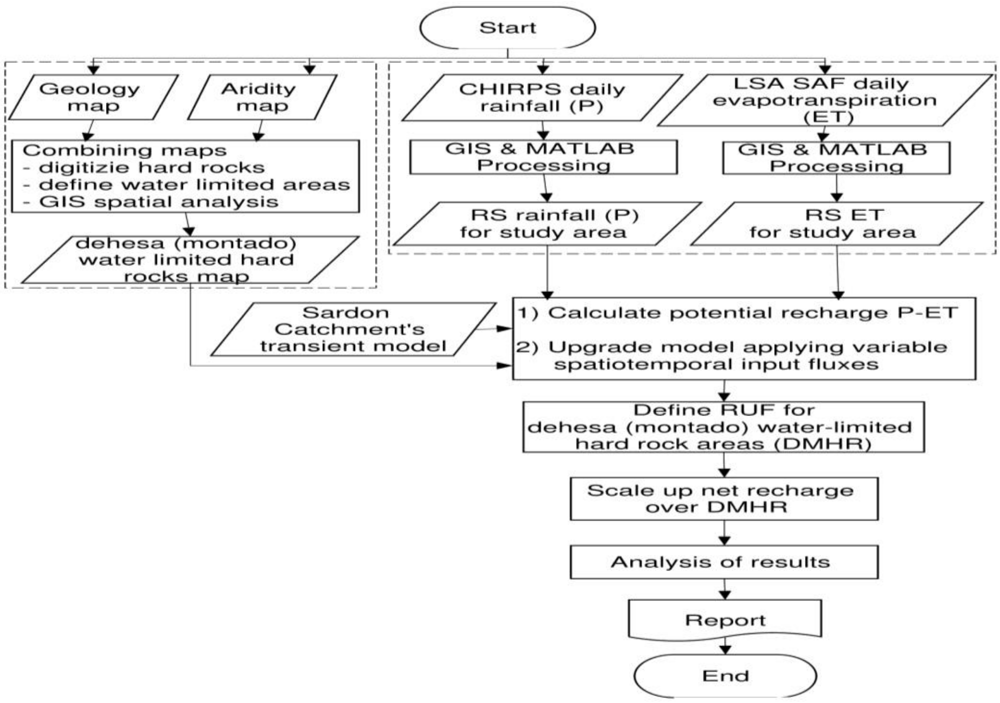

Figure 13: Summary of procedures for scaling up the recharge.

3.1. Field work

Meteorological and hydrogeological data for recent years (2014 up to Sept 2016) are collected from the field work. The meteorological data are collected from Trabadillo ADAS station; a station within Sardon Catchment from which input data were used in the transient model by Weldemichael (2016). The data collected include *P*, temperature, relative humidity, wind speed, radiations. In addition relative humidity, solar radiation and *P* data are downloaded from Muelledes ADAS station. GW level data are also retrieved in the field work from loggers, which have been installed in 7 wells (5 boreholes and 2 explosive wells), and 4 piezometers (one of which is at the outlet of SC). These data can be used in further model updating in other studies (not used in this study). Visual observations are as well made on the topography, vegetation, geology, and other features relevant to GW recharge. Therefore, field work has assisted as a transect walk to observe and understand the physical and environmental conditions of the study area particularly the groundwater dynamics of the DMHR.

3.2. General approach for scaling up

The recharge potential over an area is governed by different biophysical and climatic factors. The biophysical factors include the surface and subsurface conditions of the area like hydrological, hydrogeological conditions, soil, geology, vegetation cover and human factors (for example settlements). If these biophysical factors of one area are similar to another area, then the climatic factors (*P* and *ET*) govern the recharge potential. Therefore, considering the fact that the surface and subsurface conditions of Sardon Catchment and the other parts of the DMHR in the IP are the same, the recharge is related to environmental/climatic attributes of *P* and *ET*.

The geological and aridity maps are combined to delineate the DMHR area inf the IP. Therefore, the spatially combined HR and aridity map (area) is expected to have similar environmental, surface and sub-surface (hydrogeological) characteristics to the Sardon Catchment. Following this, the daily net recharge (*Rn*) from the model simulation of SC by applying spatiotemporally variable inputs in this study (Oct 2011 to Sept 2013) and the similar simulation done by Weldemichael (2016) from Oct 2013 to Sept 2014 is correlated/regressed with satellite-based fluxes (*Psat*, *ETsat*, and *Psat* - *ETsat*) to derive RUF for DMHR areas. The representative *Psat* and *ETsat* estimates for SC (Trabadillo ADAS station) are derived by interpolation in MATLAB, assigning the geographic coordinate of the ADAS station.

3.3. Defining study area

The geologic map from the website (http://portal.onegeology.org/OnegeologyGlobal) is exported to google earth, and then the hard rock (HR) areas are digitized. Moreover, a simplified HR map hosted by British Geological Survey, for which the European Commission project namely the European Rare Earth Element (EURARE) is also responsible, is used as a supplementary source to define HR areas in the IP. Then the digitized map is exported as *.kml for processing in GIS (shown in Fig. 18 in section 4.1).

Following the above, the aridity map from http://free-gis-data.blogspot.nl is classified into two based on a threshold. This means areas with aridity index < 0.75 are defined as water limited areas, while areas with aridity index >0.75 are considered not to be water limited (Arora, 2002). The Aridity Index (AI), is the ratio between mean annual *P* and mean annual *ET* (Lobera et al., 2015). Therefore, water limited dehesa (montado) areas in the IP are classified using conditional statements in GIS (see Fig. 19 section 4.1). Finally, the water-limited hard rock areas (WLHRA) in the IP, the DMHR area, are defined by spatial GIS combination of the HR (Fig. 20 in section 4.1) and water limited area maps to define the final DMHR area.

3.4. Rainfall estimation and validation

The *P* input in the transient model of SC by Weldemichael (2016) was *in-situ* data from Trabadillo ADAS station. Fairly enough, Lubczynski & Gurwin (2005) have approved the *P* in the SC to be represented by this station. Nevertheless, single in-situ *P* measurement, has limited spatial distribution (Habib et al., 2014), particularly when point *P* measurement is interpolated to a wide area, like from the Trabadillo ADAS into the DMHR. However, recent developments of remote sensing rainfall measurements have allowed getting relatively good spatial and temporal resolution of rainfall. For this reason, CHIRPS rainfall product (*Psat*) is used in this study.

The daily global CHIRPS rainfall data (*Psat*) from the year 2007 to end of August 2016 is downloaded from the website (http://chg.geog.ucsb.edu/data/chirps/) with free registration. The processing (importing the maps, sub-mapping to the study area, retrieving pixel values) were done by using GIS scripts, map lists, and batch processing tools in ArcGIS. Further processing and preparation of final spatiotemporal *Psat* maps are done in MATLAB.

3.4.1. CHIRPS rainfall overview

Despite the advantage, satellite-based rainfall products are affected by measurement uncertainties. Two types of errors, the random and systematic, affect the *P* estimate from a satellite. Therefore, bias correction by applying *in-situ* measurements (like rain gauge) can be helpful. However, bias correction may not all the time improve the accuracy of the estimate. For example, in a study by Alemseged, T.H and Rientjes (2015), some stations did not show improvement of rainfall measurement after doing bias correction.

The advantage of CHIRPS rainfall product (*Psat*) is that it uses gridded satellite-based *P* estimates from NASA and NOAA and combines the satellite *P* estimates with gauged station *P* measurements. So, this can reduce the systematic error in the *Psat*. Nonetheless, in this study, bias analysis and correction test is done in order to check the accuracies of the CHIRPS estimate

One way of judging the consistency of satellite *P* estimates against *in-situ* measurements is by using a double mass curve. This means cumulative of the *in-situ P* measurement, Trabadillo ADAS station in SC, is plotted on the abscissa and the satellite measurement on the ordinate. A straight or nearly straight line of these plots shows the consistency of measurement, while zigzags show inconsistency. (e.g., Kusangaya et al., 2016; Bhatti et al., 2016). Based on this in-situ *P* measurement of the ADAS in SC is plotted against the *Psat* measurement of the bias uncorrected pixel (2007 to 2016). The double mass curve has shown some inconsistencies in some parts that are circled in red (see Fig. 14). However, this is still acceptable particularly if the bias correction test doesn't promise a better result.

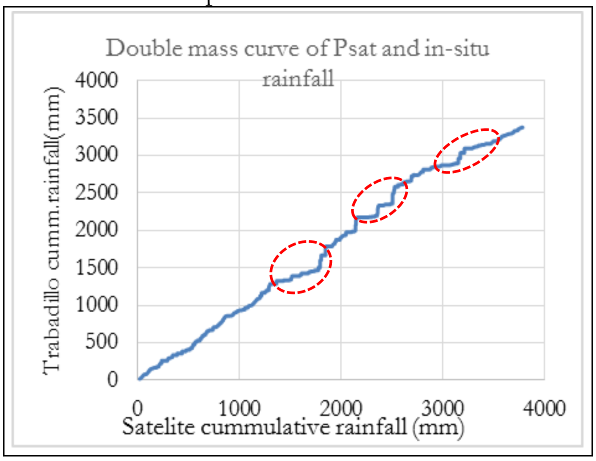

Figure 14: Double mass curve of CHIRPS rainfall (*Psat*) and in-situ measurement.

Secondly, the satellite rainfall errors are analyzed by decomposing into False (F), Hit (H), and Miss (M) biases (Tian et al., 2009; Gebregiorgis et al., 2012; Yong et al., 2016; Haile et al., 2013). According to these authors, F, H and M biases are when the satellite has recorded *P* and the *in-situ* measurement shows no *P*; the satellite and *in-situ* measurements show records of *P* but show variation, and the satellite records no *P* while the *in-situ* measurement shows record respectively. According to Haile et al. (2013) and Tian et al. (2009), these biases are defined as shown in Equations 1 to 4.

$$Meanbias = \frac{1}{n}\sum (Ps - Pg)/(Ps > 0 \,\&\, Pg > 0) \quad (1)$$

$$Hit\,bias = \sum (Ps - Pg)/(Ps > 0 \,\&\, Pg > 0) \quad (2)$$

$$Miss\,rainbias = \sum Pg/(Ps = 0 \,\&\, Pg > 0) \quad (3)$$

$$False\,rainbias = \sum Ps/(Ps > 0 \,\&\, Pg = 0) \quad (4)$$

where n is the number of days for which bias is calculated, *P*s is satellite *P* record, *Pg* is *in-situ* (Trabadillo ADAS station) *P* record.

The bias, in general, is calculated expressed by (Abera et al., 2016) is shown in equation 5. Therefore, the F, H, and M biases are calculated using equation 5, by applying the conditions in equations 1 to 4.

$$BIAS = \frac{\sum_{i=1}^{N}(Ps - Pg)}{\sum_{i=1}^{N} Pg} \quad (5)$$

Logical (if) statements in excel are used to identify (decompose) the F, M, and H biases by first finding the rainy and non-rainy days in the ground and satellite records. In addition, the logical statements in excel are used to compute the bias factors (BF) and do the correction test.

3.4.2. Rainfall validation test

Rainfall bias decomposition is done by taking the time series (Oct 2011 to Sept 2014) of CHIRPS based rainfall estimate (*Psat*) representing Trabadillo ADAS station in SC and the ground reference of the daily tickle bucket rain gauge records of the same station. Then, this can give an indication whether applying bias correction can improve the CHIRPS rainfall estimate for the study area. If the bias decomposition shows more of F or M than H, the correction is less likely to give improvement of *Psat* estimate.

The bias factor for a *Psat* is calculated as a ratio of ground measurement and satellite estimate (Bhatti et al., 2016). It is calculated as shown in Equation 5.

$$BF_i^d = \frac{\sum_{t=d1}^{t=d2} P_{\mathrm{ground}}(i,t)}{\sum_{t=d1}^{t=d2} P_{\mathrm{sat}}(i,t)} \quad (6)$$

Where P_{ground} and *Psat* are daily *in-situ* and satellite rainfall measurements respectively; for a certain pixel location *i* and *d1* & *d2* of time *t*. To do the bias correction test, the *Psat* record for the ADAS station is multiplied by the bias factor (*BF*), calculated in Equation 5.

There is only one rainfall (*P)* station record available for the study area. For this, the bias correction test is applied to the temporally variable *Psat* representing Trabadillo ADAS station in Sardon Catchment. This method is proposed for areas with one *P* station by Habib et al. (2014). Therefore, the daily *P* record (year 2011 to 2014) of Trabadillo ADAS station in SC is used to calculate the bias of the daily *Psat* pixel corresponding to the station.

The bias correction test is done based on different window sizes (number of days for which the bias factor for a given day is calculated). Additionally, the window type can be a sequential or a moving window

(Bhatti et al., 2016; Habib et al., 2014). A moving window means the bias factor for a given day *d* is calculated as a ratio of the sum of the *in-situ P* measurement to satellite measurement, considering *d+1, d+2, … d+ (w-1)* days, where w is the size of the window. A sequential window means the same *BF* is used for the days in the specific window. For example, if the window size is 7, the bias factor for *d1* to *d7* is the same, which is calculated as the ratio of the sum of *in-situ* measurement for the 7 days divided by the sum of the satellite measurement. For a given window type and size also three schemes can be applied; forward window (FW), central window (CW), and backward window (BW) depending on the direction of the movement of the window, either forward, backward, or back and forth.

In this study, a moving forward window of size 1, 3, 5, …and, 31 and a sequential forward window of size 7, 1, 15, 21, and 31 are tested to select the correction method that gives the best *Psat* estimate. The judgment is done based on the analytical errors mean error (ME), mean absolute error (MAE), mean squared error (MSE), and root mean squared error (RMSE) that are calculated as the bias *in-situ P* measurements against the *Psat* tested for bias correction for each of these correction methods. A similar calculation is done for the uncorrected *Psat* estimate as well. At the end, particularly, the RMSE of the bias uncorrected *Psat* is compared with the *Psat* estimates of all window types and sizes. Equations 7 to 10 show how the errors are calculated.

Equations 6 to 9 show how these statistical (analytical) measures are calculated.

$$ME = \frac{1}{n}\sum_{n=1}^{n}(P_{\text{sat}} - P_{\text{gound}}) \quad \text{………} \quad (7)$$

$$MAE = \frac{1}{n}\sum_{n=1}^{n}|(P_{\text{sat}} - P_{\text{gound}})| \quad \text{………} \quad (8)$$

$$MSE = \frac{1}{n}\sum_{n=1}^{n}(P_{\text{sat}} - P_{\text{gound}})^2) \quad \text{………} \quad (9)$$

$$RMSE = \left[\frac{1}{n}\sum_{n=1}^{n}(P_{\text{sat}} - P_{\text{gound}})^2\right]^{0.5} \quad \text{………} \quad (10)$$

where P_{ground} is in-situ (rain gauge) rainfall measurement of Trabadillo station, P_{sat} is satellite rainfall measurement, and n is the number of days from October 1, 2011, to September 30, 2014.

The representative *Psat* is required, so that a recharge upscaling function (RUF) is derived from the relationship of properly estimated *Psat* inputs. In this regard, the representative *Psat* corresponding to Trabadillo station is determined by MATLAB interpolation of the daily *Psat* with respect to the coordinates of Trabadillo ADAS station. This option is chosen if the bias correction test doesn't give satisfactory improvement. Three interpolation methods (linear, spline and cubic) are tested, and the resulting interpolated *Psat* estimates are judged for their accuracy by computing the RMSE against the *in-situ P* record of Trabadillo ADAS.

In addition, spatiotemporal maps (daily) of the whole study area (dehesa/montado) are prepared and further processed in MATLAB. However, the daily maps are later aggregated into monthly for ease of presenting the results in this report.

3.5. Evapotranspiration (*ET*) estimation and adjustments

Like the *P*, evapotranspiration (*ET*) input from Trabadillo ADAS station was used in the transient model of Sardon Catchment by Weldemichael (2016). Studies made on how recharge was affected when *ETsat* is used instead of *in-situ* based recharge measurement (e.g., Soheili, 2014) proved high uncertainties in the *in-situ* based measurements. Therefore, in this study, an endeavor is made to estimate *ET* from remote sensing in estimating GW net recharge (*Rn*). A number of sensor-based energy balance data like MODIS and Landsat are available on different websites. The computation of *ET* from these energy balance components uses the formula *Rn* = Go + H + LE; where *Rn* is the net radiation, Go is the ground heat flux, H is the turbulent sensible heat flux, & LE is the turbulent latent heat flux. Models are also available to calculate *ET* from the energy balance components. These models include like TSEB & SEBAL (e.g., Timmermans et al., 2007), and SEBS (e.g., Su et al., 2014; Chen et al., 2014). For areas with rugged terrains, a topographically enhanced energy balance (TESEBS) method has been recommended to calculate *ET* (Chen et al., 2013). However, the procedures in these methods of computing *ET* are time taking.

Nowadays ready-made downloadable satellite *ET* products are available. These products have different areal coverages, spatial and temporal resolutions. For this study, 5 km spatial resolution and daily temporal resolution is required in order to match the chosen rainfall product (*Psat*). Among the satellite *ET* products available for the IP include, FEWSNET, MOD16, and LSA-SAF. However, the FEWSNET product that is available for the study area has a low spatial resolution (1°). On the other hand, the MODI16 has good spatial resolution, though, it is provided in 8daily basis. So, LSA-SAF daily evapotranspiration (DMET) product, which is available on daily basis, and has ~3.1 km spatial resolution is selected for this study.

The LSA-SAF data is downloaded with a free registration from (https://landsaf.ipma.pt/security). Then the data can be retrieved to either a private *.ftp server or LSA-SAF ftp server. Using the personal ftp server helps for fast downloading of the images. The data are available in zipped *.rar formats, inside which the daily evaporation images are provided in HDF5 formats. In order to open these files JavaScript is installed and checked for its proper function, and then MSGTool Box is that interactively works with JavaScript is used to import the *ETsat* files. By doing this the DMET is imported as GIS or ILWIS formats. The dataset has a scaling factor of 1000. So, all the daily satellite images are divided by 1000 to get the actual daily *ETsat*. After preparing the datasets so that they can be opened by GIS and other softwares they are processed in a similar way as the *Psat* product by using GIS scripts and map lists. Then, further processing and final spatiotemporal *ETsat* maps preparation is done in MATLAB.

The daily LSA-SAF DMET data downloaded for the period of this study (2011 to 2016) had 20 missing days (see Table 1). So the gap filling for these missing days is done using linear correlations (linear averaging) of the satellite DMET (LSA-SAF) images of the preceding and proceeding days. However, the missing data in September are consecutive, so the gap filling is done by taking an average of images for the corresponding days in the other years (2011, 2013, 2014, and 2015).

Table 1: Missing LSA-SAF *ET* data. These data are not available in the LSA-SAF website, so gap filling is done by linear averaging of the available maps of the days before and after the missing day.

S.no.	Year	Month	Days of missing data	Total number of days missing
1	2012	January	01,20,30,31	4
		February	21	1
		March	04	1
		September	01, 5-12, 24, 25	11
		November	20, 30	2
2	2014	May	31	1
Total				20

After filling the missing days, the representative *ETsat* corresponding to Trabadillo ADAS is derived by interpolating in MATLAB. Then the judgment is done by computing the RMSE and other error parameters described in section 3.4.2. The LSA-SAF DMET product is an actual *ET*, and the ground *ET* measurement in the Sardon Catchment ADAS is a reference evapotranspiration (*ET*), which is converted to PET when used as input to the Sardon Catchment model. So, the plots of *ETsat* and the actual *ET* equivalent of the model outputs expressed as a sum of GW evapotranspiration (*ETg*), unsaturated zone evapotranspiration (*ETun*) and interception (*I*) is used to check the consistency of the satellite *ET* measurement.

3.6. Model simulation with spatiotemporally variable driving forces

A three stage model calibration (steady state, a warming up, and a transient), has been done for Sardon Catchment (SC) by Weldemichael. (2016) using *P* and potential *ET* driving forces from Trabadillo Automatic Data Acquisition System (ADAS). The state variables were observation heads and the calibrated variables are K_H, K_V, S_Y, and SS. In addition, a post calibration transient simulation was done with spatiotemporally variable UZF1 driving forces. The UZF1 package inputs: crop coefficient (kc), interception rate (*I*) and root extinction depth (EXTDP) that were assumed as spatially invariant even when the transient model was calibrated are spatiotemporally variable in this simulation. The three land covers (*Qp, Qi* and bare/grass) are assigned different Kc, *I* and EXTDP. The Kc for *Qp*, *Qi*, grass and bare land are 1, 1, 0.75, and 0.61 respectively, while the EXTDP is taken as 10, 15, 1.45, and 0.5 meters respectively (see Fig. 15 for the cover the land classes). Therefore, the temporally variable PET and infiltration rate are made spatiotemporally variable as well by multiplying with spatially variable Kc and interception loss rate for the land use cover classes by Reyes-Acostaa & Lubczynski (2013).

Table 2: Groundwater budget for spatially uniform and spatio-temporally variable driving forces for the entire model domain, by Weldemichael (2016).

Budget components	Model solution with:			
	Spatiotemporally variable driving forces (all units mm day^{-1})		Spatially uniform driving forces (all units mm day^{-1})	
	IN	**OUT**	**IN**	**OUT**
Change in storage	1.06	0.68	0.93	0.70
Head dep bounds	0.00	0.02	0.00	0.03
Stream leakage	0.06	0.35	0.05	0.47
GW Evaporation	0.00	0.85	0.00	0.52
Gross recharge	1.08	0.00	1.18	0.00
GW Exfiltration	0.00	0.28	0.00	0.44
Total IN-OUT	2.19	2.19	2.16	2.16
IN-OUT		0.00		0.00
Percent Error		0.00		0.00

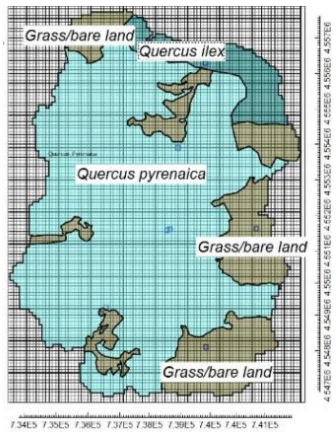

Figure 15: Land cover classes of SC (3 cover types: *Qi*, *Qp*, and grass/bare land) adopted from Weldemichael, (2016), defined for spatiotemporal model simulation.

The interception loss rate is calculated applying Equation 11.

$$I = P*(I_f*A_f+I_{other}*A_{other}) \quad (11)$$

where *I* - canopy interception per grid cell (mm day^{-1}), *P* - precipitation (mm day^{-1}), I_f & I_{other} - interception loss rate by forest and other land covers (%) respectively, and A_f & A_{other} - area of forest and area of other land cover respectively.

The water budget components have shown significant differences when the transient model is simulated with spatially uniform and spatiotemporally variable driving forces (look Table 2). However, this was done for one year only (2014). Therefore, in the present study, the transient model is simulated with spatiotemporally variable driving forces for additional 3 years (2011 to 2013). This is done in order to have a better *Rn* estimate for Sardon Catchment, so as to derive a better *Rn* for upscaling it to the DMHR.

In order to see the effect of using in-situ and *Psat* & *ETsat* product inputs in GW recharge estimation, the transient model can be simulated with *Psat* & *ETsat* from remote sensing under the same model settings by Weldemichael. (2016) in model muse environment. But this is not in the scope of this study. The model has been validated using one year's data (2014). Therefore, in this study, no validation is done after simulation of the model by applying spatiotemporally variable data. In future studies, supplementary recharge estimates by other techniques can be used as verification.

Fig. 16 describes the schematic representation of the scope of work with regards to Sardon Catchment model. The blue colour represents simulation by applying spatiotemporally variable model inputs.

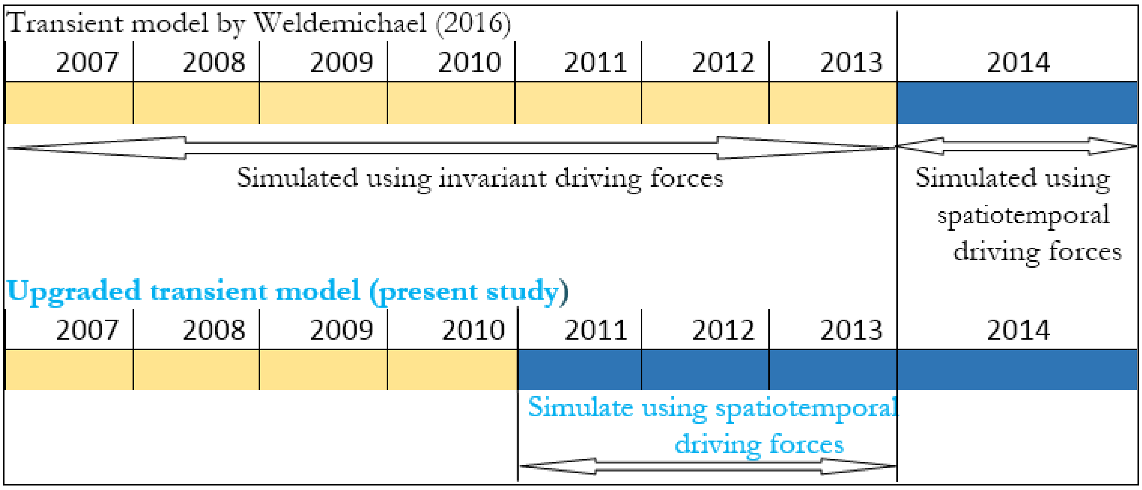

Figure 16: Schematic representation of Sardon Catchment's model upgrading (numbers show years).

3.7. Scaling up net recharge of Sardon Catchment into dehesa (montado) hard rocks

In order to scale up the net recharge (*Rn*) from SC model to DMHR, the recharge upscaling function (RUF) is defined based on the correlation/regression of the model output fluxes (like the *Rg*, *Rn*, *ETg*, and Exf_{gw}) of SC and its satellite-based *Psat*, *ETsat* and PR (*Psat* - *ETsat*) at Trabadillo ADAS station. So the pairs of the daily model and satellite fluxes that result in most significant correlation/regression are used to define RUF. Finally, the satellite-based fluxes (*Psat*, *ETsat*, and PR) of DMHR, which are spatiotemporally variable, changed to *Rn* using the recharge upscaling function (RUF).

The recharge potential (PR) for Trabadillo ADAS station is calculated by subtracting the daily *ETsat* from the daily *Psat* of the same location, i.e., as (*Psat-ETsat*). The spatial resolution of the daily *Psat* for the study area is 5 km, and that of the *ETsat* (DMET) product is 3.1 km (Fig. 17). The squares in blue colour in the Figure represent *Psat* pixels and the squares in red represent *ETsat* pixels. The SC is in covered by 9 *Psat* pixels. One pixel of *Psat* is in turn covered by 9 (1 full and 8 partial) *ETsat* (DMET) pixels. The representative *Psat* and *ETsat* for Trabadillo ADAS station are derived by the interpolation of the daily (year 2011 to 2016) *Psat* and *ETsat* (DMET) maps of DMHR with respect to the geographic coordinate location of the station in MATLAB. This has been mentioned in sections 3.4.2 and 3.5). Then recharge potential of the WLHR of the dehesa (montado), the DMHR, is estimated by subtracting the DMET maps of the DMHR from the CHIRPS (*Psat*) maps of the same area.

Three interpolation methods (linear, spline, and cubic) are applied to select a representative estimate of *Psat* & *ETsat* corresponding to Trabadillo ADAS station. The accuracy of the interpolation results is judged by plotting the against the *in-situ* rainfall (*P*) and model *ET* respectively and calculating the analytical ME, MSE, MASE, and RMSE. Then, the PR is the difference of these two daily fluxes (*Psat* - *ETsat*). Whereas the PR for the DMHR is calculated by first resampling the DMET (*ETsat*) pixels to the CHIRPS pixels and then subtracting the resampled daily *ETsat* maps from the daily CHIRPS maps. The resampling may introduce errors to the *P* and *ET* estimates of the *Psat* and *ETsat*. However, the analytical error calculations can give an indication whether the interpolated values match the measured values. Both the resampling and map calculation is done by writing codes in MATLAB.

Following the above, the potential recharge (PR) for Trabadillo ADAS is calculated by subtracting the interpolated DMET (*ETsat*) from the *Psat*. Then the PR for DMHR is derived by subtracting its *ETsat* (DMET) maps from the *Psat* using MATLAB.

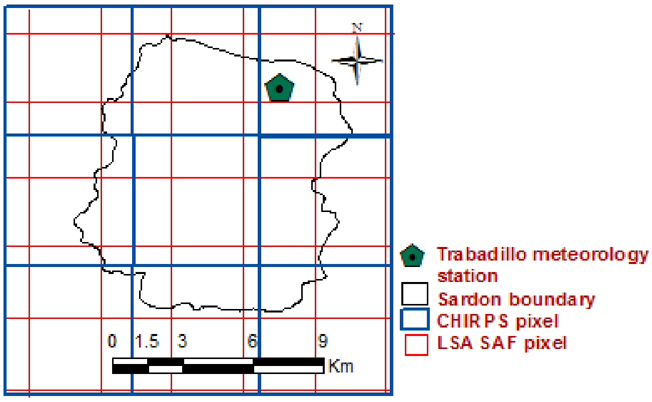

Figure 17: CHIRPS rainfall (*Psat*) and DMET (*ETsat*) pixels of Sardon Catchment. The lighter colours represent larger values of *ETsat* than the darker colours. The pink lines show the CHIRPS (*Psat*) pixels.

Finally, a mathematical relationship between the recharge derived from Sardon Catchment model calibrated by Weldemichael (2016) that is also upgraded in the present study and the PR calculated as satellite *Psat* - *ETsat* is defined. The resulting mathematical correlation/regression is the recharge upscaling function (RUF), based on which the *Rn* of SC is scaled up to the DMHR areas in the IP.

The mathematical relationships between the model input fluxes (independent variables) and the output fluxes (dependent variables) are expressed in different ways. The input fluxes include *Psat* and DMET (*Psat*) and the output fluxes from the model include like the *Rg*, *Rn*, the *ETg*, and GW exfiltration (Exf_{gw}).

Brunner et al. (2004) defined the water balance of a volume of soil to be expressed as:

$d\,\partial\theta/\partial t = P - ET - Q - R$………………………………………………………………………………. (12)

where *P* is precipitation (mm year^{-1}), *ET* is evapotranspiration (mm year^{-1}), d is the height of soil cube, $\partial\theta/\partial t$ is a change of soil moisture storage per time, Q is a surface runoff (mm yr^{-1}), and R is recharge rate. If the computation is done for several years, the term on the left side of the Equation 13 approaches to zero. In addition, river inflows and outflows from the catchment are assumed to balance each other (runoff is neglected) in this study.

If $d\,\partial\theta/\partial t = 0$, then $P\text{-}ET = Q + R$. Additionally, in this study, *Q* coming into the catchment and going out of it are assumed to balance one another. is assumed to be This implies that $P\text{-}ET \sim R$, where if present the Q would appear as a noise affecting the linearity of the relationship between P-ET and R

Therefore, Equation 13 can be rewritten as:

$PR = Psat - ETsat$ …………………………………………………………………………………………. (13)

where PR is the potential recharge, *Psat* is the precipitation, and *ETsat* is evapotranspiration.

In addition, the water that reaches the aquifer and moves down to ground water recharge zones (the net GW recharge) is illustrated as follows (Hassan et al., 2014);

$Rn = Rg + Exf_{gw} - ETg$ ………………………………………………………………………………….. (14)

where *Rn* is the Net Recharge, *Rg* is Gross Recharge, Exf_{gw} is groundwater exfiltration, and *ETg* is groundwater evapotranspiration.

If the groundwater exfiltration is excluded in Equation 14, then the equivalent term for *Rn* is the effective recharge (*Re*) that is shown in Equation 15.

$Re = Rg - ETg$ ………………………………………………………………………………………….... (15)

Therefore, considering the above mathematical relationships between the model output fluxes and satellite-based independent variables, the correlation/regression analyses are done in MATLAB. The correlation in this study is done using a linear and polynomial fitting. The linear fitting is preferably tested, then if the R^2 is found to be low the polynomial fitting with smallest possible degrees of freedom is tested. In fitting the polynomial curve the "robust method" option in the MATLAB is set to bisquare. There two "robust method" options: LAR and bisquare. The LAR method minimizes the absolute difference of the residuals so that extreme values have less influence. The bisquare gives weight to each data depending on how far the point is from the fitted line. Therefore bisquare is used to include all values as much as possible. All the correlations are tested with a confidence interval of 95% ($P \leq 0.05$).

The correlation/regression between *Rg* & PR, *Rg* & *Psat*, *Rg* & *ETsat* is tested to define the RUF from the most significant combination of the *Psat* and *ETsat* variables that affect the *Rg*. Similarly, the correlation between *Rn* and these remote sensing based variables is tested. The correlation test is done at three temporal scales (daily, 10 daily and monthly). So, depending on the significance of the resulting correlation, *Rg* or *Rn* is be scaled up from Sardon Catchment to the DMHR. Another option that is considered is to scale up *Re*. The *Re* is scaled up provided that there is a strong correlation between *Psat* & *Rg* and *ETsat* & *ETg*. Then the principle of proportionality can be applied between PR and *Re* that have been expressed in Equations (13) and (15) respectively. This means, if $Psat \propto Rg$ and $ETsat \propto ETg$, then $PR \propto Re$. Therefore, if the correlation is strong enough, *Re* can be expressed as in Equation (16).

$Re = Rg - \beta * ETsat$ …………………………………………………………………………....... (16)

where, β is the proportionality constant that can be derived from the correlation of *ETg* & *ETsat*, provided that their correlation is strong.

In addition, relationship *Rg* and *Rn* with *Psat* and *ETsat* was tested by regressing the cumulative of the latter two against the former two.

Another approach that is followed is applying multiple regression between *Psat*, *ETsat*, against *Rg* and the previous two against *Rn*. This is important because both *Psat* and *ETsat* affect the net recharge (*Rn*). Apart from this, the correlation is tested on a logarithmic scale of the variables and their errors (deviation from the ground measurements). This is because logarithmic plot can sometimes have more uniform distribution than the non-logarithmic plot (Webster and Oliver, 2008).

The analysis to determine the relationship between *P* and recharge (Moon et al., 2004) indicates that the correlation between the two increases when cumulative *P* is used. This is due to the time required for the *P* to reach the groundwater (time lag). Based on this the correlation between the cumulative *Psat* of Trabadillo station and the *Rg* & *Rn* is tested.

In this study, the focus is given to scale up *Rn*, rather than *Rg*, provided that the correlation is significant. This is because the *Rn* is more supportive in the management of GW resources (Lubczynski and Gurwin, 2005). This is because the *Rg* doesn't include the *ETg* and Exf_{gw} that reduce and non-linearize the recharge coefficient from *P*.

After scaling up and producing *Rn* maps for DMHR, presence pixels with exaggerated values are checked using conditional statements in MATLAB, by putting a threshold of $Rn \geq$ PR as outliers.

THIS PAGE IS BLANK

4. RESULTS AND DISCUSSION

4.1. Definition of the study area

The hard rock areas are found mostly in the west of the IP, excluding some parts in the central west of Portugal (see Fig. 18). The Iberian Massive (shown in Fig.6a) constitutes most of these areas. The arid areas are found in the southwest, central and the eastern parts of the IP excluding the north (Fig. 19)

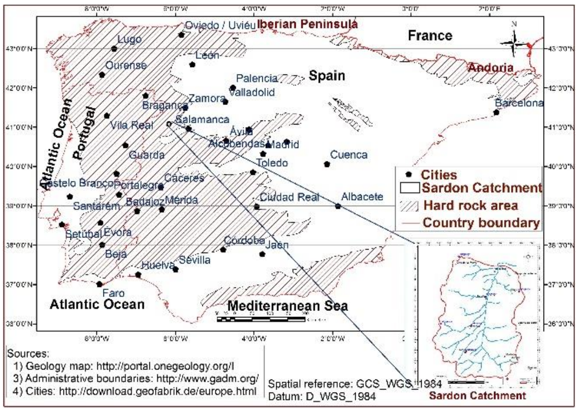

Figure 18: Hard rocks (HR) map of the DM. The hashed areas are HR areas. The HR are digitized from a geological map prepared by the USGS & a supplementary information from a simplified hard rock map prepared by the British Geological Survey.

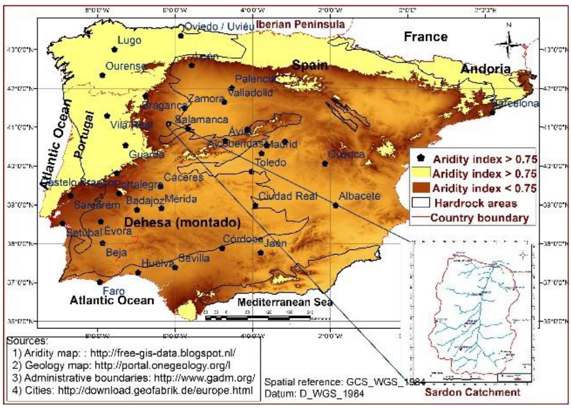

Figure 19: Water limited and non-water limited areas of the DM, classified applying a threshold of aridity. Aridity index < 0.75 is water-limited & vise verse. The brownish colour represents water-limited areas & the yellow represents non-water limited.

From the combined HR and water limited areas map (Fig. 20), clusters of areas on the northeast and south of the IP are excluded, as they are close to the Mediterranean Sea. In addition, small areas in the central north part are excluded. So, the large area that includes the west and southwest parts of the DM is considered. At last, this map is buffered by 10 km from the Atlantic Ocean (see Fig. 21) to define the final DMHR because the recharge may be affected by the ocean.

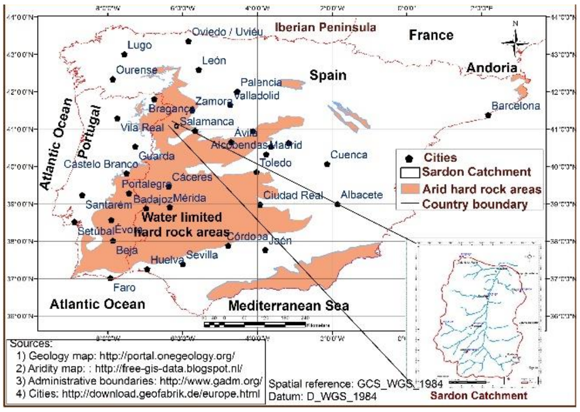

Figure 20: Water-limited hard rock areas (WLHRA) of DM defined by combining the HR map and the water-limited areas. Areas in salmon colour are WLHRA.

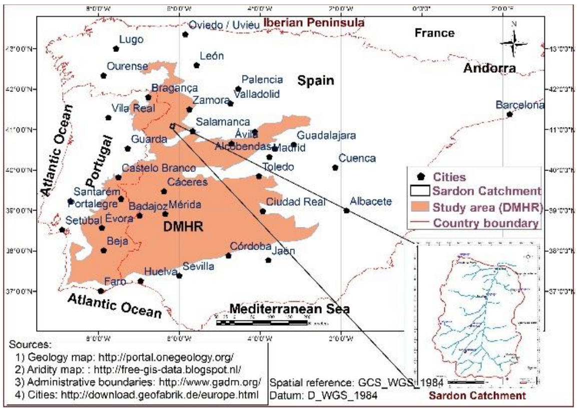

Figure 21: DMHR map (study area). Clusters of areas in the northeast are neglected. Then areas in the southeast and far northeast that are close to the Mediterranean Sea and the Atlantic ocean are buffered by 10 km to define the final DMHR map.

The DMHR area includes areas in four drainage basins of the IP, namely: Tagus, Duero, Guadiana, and Guandaliquivir basins. The rivers in these basins flow from east to west, i.e., to the Atlantic (see Fig. 22).

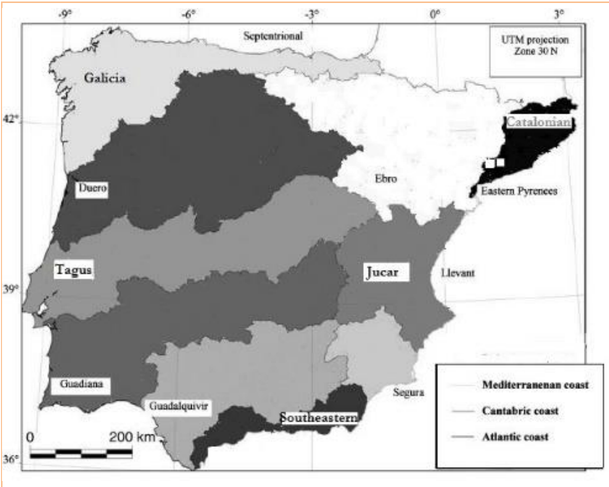

Figure 22: Iberian Peninsula drainage basins taken from Ninyerola *ET* al. 2007 with additional editing. The water limited dehesa (montado) hard rock (DMHR) area comprises mostly the, Guadiana, and Guadalquivir basins.

4.2. Spatiotemporal rainfall (*Psat*) over dehesa (montado) hard rocks

4.2.1. CHIRPS rainfall (*Psat*) accuracy analysis

Based on the bias analysis, the *Psat* for the daily records of Trabadillo ADAS station has -18% overall bias; in which 42% is F, -76 % is M, and 16% is H. This tells us that the *Psat* has generally underestimated *P* by 18%. In addition, bias correction may account for the 16 % of the total biases, i.e., the H (Fig. 23 left). The mean F, M, H, and total biases are 0.63 mm, -1.13 mm, 0.23 mm, and -0.27 mm (Fig. 22 right). This shows that the *Psat* product for DMHR has overall underestimated the *P* measurement by 0.27mm per each measurement (in the years 2011 to 2014).

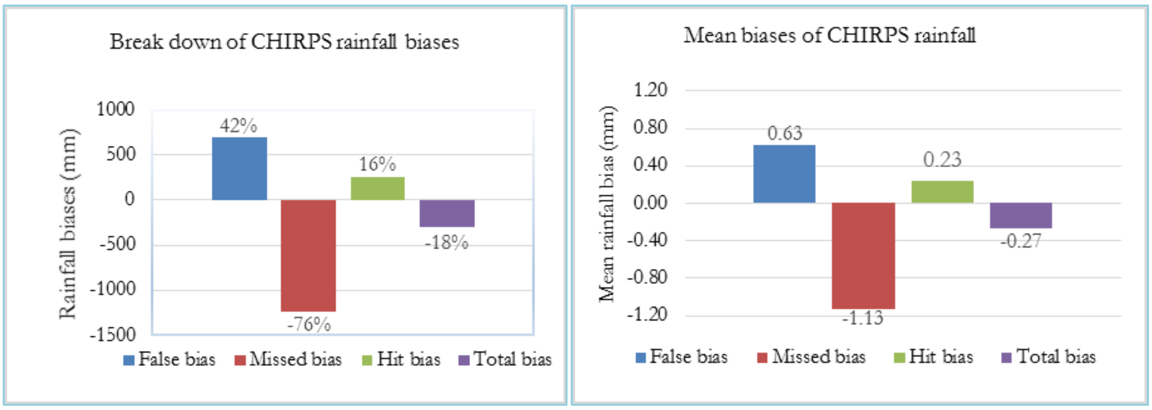

Figure 23: Bias decomposition of CHIRPS satellite rainfall product: actual bias (left) and mean bias (right); calculated as the difference between the representative temporal (daily) satellite estimates for Trabadillo station (derived by interpolation in MATLAB) and its corresponding *in-situ* (ticking bucket rain gauge) measurement.

The bias decomposition of *Psat* shows the dominance of F and M. This agrees with the study by Yong et al. (2016) that indicates the prevalence of F and M in arid and semi-arid regions than H bias. For this reason, bias correction test of the CHIRPS has not improved the accuracy of *P* estimate. The RMSE of the *Psat* pixel (representing SC ADAS station) tested for bias correction and its in-situ *P* measurement is found to be larger than the pixel without bias correction. The lowest RMSE for the moving window and sequential window are 6.1 mm at a window size of 3 days, and 6.6 mm at a window size of 7 days respectively. The RMSE of the bias uncorrected *Psat* is, however, 5.7 mm (labelled in green in Fig. 24). Therefore, for both window types (sequential and moving) and of all the window lengths (3, 5, …, and 31) that are tested in this study, the RMSE is larger in the pixel tested with bias correction than without correction (See Fig. 24). This means the bias correction of CHIRPS product for the study period did not improve the accuracy of its *P* estimate

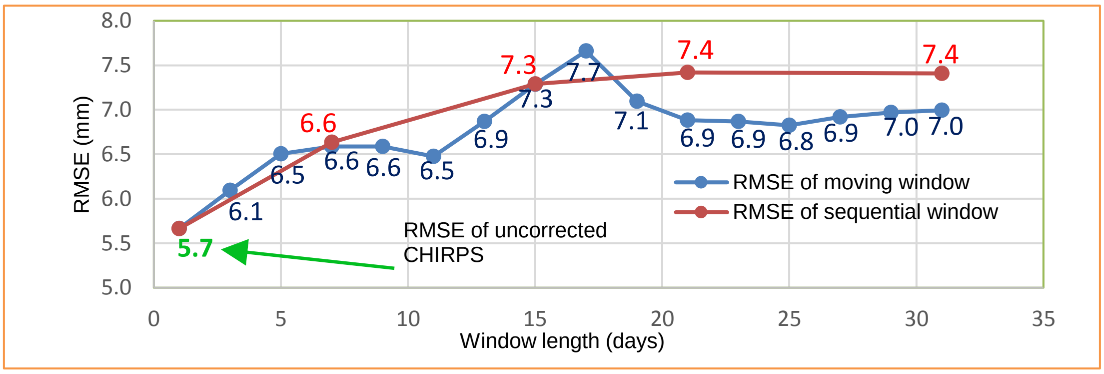

Figure 24: RMSE between SC ADAS station daily rainfall record and *Psat* tested with and without bias correction for a moving and sequential windows of varying sizes (days). The RMSE is higher for *Psat* estimates tested with bias correction. The blue line is RMSE for moving window and the brown is for sequential window.

Therefore the representative *Psat* for the Trabadillo ADAS station is defined by MATLAB interpolation. The RMSE of the nearest and cubic interpolation interpolations of *Psat* with respect to Trabadillo in-situ *P* measurement are found to be resulted in of 6.6 mm and 5.7 mm respectively. The spline interpolation resulted in completely different values. Based on this the *P* estimate by cubic interpolation is adopted as the representative *Psat* for Trabadillo ADAS station.

4.2.2. Spatiotemporal distribution of *Psat*

The spatiotemporal *Psat* over DMHRs generally increases from east to west. It is also higher in the central eastern part. The increase in the central east part is related to higher elevations in those areas. In general, *Psat* in the DMHR is higher in high elevation areas (see Fig. 26 and Fig. 4 section 2.1.4). Topography has a strong influence on *P* patterns, in that it can affect both local wind patterns and condensation of precipitable water (Basist et al., 1994). In addition, topography can have an impact on *P* of an area by the enhancement of orographic *P*. Therefore *P* is usually higher in high elevation areas which have even similar geographic locations. In line with this, Chu (2012) justifies the dependence of the spatial distribution of *P* on elevation, and Fernández-Montes et al. (2014) indicates the dependence of inter-annual variability of extreme *P* days on the frequency of synoptic circulation types for the western the IP and high altitude stations. According to the study, the relationship of elevation with extreme *P* of short duration is stronger than for long durations.

Seasonally, the *Psat* in DMHR for the years 2011 to 2016 is higher in months Jan to March & Nov followed by Sept to Dec. The months June to Sept are the driest months. However, some showers occur in Sept. The seasonal variability of *P* in the study area is affected by incursions of fronts from the southeast (the Mediterranean), the southwest (the Atlantic), and the north (the Bay of Biscay). Due to this influence, the south and southwest part of the DMHR areas are nearly completely dry in the months July and Aug (see Fig 26). The month June is no different as well. This coincides with the finding of the study by Fernández-Montes et al. (2014) that concluded diminishing of extreme *P* days in the West and south of the IP mainly due to a declining incidence of cyclonic southwest flow. In contrast, the period from Oct to Feb is wet due to the movement of active Atlantic frontal systems. This phenomenon agrees with Sumner et al. (2001), which is a study made on the seasonality of *P* in the eastern and southern Spain based on 410 sites of monthly *P* values from 1964 to 1993. Additionally, the Guandiana basin, comprising south and southwest of DMHR, (see Fig. 22) is drier and hotter as compared to other areas in the IP due to the Atlantic influence (Costa et al., 2011).

The findings of this study show that the overall seasonal variability (monthly variation in a year) of *Psat* is higher in the southern part of the study area. It can be seen from Fig. 26 that the monthly variations in the whole study period are higher in the south than in other parts of the study area. As a result of a greater concentration of *P* during the cooler part of the year, the months January to March become drier and October to December wetter. The study by Sumner et al. (2001), which has used the seasonality variation index derived by Walsh & Lawler (1981) explains this variation. The study used an index through the 30-year period with a linear regression on 5-year running means and indicates that the seasonality increases in the south (Andaluciá). Space–time analysis of the inter-annual irregularity of *P* in the IP (García-Barrón et al., 2015) as well complements the findings in this study. The study is based on monthly *P* data from 1940 to 2010 from scattered 500 Spanish meteorological stations and indicated that the Guadalquivir basin (Fig. 22), a basin in the southwest part of Spain, shows the greatest Inter-annual variability of *P* in Spain. Similar variability is shown in the present study (Fig. 26). This spatiotemporal variation of *P* has a direct influence on the spatiotemporal variability of *Rg* and *Rn* in the area. Refer Table 3 & 4 for the seasonal variations of *Psat* in the present study.

The year 2013 and 2016 have shown a different spatiotemporal distribution of *Psat* with relatively higher annual *P* most of it concentrating in March and January respectively. The year 2013 shows lower occurrences of *Psat* in Sept & Oct as compared to other years. (see Fig. 26 & Table 3). This is because of unevenness of *P* patterns in semi-arid climates, sometimes with extreme daily *P* amounts approaching annual total *P* (Wheater et. al, 2008), and the standard deviation of the mean annual *P* surpassing the mean value (Mays, 2009). Usually, *P* shows a replica of decadal or a certain number of years, with a maximum and minimum at a certain period of time common to the specific area.

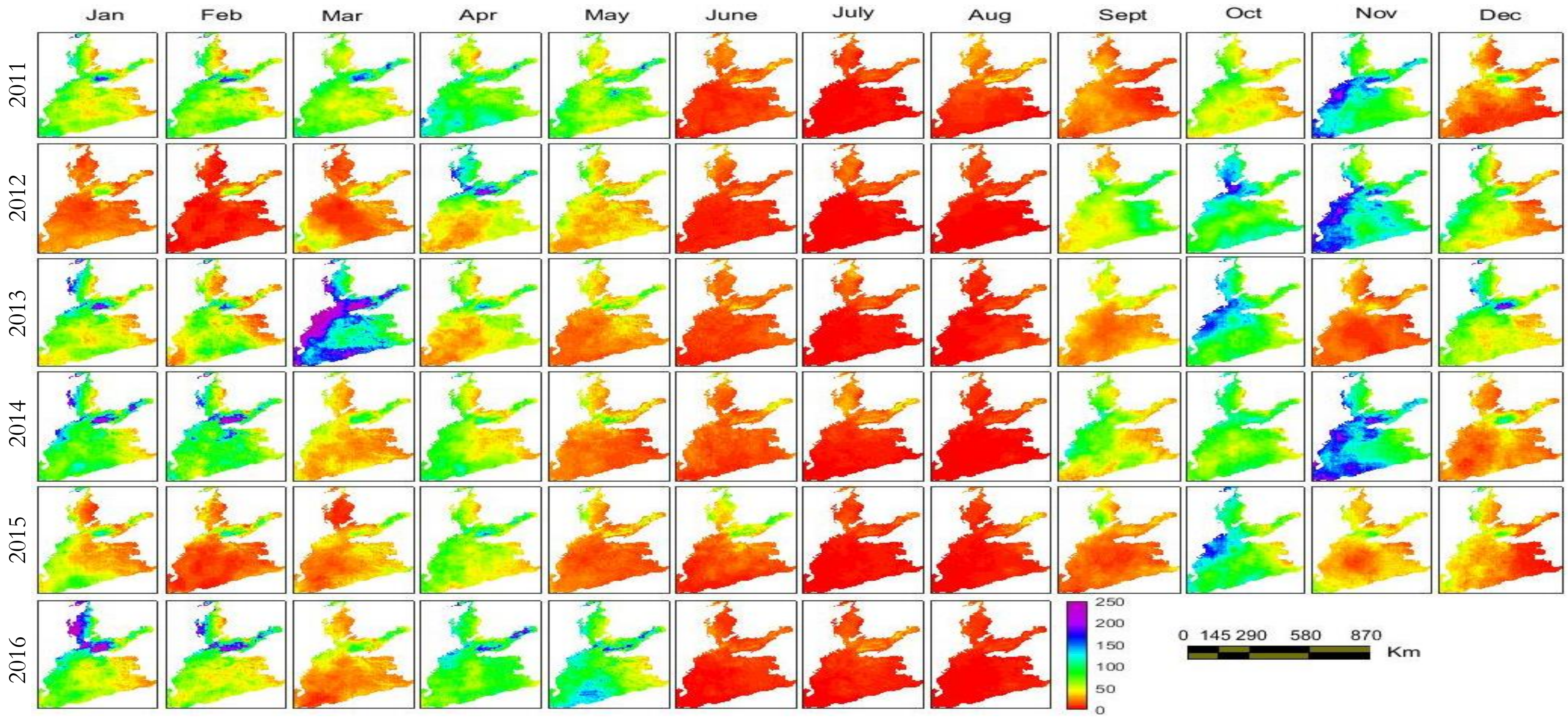

Figure 25: Spatiotemporal satellite-based monthly rainfall (*Psat*) maps of dehesa (montado) water limited hard rock (DMHR) area in years 2011 to 2016. The daily satellite-based CHIRPS rainfall product (*Psat*) is downloaded from the http://chg.geog.ucsb.edu and subseted to the DMHR applying batch processing tools in GIS softwares. The daily maps (mm day^{-1}) are aggregated to monthly (mm month^{-1}) in MATLAB. The final maps are as well produced in MATLAB The dry season (June to Sept) show no rainfall (except small amount in Sept and very limited areas in Jul and Aug). The central eastern parts of the maps are high rainfall areas.

Table 3: Spatiotemporal monthly total maximum, minimum, mean, and standard deviation (SD) of satellite -based rainfall (*Psat*) in dehesa (montado) hard rock (DMHR) area. These are extracted from the monthly total maps (mm month^{-1}) that are aggregated from the daily (mm day^{-1}) *Psat* maps of the DMHR area. The max or min means the highest monthly total rainfall value in any part of the DMHR area. The mean is the average monthly flux (mm month^{-1}) of the DMHR for the given month and year.

Month	Year 2011 (mm month^{-1})				Year 2012 (mm month^{-1})				Year 2013 (mm month^{-1})				Year 2014 (mm month^{-1})				Year 2015 (mm month^{-1})				Year 2016 (mm month^{-1})			
	Max	Min	Ave.	SD	Max	Min	Ave.	SD	Max	Min	Ave.	SD	Max	Min	Ave.	SD	Max	Min	Ave.	SD	Max	Min	Ave.	SD
Jan	223	18.9	77.3	38	89.3	5.7	33.7	18.7	316	15	92.3	51.3	273	24	104.2	50.7	178	6.6	54.4	30.3	427	20	123.2	76
Feb	241.4	3.2	79.2	41	89	0	28.1	18.6	257	2.3	67	39.4	353	6	110.3	60.7	149	2.4	48.3	31.2	384	6.6	104.4	60
Mar	196	28	86.4	36.9	86.1	0	35.9	18.4	416	49.5	168.5	70.3	61.2	0	22.5	13.7	35.4	0	13.4	8.2	42	0	18.3	10
Apr	168.3	19.4	86	32.9	279.5	18	96.9	50.6	174	16.7	66.2	32.2	146	23	69.6	26.6	186	23	72.3	29.8	256	37	103.8	41
May	189.9	30.1	80.2	31.3	155.2	16	52.9	22.3	126	12.4	50.7	24.8	108	7.4	40.5	21.8	102	8.7	37.6	18.4	218	28	96.1	38
June	44.5	0	20.9	10.1	67.3	0	21	12.4	47.9	3.9	22.4	10.8	86.1	5.1	27.7	14.6	115	0	42.5	23.7	42	0	16.5	9
Jul	38.9	0	14.3	8.3	34.5	0	15.2	8.1	44.7	0	17.6	10.3	61.2	0	22.5	13.7	35.4	0	13.4	8.2	42	0	18.3	10
Aug	60.6	0	23.9	13.9	27.4	0	12.2	6.4	37.4	0	13.6	8	40.2	0	14.9	8.8	64	0	22.6	15.6	29	0	11.5	7
Sep	47.2	0	22.2	10.4	141.8	22	69.1	27.2	81.7	13.5	40.4	15.7	135	18	68.4	28.8	85.9	0	39.7	20.9				
Oct	109.8	16	57.1	22.4	206.1	29	105.1	39	199	23.2	103.2	40.1	139	28	78.7	25.5	189	23	99.5	41.3				
Nov	239.9	33.5	114.4	45.4	237.2	30	121.7	45.1	68	5.5	28.3	14.9	252	45	127.9	43.6	10.8	95	42.2	19.1				
Dec	128.8	3.7	41.1	25.9	210.9	10	66.1	34.2	248	23.2	88.5	44.3	126	7.4	44.9	26.8	137	0	39.6	23.6				
Annual mean			58.6				54.8				63.2				61.0				43.8					61.5

The contribution of the dry season (June to Sept) *P* to the total annual *P* ranges from the highest of 14.9 % in 2015 to the lowest of 7.1% in 2013 (see Table 4). This finding matches with the study by Rodriguez-Puebla et al. (1998) that indicates the dry season contribution to be 12% of the total annual *P*.

Table 4: Dry season and wet season contribution of *Psat* from CHIRPS. These are calculated by taking: (i) the sum of dry season monthly mean *Psat* (June to Sept) (ii) sum of mean *Psat* for the rest of months in each year.

Year	Satellite-based rainfall (*Psat*)				Total rainfall (mm year^{-1})	
	Dry season (mm)	Dry season (%)	Wet season (mm)	Wet season (%)	*Psat* for DMHR	SC (in-situ)
2011	59.1	8.4	643.9	91.6	703.0	301.7
2012	48.4	7.4	657.9	100.0	657.9	431.1
2013	53.6	7.1	705.1	92.9	758.7	702.9
2014	65.1	8.9	667.0	91.1	732.1	495.5
2015	78.5	14.9	447.0	85.1	525.5	N/A
2016	46.3	9.4	445.8	90.6	492.1	N/A

N.B. The last column for the year 2014 is up to Sept.

4.3. Spatiotemporal evapotranspiration (*ETsat*) in SC and DMHR area

4.3.1. Temporal *ETsat* in SC

Like in the rainfall the representative *ETsat* for Sardon Catchment is derived by MATLAB interpolation. Accordingly, the cubic interpolation method that has lowest RMSE of 0.98 mm is adopted for interpolating *ETsat*. Generally, the *ETsat* for Trabadillo ADAS has underestimated *in-situ ET* measurement calculated as a sum of groundwater evapotranspiration (*ETg*), unsaturated zone evapotranspiration (*ETun*), and interception (*I*). It should be noted that model *ET* estimate is assumed to be accurate. The plotting is done for the time period of 2011 to 2014. This is because the model is simulated with spatiotemporally variant driving forces up to Sept 30, 2014. The maximum and minimum of the model *ET* and the *ETsat* is found to be 4.2 mm day^{-1} & 0.4 mm day^{-1} and 3.8 mm day^{-1} & 0 mm day^{-1} respectively. From Fig.27 it can be observed that inconsistencies of satellite *ET* measurement are more visible on the falling limb than at the rising limb. Nonetheless, the pattern of the variations in measurements is similar in the satellite and model estimates. This implies that the satellite *ET* product for the study area gives a good estimate, and it is acceptable to use it in this study. Therefore, a similar trend is expected in the whole study area.

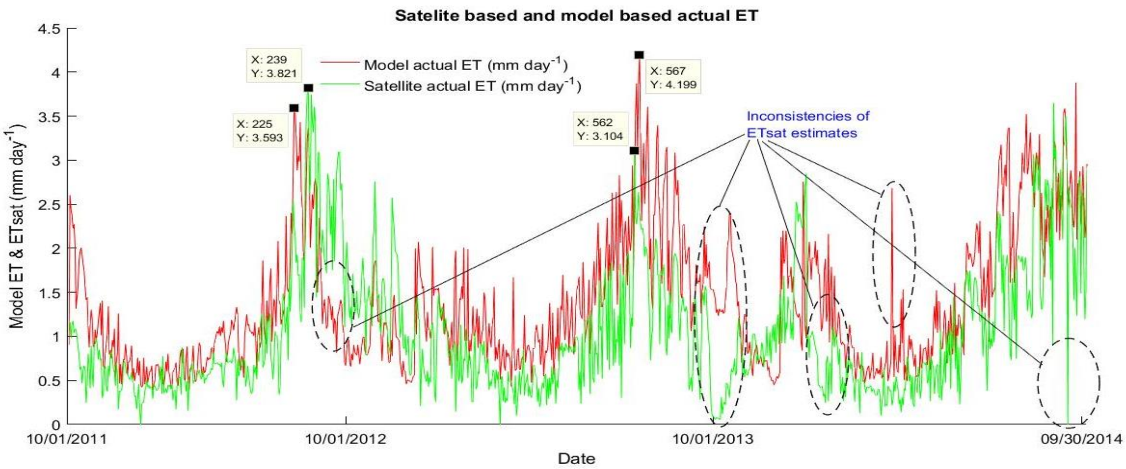

Figure 26: Comparison of the model (in-situ) & LSA-SAF satellite evapotranspiration (*ETsat*). The model *ET* is the output of the simulation with spatiotemporally variant inputs in this study. It is the sum of *ETg*, *ETun*, and *I*.

4.3.2. Spatiotemporal *ETsat* over DMHR area

The spatiotemporal *ETsat* is generally higher in areas where *Psat* is higher over the DMHR. It increases from east to west, however, there are also higher *ETsat* anomalies in the southwest of the study area (see Fig. 28) even in the dry season. This higher *ET* in the southwest can be attributed to the type of vegetation cover, which is dominated by evergreen *Quercus ilex* oak trees (Costa et al., 2011) that can transpire throughout the year. Interestingly, Costa et al. (2011) have indicated land use transformations involving the replacement of agricultural land uses and native oak woodlands by fast-growing Eucalyptus plantations in the southwest parts of the IP. Many studies show that Eucalyptus has high *ET* rate (e.g. the review article by Albaugh et al., 2013; Rodríguez-Suárez et al., 2011; Nosetto et al., 2012; Dzikiti et al., 2016; V, 1984) with deep roots that can tap GW even in the dry season. Therefore, this justifies the higher *ETsat* observed in the southwest parts of the DMHR while rainfall is low. Apart from this the Alcoutim area (AL), located in the Guadiana basin(southwest part), is drier and hotter (Costa et al. 2011).

The *ET* in the years 2011 and 2012 in general, particularly in March, is lower as compared to other years (see Fig. 28). This is because of lower *Psat* in these years (shown in Fig. 26 and Table 4). On the other hand, the monthly total *Psat* for the months June to August in years 2011 and 2012 is very low (< ~50 mm), though, monthly *ETsat* >50 are observed in some areas (see Fig. 28). This is due to the fact that deep-rooted trees (the *Quercus ilex*) can extract water directly from the groundwater (which is shallow in most of the DMHR areas. This is also observed in other years of the study periods in this research. The general trend is, however, areas with higher *ETsat* are areas with higher *Psat*. The reason is water availability accompanied by high solar energy acting on the surface results in higher *ET*. Due to this, *ETsat* is generally higher in the months of Mar to May, in which the rainfall is higher than the rest of the months and temperature is warm. However, high *ETsat* is observed as well in June and July throughout the study period in limited localities that receive rainfall.

The range of spatial maximum and minimum monthly total *ET* in the study period (Oct 2011 to Sept 2016) is from 133 mm month^{-1} that occurred in July 2015 to 0 mm month^{-1} that occurred in June to Aug respectively. The standard deviation ranges from 32.5 calculated for June 2013 to 2.7 that is calculated for Nov 2015. The range of spatial mean monthly *ETsat* is 57.3 mm month^{-1} in Mar 2013 to 0 mm month-1 tin Dec 2015 (Fig. 28 and Table 5). The highest annual spatiotemporal mean *ETsat*, calculated as the average of the mean monthly *ETsat* for the 12 months, in the study period is 33.1 mm year-1 that occurred in the year 2013 (see Table 5) and the lowest is 23.2 mm year^{-1} in the year 2012.

The maximum monthly *ETsat* (that occurred in some parts of the study area) as mentioned in the above is in Jul 2015. On the other hand, the month with the lowest *ETsat* is Dec 2015 (see Fig. 29 and Table 5), in which the whole study area has 0 mm month^{-1}. However, the spatiotemporal *Psat* map for this year shows *Psat* records. So the absence of *ETsat* is associated with very low temperature in this month.

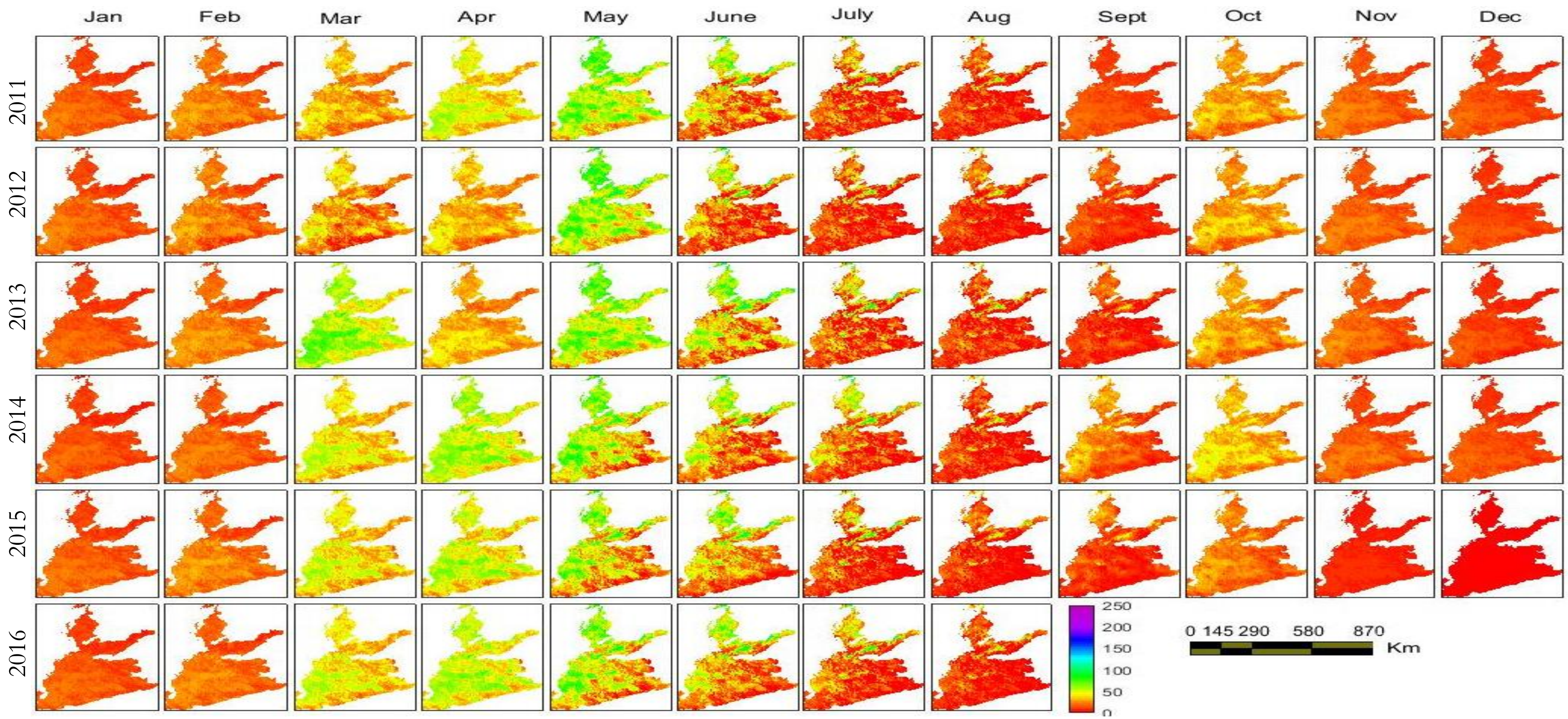

Figure 27: Spatiotemporal satellite-based LSA-SAF evapotranspiration (*ETsat*) of dehesa (montado) water limited hard rock (DMHR) area in years 2011 to 2016. The daily LSA-SAF evapotranspiration product (*ETsat*) is downloaded from https://landsaf.ipma.pt/ and subseted to the DMHR applying batch processing tools in GIS softwares. Then the daily maps (mm day^{-1}) are aggregated into monthly (mm month^{-1}) in MATLAB. The final maps are produced in MATLAB. The same classification range is used in these maps as in the rainfall maps (*Psat*) for ease of comparison between these two. The months Mar to May have higher *ETsat* than other months because of higher rainfall and temperature in these three months.

Table 5: Spatiotemporal monthly total (mm month^{-1}) maximum, minimum, mean, and standard deviation (SD) of satellite-based evapotranspiration (*ETsat*) in dehesa (Montado) water limited hard rock (DMHR) areas. The values are extracted from the monthly total *ETsat* maps that are aggregated from the daily (mm day^{-1}) *ETsat* maps of the DMHR area. The max or min means the highest monthly total *ETsat* value in any part of the DMHR area. The mean is the average monthly flux (mm month^{-1}) of the DMHR for the given month and year.

	Year 2011 (mm month^{-1})				Year 2012 (mm month^{-1})				Year 2013 (mm month^{-1})				Year 2014 (mm month^{-1})				Year 2015 (mm month^{-1})				Year 2016 (mm month^{-1})			
Month	Max	Min	Ave.	SD	Max	Min	Ave.	SD	Max	Min	Ave.	SD	Max	Min	Ave.	SD	Max	Min	Ave.	SD	Max	Min	Ave.	SD
Jan	29	4.8	16.1	4.3	30.4	4.5	16.9	5.17	29	4.9	16.7	6.5	24.6	3.4	14	6.1	29.7	5.2	17.2	6.9	26.6	4.5	15	4.5
Feb	37	5.6	21	6.3	39	2.3	20.6	7.3	36.6	5.5	20.7	8.6	30.5	5.6	17.6	6.9	36.5	5.4	20.6	8.8	32	5.7	19.3	5.8
Mar	53	9.7	29.1	9	60.3	0	27	12.8	92.1	22.1	57.3	18.7	68.1	12.8	40	14.7	69.6	11.9	39.6	15.6	69	12.4	40	11.1
Apr	73	17.5	42.6	10.9	57.4	4.7	30.7	9.3	51.4	10.1	30.2	11.1	87.3	8.5	49.7	20	79.7	12.2	46.8	18.1	83	10.5	48.4	12.2
May	113	10.2	54.6	17.9	123	7.9	55	19.6	107	4.6	53.3	25.9	114.9	0	50.2	29.4	112	0	49.2	28.8	111	0.3	43.6	21.4
June	126	0	31.5	20.9	123	0	26	19.5	129	0	55.3	32.5	121.3	0	50	29.7	121	0	51.4	30.5	121	23	31.8	20.5
Jul	112	0	20.2	16.5	104	0	17.5	14.7	125	0	48.3	29.4	117.6	0	49.3	29.4	133	0	46.8	29.4	126	0	22.2	18.3
Aug	86	0	14.4	12.2	80.3	0	14.3	11.9	92	0	36.3	22.6	82.2	0	33.8	20.6	79.9	0	32.1	19.7	79	0	13.8	11.7
Sep	53	1	12.2	7.7	52.6	1.4	12.8	7.2	55.2	0.3	23.6	14	61.9	1.9	27.6	15.2	60.6	0	25.8	15.2				
Oct	47	7	26.7	7.8	48.7	4.9	27.5	8.4	49	6.7	26.9	11	53.5	8.9	30.9	12.6	41.2	4.3	22.3	9.7				
Nov	30	7.1	17.9	4.7	27.3	5.6	17.3	4.5	30.6	2.8	16.9	7.7	27.2	5.5	16.4	6	12.3	2.7	7.5	2.7				
Dec	24	4.7	14.1	3.8	24.1	4.5	12.9	3.8	20.9	2.3	11.6	5.3	24.3	4.7	14.3	5.5	0	0	0	0				
Annual mean (mm yr^{-1})			25				23.2				33.1				32.8				29.5				29.3	

The dry season (June to Sept) *ETsat* contribution to the total annual ranges from the highest of 36.3 % of that occurred in 2015 to the lowest of 20.8 % in 2012 (see Table 6). So the dry season contribution of *ET* is higher than the dry season *P* contribution, indicating *ETg* contribution.

Table 6: Dry season and wet season contribution of *ETsat* from LSAF SAF. These are calculated by computing: (i) the sum of monthly mean total *ETsat* for the dry season (June to Sept) (ii) monthly mean total for the rest of months in each year. For the year 2016, only the first 8 months are taken.

Year	Satellite evapotranspiration (*ETsat*)				Annual *ET* (mm yr^{1})	
	Dry season (mm)	Dry season (%)	Wet season (mm)	Wet season (%)	*ETsat* DMHR	SC model *ET*
2011	78.3	26.0	222.0	74.0	300.4	256.9
2012	70.6	25.4	207.9	74.6	278.5	314.9
2013	163.5	41.2	233.6	58.8	397.1	422.2
2014	160.7	40.8	233.1	59.2	393.8	521.1
2015	156.1	43.4	203.2	57.6	359.3	N/A
2016	67.8	29.0	166.3	71.0	234.1	N/A

4.4. Satellite-based spatiotemporal potential recharge (PR)

4.4.1. Satellite-based potential recharge (PR) of Sardon Catchment

The plot of daily satellite-based potential recharge of Sardon Catchment (SC) and its model derived net recharge (*Rn*) shows similar pattern in some parts of the study period. The relatively similar patterns occurred towards the mid of 2013 and 1st quarter of 2014. Nevertheless, it shows inconsistencies in the period like in the 1st quarter of 2012 (see Fig. 30). These inconsistencies may arise from: (1) complex recharge processes in the unsaturated zone, (2) uncertainties in the *Psat* and *ETsat*, (3) uncertainties in the model estimate (calibration), and (4) the noise/error introduced by the run off and the groundwater exfiltration (Exf_{gw}) as well as groundwater evapotranspiration (*ETg*) shown in Equations 12 and 14 respectively. So these factors may increase uncertainties in the scaled up *Rn* into the DMHR by increasing the errors that can occur in curve fitting to derive the RUF. However, this is used to scale up if the significance correlation between these two fluxes is strong (details in section 4.6).

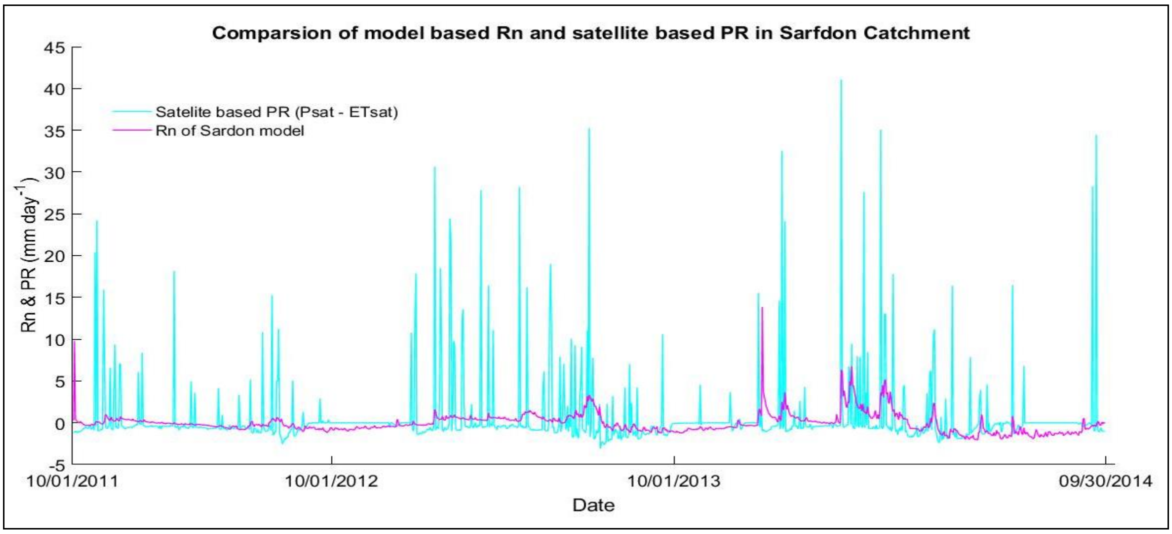

Figure 28: Relationship of daily (Octo 2011 to Sept 20114) *Rn* from Sardon model and satellite-based potential recharge (PR) corresponding to Trabadillo ADAS station.

4.4.2. Satellite-based potential recharge (PR) of DMHR area

The potential recharge (PR), calculated as *Psat* - *ETsat*, in the DMHR is expected to be generally higher in the years with higher *Psat* as rainfall has more influence on the PR than evapotranspiration. In line with this, the PR in the year 2013 (particularly in months March and April) is higher in most parts of the study area as compared to other years (see Fig. 31). The PR in many areas, particularly during the dry season (June to Sept), is generally found to be slightly negative or negative. This finding goes in line with a case study in Kalahari, Botswana in the proceedings of "International Conference on Water Resources of Arid and Semi-arid Regions of Africa" by Lubczynski & Obakeng (2004) that indicated negative recharge as a result of excess *ETg* than the recharge. In addition, this finding goes in line with the study by Obakeng et al. (2007) in the Botswana Kalahari, that indicated GW discharge to be less than the actual recharge. The negative PR is likely to result in negative *Rn*. Hassan et al. (2014) have found an occurrence of negative effective (*Re*) and *Rn* that approves as well the present finding. The PR in the whole study period usually increases while moving from east to west, where *Psat* also increases in this direction. Apart from this, areas in the central east part show high PR. This is also related to higher *P* in those areas. The PR is mostly low in the south and southwest, where low *Psat* & higher *ETsat* are observed (explained in sections 4.1 & 4.2). However, the 6 years average monthly PR (calculated as the average of all months for the whole study area in each year) for the study period (2011 to 2016) is positive, i.e., 23 mm (see Table 7).

The spatial maximum and minimum monthly total PR for the DMHR in the study period ranges from 417 mm $month^{-1}$ in Jan 2016 to -110 mm $month^{-1}$ in June 2012. Following Jan 2016, the highest monthly total PR is in Mar 2013, which is 402 mm $month^{-1}$. The standard deviation (SD) ranges from 55.8 in Jan 2016 to 8 in Aug 2013, showing high variability. In addition, the mean monthly PR ranges from 36 mm $month^{-1}$ (excluding the year 2016 as the PR is derived for 8 months) in the year 2013 to 10.5 in the year 2015. The low mean monthly PR in the year 2015 is because the *Psat* is not that high and the *ETsat* is, on the other hand, is comparable to other years (see Table 5 & 6). It is seen in Fig. 31 as well, particularly, the months Jan to May have lower PR relative to other years. In Jan and Feb the highest records of PR are found in the year 2016. On the contrary, the spatial mean in this year is the lowest (next to the year 2015 & more or less similar to 2012) in the study period. These results show that the spatiotemporal dynamics of GW recharge, in particular in arid and semi-arid environments, is not easily predictable (L. Zhang et al., 2002).

Despite the fact that many areas in the year 2012 show negative PR, its maximum, minimum monthly total PR is higher than in 2011 (see Fig. 31). The reason is because there is relatively higher *Psat* in January, February, and March 2011 (in which *ETsat* is low due to low temperature), so that many areas in these 2 months in 2011 have higher PR as compared to the year 2012. This has presumably made the maps for 2011 to have higher PR than in the year 2012. However, the mean monthly average for the year 2011 is lower than the year 2012 (see Table 5, 6 & 7). In other words, the volumetric PR is higher in the year 2012 than in the year 2011.

The dry season (June to Sept) spatiotemporal mean monthly total (total of the mean PR of each month) PR is -19.5 mm, 11 mm, 15.9 mm, 0.4, -11.1, and -38.6 mm in years 2011, 2012, 2013, 2014, 2015, and 2016 respectively (Tables 8). It contributes from a maximum of 15.9% to a minimum of -38.6%. This shows that the dry season PR is mostly negative in the DMHR areas. This may indicate that the GW is losing water during the dry season as a result of tree transpiration that taps ground water with their deep roots. From Tables 5 & 6 it can be seen relatively higher *ETsat* than *Psat*. In other words, there is the occurrence of *ET* while the *P* is very little or zero (refer Table 6). This means the *ETg* is contributing to the total *ET* during the dry season, and *P* is not contributing to recharge in these years. This agrees with the study by Hassan et al. (2014). Therefore, this will result in low and/or negative *Rn* in the area. The wet season PR is 300.4 mm, 221.5 mm, 416 mm, 289.9 mm, 137.6 mm, and 191.4 mm for years 2011 to 2016 respectively. This shows the wet season contributes nearly all the PR in the DMHR areas.

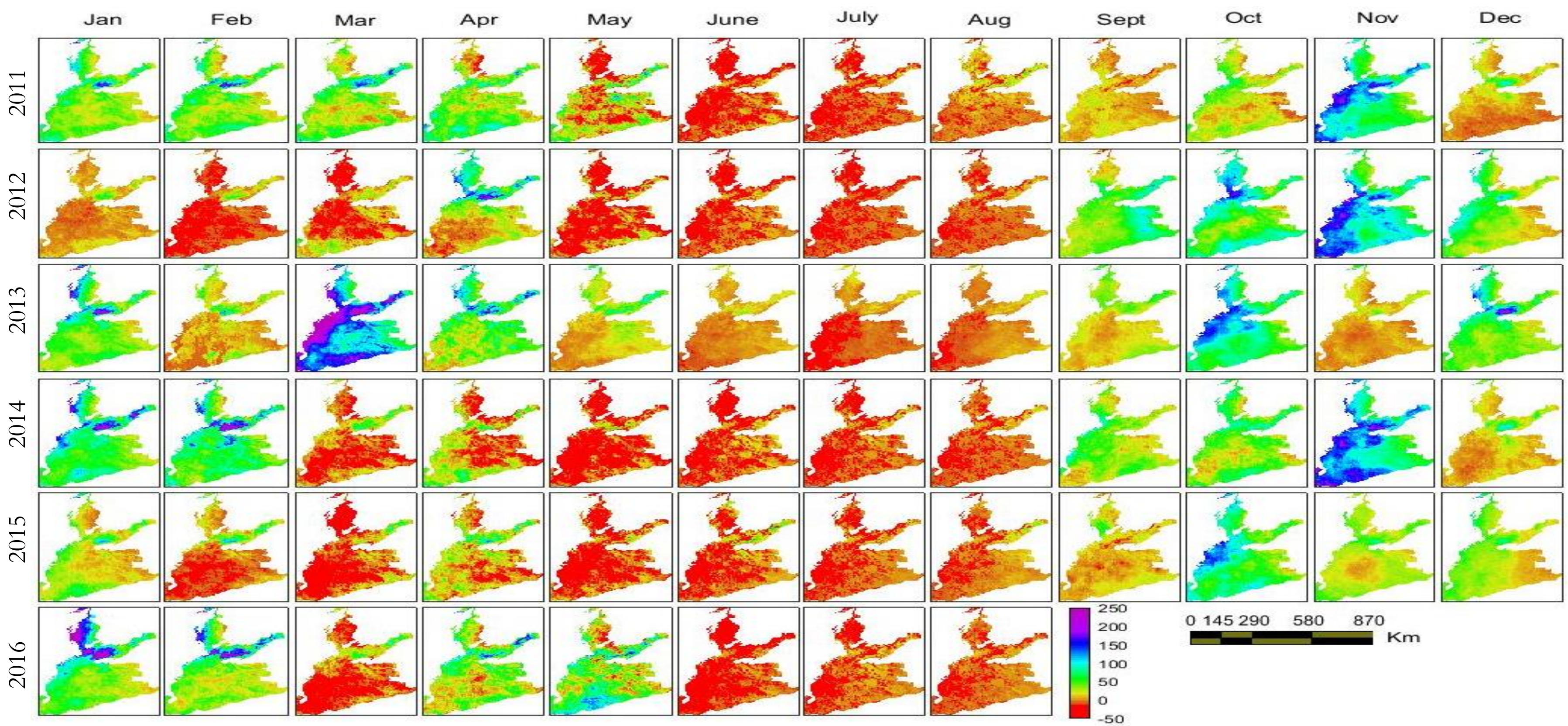

Figure 29: Spatiotemporal monthly satellite-based potential recharge (PR) of DMHR area for the years 2011 to 2016, derived as daily (mm day^{-1}) CHIRPS rainfall minus LSA-SAF evapotranspiration (*Psat – ETsat*) and aggregated to monthly scale (mm month^{-1}). Processing the PR and preparation of these maps is done in MATLAB. High PR are shown in the central west and central east maps, where *Psat* is high.

Table 7: Spatiotemporal monthly total maximum, minimum, mean, and standard deviation (SD) of the satellite-based potential recharge (PR) in the dehesa (montado) water limited hard rock DMHR area. These are extracted from the monthly total (mm month^{-1}) maps that are aggregated from the daily (mm day^{-1}) maps of the PR. The PR is calculated by subtracting the daily (mm day^{-1}) LSA-SAF based evapotranspiration product (*ETsat*) from the daily CHIPS rainfall (*Psat*) in GIS and MATLAB. The max and min means the highest and the lowest monthly total PR values respectively in any part of the DMHR area. The mean is the average monthly flux (mm month^{-1}) of the PR the DMHR area for the given month and year

	Year 2011 (mm month^{-1})				Year 2012 (mm month^{-1})				Year 2013 (mm month^{-1})				Year 2014 (mm month^{-1})				Year 2015 (mm month^{-1})				Year 2016 (mm month^{-1})			
Month	Max	Min	Ave.	SD	Max	Min	Ave.	SD	Max	Min	Ave.	SD	Max	Min	Ave.	SD	Max	Min	Ave.	SD	Max	Min	Ave.	SD
Jan	214	2.8	44.2	24	77.6	-16	5.2	10.8	311	3.4	53.2	33.1	266	9.6	70.1	35.2	165	-6.5	25.5	19.5	417	4.1	68.1	55.8
Feb	223	-8.6	44.7	25.5	76.2	-35	-9.6	13.2	159	-11	15.3	16.9	342	-7.9	69.3	38.2	138	-28	1.4	21.7	373	-5.8	49.2	41.1
Mar	177	-10	39.2	26.2	65.2	50.8	-3.1	19.4	402	40	137.4	52.4	95	-40	-2.5	20	95	-54	-11.8	21.4	108	-53	-7.5	21.8
Apr	144	-34	40.8	25.4	258	-26	33.8	40.8	245	-3.8	50.3	31	105	-50	9	24.7	155	-40	14	22.4	207	-33	36.5	29.1
May	151	-69	11.3	28.3	60.3	-87	-15.9	21.7	123	-13	18	17.6	66	-84	-21.6	21.4	50	-90	-17.6	21.2	165	-42	45.1	34.8
June	25.7	-103	-16.9	19.1	27.8	-110	-12.8	17.5	42	-20	2.8	8.1	34	-88	-13.7	19.3	72	-92	-8.2	19.5	19.8	-105	-22.3	19.6
Jul	20.4	-104	-12.8	15.2	6.7	-104	-15.5	14	38	-27	-3.3	9	40	-97	-12.8	17.1	27	120	-10.7	16.3	26.3	-99	-9.8	16.3
Aug	52	-70	1	12.4	19.7	-74	-7.8	10.3	33	-27	-3.8	8	35	-82	-8.2	11.9	53	-71	-3.3	12.3	16.5	-75	-6.5	11.1
Sep	38	-32	9.2	8.4	135	-19	47.1	22.7	79	-8.3	20.2	12.5	115	-74	35.1	18.5	69	-32	11.1	11				
Oct	90.6	-18	23.9	15.8	182	1.6	68.4	30.3	183	10	83.1	30.1	113	-3.7	42.4	20.6	160	3.6	69.9	29.2				
Nov	223	18.7	87.7	34.6	225	11.2	102	34.4	61	-12	7	9	241	27	109.5	34.8	91	0.2	27.3	12				
Dec	117	-16	8.6	15.6	204	-3.6	40.7	25.7	242	5.3	51.8	29.2	116	-14	13.7	15.1	137	0	28.9	15.5				
Annual mean (mm yr^{-1})			241.4	0	114.4	8.3	279.5	0	121.7	50.6	416	0	168.5	70.3	353	0	127.9	60.7	189	0	99.5	41.3	427	0

Table 8: Summary of dry (June to Sept) and wet season PR in DMHR. The wet season contribution is shown sometimes to be above 100 %, indicating compensations of the deficit (negative recharge) in the dry season.

PR	Year					
	2011	2012	2013	2014	2015	2016
Total PR (mm yr^{-1})	280.9	232.5	439.1	349.1	178.1	198.9
Dry season (mm)	-19.5	11.0	15.9	0.4	-11.1	-38.6
Dry season (%)	-6.0	5.0	3.8	0.1	-8.0	-2.0
Wet season (mm)	300.4	221.5	416.1	289.9	137.6	191.4
Wet season (%)	103	95.3	96.3	99.9	108.8	125.3
SC PR (mm yr^{-1})	304.8	188.2	183.3	317.6	74.9	98.5

Generally, the dry season (June to Sept) potential recharge (PR) to the total annual ranges from the highest of 15.9 % in 2013 to the lowest of -38.6 % in 2016 (see Table 8). It has been mentioned that the dry season PR is negative. The dry season PR would be expected to be higher in the year 2015, which was the year with highest dry season *Psat* accumulation. However, the *ET* influences it and non-linearizes the coefficient of *P* in expressing the recharge.

4.5. Sardon transient model updated by using spatiotemporally variant driving forces

The model simulation with spatiotemporally variable driving forces for the time period of October 2011 to September 2013 showed difference in the water budget components as compared to the transient model with spatiotemporally invariant driving forces. The plot of the observed and simulated heads in the abscissa and ordinate (Fig. 32) show good consistency with $R^2 = 0.99$, and RMSE = 1.43m. The R^2 meets the criteria set by Hill (1998), which is also cited by Weldemichael (2016) that says it should be > 0.9. The mean error (ME), mean absolute error (MAE) are o.69 m and 1.12 m respectively. The normalized RMSE, which is expressed as a ratio the RMSE to the average of the observed heads is 0.02%. This means the model calibration error accounts for 0.02 % of the overall errors.

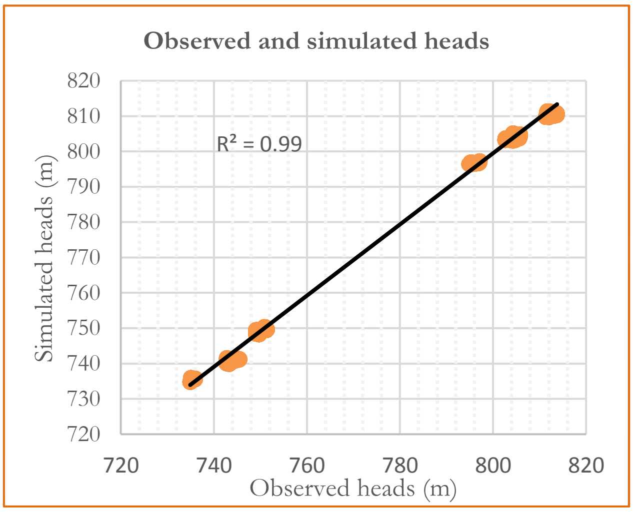

Figure 30: Scatter plot of observed and simulated heads for the transient model of SC using spatiotemporally variable driving inputs for 8 observation points. The simulation period is from Oct 2011 to Sept 2013.

The observed and simulated head hydrographs show a similar pattern of fluctuation (see Fig. 33) in most of the groundwater (GW) level monitoring points. This tells that the model simulation has acceptable accuracy. Nonetheless, there are irregularities (inconsistency of the observed and simulated hydrographs) of patterns which show uncertainties in the model result. These inconsistencies are caused by inaccuracies of estimating model parameters, zoning, difficulties of estimating factors related to intricate interactions of the inherent properties (like fracture network density, geometry, connectivity, and infill) in fractured rocks (Mortimer et al., 2011). The water level in the simulated heads is underestimated throughout the simulation period in the most of the piezometers, while in the boreholes it underestimated at the start of the simulation period and overestimated at the end of the simulation period. Hassan et al. (2014) explain that the mismatch is due to unaccounted heterogeneity in the aquifer characteristics, the uncertainty of water level records, unaccounted water extraction, grid size and sub-grid-scale altitude variability. This means poor estimation of model boundary conditions, uncertainties from model parameterization including inaccuracies in the assignment of vertical and horizontal hydraulic conductivities and/or specific yield and specific storage.

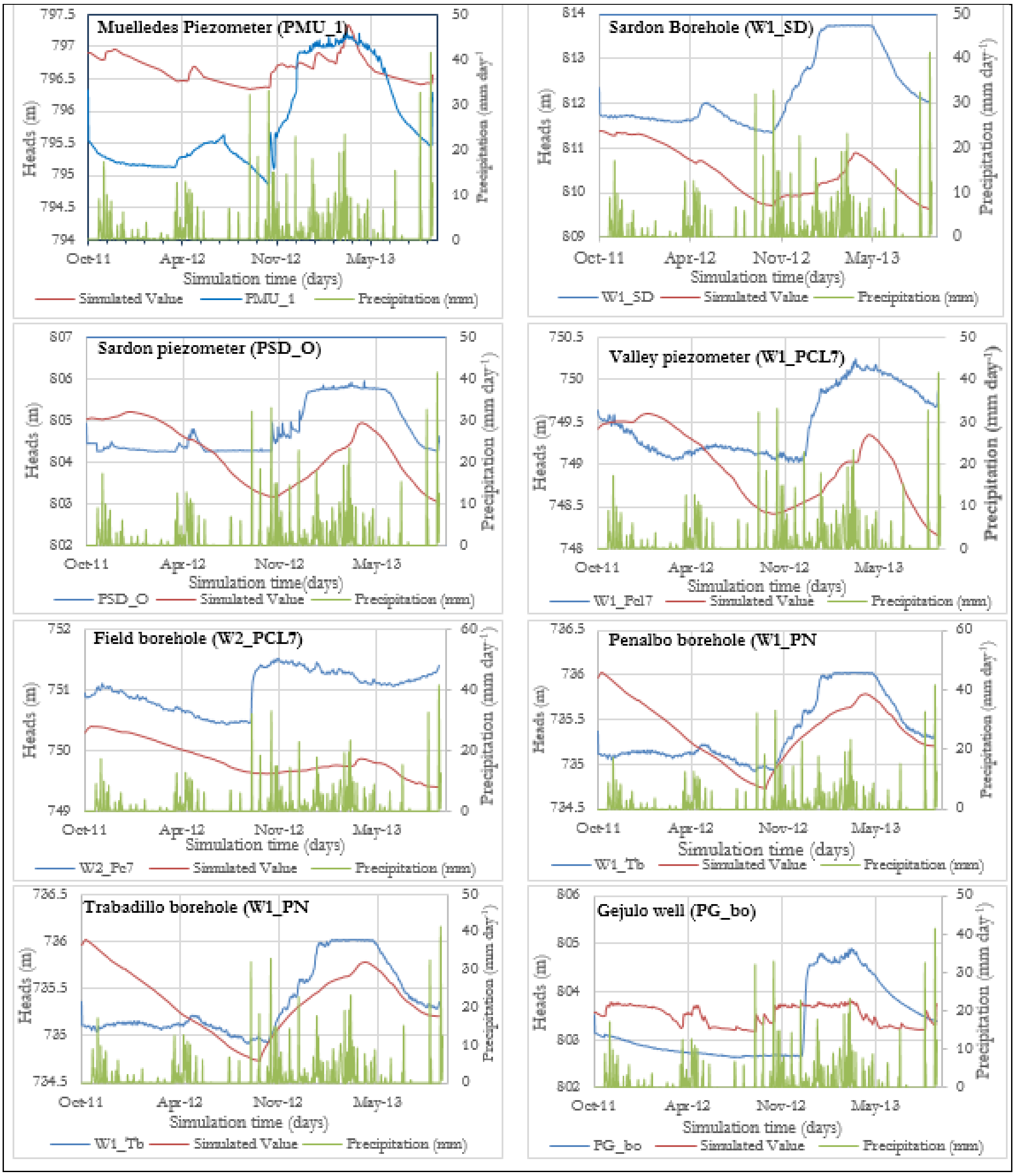

Figure 31: 3-year (Oct. 01, 2011 to Sept. 30, 2013) transient model simulation of SC with spatiotemporally variant driving force model inputs consisting of 4 boreholes, 3 piezometers, and 1 well used for post auditing of accuracy after model simulation. The transient model has been simulated by Weldemichael (2016) using spatiotemporally invariant driving forces of *P* and *PET*. In this study, the model is simulated using spatiotemporally variable infiltration rate, *PET*, EXTDP.

The sum of the water budget components coming into and going out of the GW system should be zero because of the law of conservation of mass. In this model simulation, the water balance is 0, and it has met the criteria. Table 9 shows the GW budget for the model simulation with spatiotemporal driving forces (model simulation in this research) and spatiotemporally invariant forces (outputs from Weldemichael, 2016) model from the year 2011 to 2014. This is done by subtracting water budget components at the time step 1463 from time step 2193 in the transient model calibrated by Weldemichael (2016). Particularly *ETg*, (ΔS), and more interestingly the *Rn* that is the flux required for scaling up in this study have shown a significant change from the model simulation with spatiotemporally invariant driving forces (Table 9). A similar table in the existing model for the year 2014 has been shown in Table 2, Section 3.6. The *ETg* increased by 328.5 %, and the *Rn* decreased by 130.4%. The *Rg* and Exf_{gw} have shown less variation.

Table 9: Groundwater budget for spatiotemporally variable and spatially invariant driving forces of model simulation from Oct 2011 to Sept 2013.

Budget component	Model solution with:			
	Spatiotemporally variable driving forces		Spatiotemporally invariant driving forces	
	IN	OUT	IN	OUT
Change in storage (ΔS)	1.12	0.64	0.48	0.47
Head dep bounds	0.00	0.02	0.00	0.02
Net recharge (*Rn*)	-0.07	0.00	0.23	0.00
Gross recharge (*Rg*)	0.85	0.00	0.61	0.00
GW exfiltration (Exf_{gw})	0.00	0.12	0.00	0.11
GW evapotranspiration (*ETg*)	0.00	0.92	0.00	0.28
Stream leakage (q_{sg})	0.12	0.40	0.07	0.29
Total IN-OUT	2.09	2.09	1.16	1.16
In-OUT	0.00	0.00	0.00	0.00
% Error	0.00	0.00	0.00	0.00

The daily fluxes derived from this spatiotemporally variable model simulation are used for upscaling recharge (with a focus on the *Rn*) from this model to the DMHR by testing their correlation with the *Psat*, and *ETsat,* and the PR (*Psat - ETsat*). The plot of the *Rn* with *Psat* and *ETsat* fluxes of Trabadillo Automatic Data Acquisition System (ADAS) in Sardon Catchment is shown in Fig. 33.

4.6. Recharge scaling-up function (RUF) between Sardon Catchment's *Rn* & satellite-based fluxes

4.6.1. Defining RUF

The significance of correlations between the flux outputs (*Rg* and *Rn*) of Sardon Catchment model with respect to the satellite-based variables (*Psat*, *ETsat*, and PR) at different temporal scales show variations. The residuals of the curve fittings also differed with variation in temporal scales. Nonetheless, the correlation is affected by the uncertainties of the *Psat* and *ETsat* estimations. The significance of the correlation between the variables is explained by R^2. The R^2 shows how much of the variations in the response (dependent) variable is explained by the variations in the independent variables (Shevlyakov and Oja, 2016). The response and independent variables in the present research are *Rg* or *Rn* and *Psat*, *ETsat*, or PR respectively.

The plots of net recharge (*Rn*) of SC with the *Psat* and *ETsat* from 2011 to 2014 (Fig. 33) show that the net recharge is mostly higher during higher *P* occurrences and decreases in lower *P*. In some parts of the graph (marked by red dotted circles), the pattern of rising and falling of the *Rn* and *Psat* (*ETsat* as well) show differences. This can be due to uncertainties (like explained for PR in Section 4.1.1) in model calibration or parametrization, and uncertainties in remote sensing *Psat* and *ETsat* estimates. This can have an effect on the accuracy of the scaled up recharge over the DMHR. In general, however, the recharge of the model has shown good consistencies with the *Psat* and *ETsat*. Therefore, extrapolation of *Rn* using the relationship of these variables can give acceptable results. The details on how the representative *Psat* and *ETsat* for Trabadillo station in Sardon Catchment are derived has been explained in sections 3.4 and 3.5.

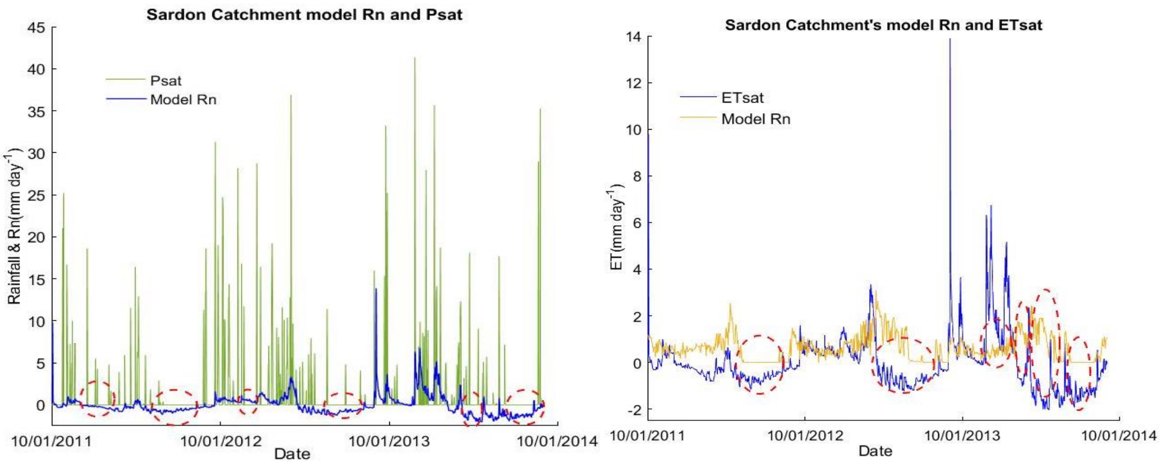

Figure 32: Model-based *Rn* for SC (Trabadillo ADAS station) and satellite-based fluxes for the pixels corresponding the station (a) *Rn* & *Psat*, and (b) *Rn* & *ETsat*.

Curve fitting Rg with Psat, ETsat, and PR on a daily scale

On a daily scale, the R^2 of the correlation between the *Rg* and the satellite-based variables; *Psat*, *ETsat*, & PR is found to be 0.87, 0.89, and 0.88 respectively (see Fig. 34a, b & c for the distribution of the plots of *Rg* and satellite-based variables). This means, by fitting the curve shown in Fig. 34, 87%, 89%, and 88% of the variations in *Rg* are explained by the variations in *Psat*, *ETsat*, and PR respectively.

Considering the R^2 alone, the correlation of *Rg* with *Psat*, *ETsat*, and PR is strong. However, the distribution of the residuals of the curve fitting, i.e., the deviation of the variables below and above the fitted curve, gives more information on the significance of the correlation than does the (Webster and Oliver, 2008). Looking at Fig. 34a, b & c (bottom), the residuals are not equally distributed below and above the fitted curve. Therefore, the correlation of *Rg* with respect to *Psat*, *ETsat*, and PR at a daily temporal scale is not as strong as its R^2 indicates.

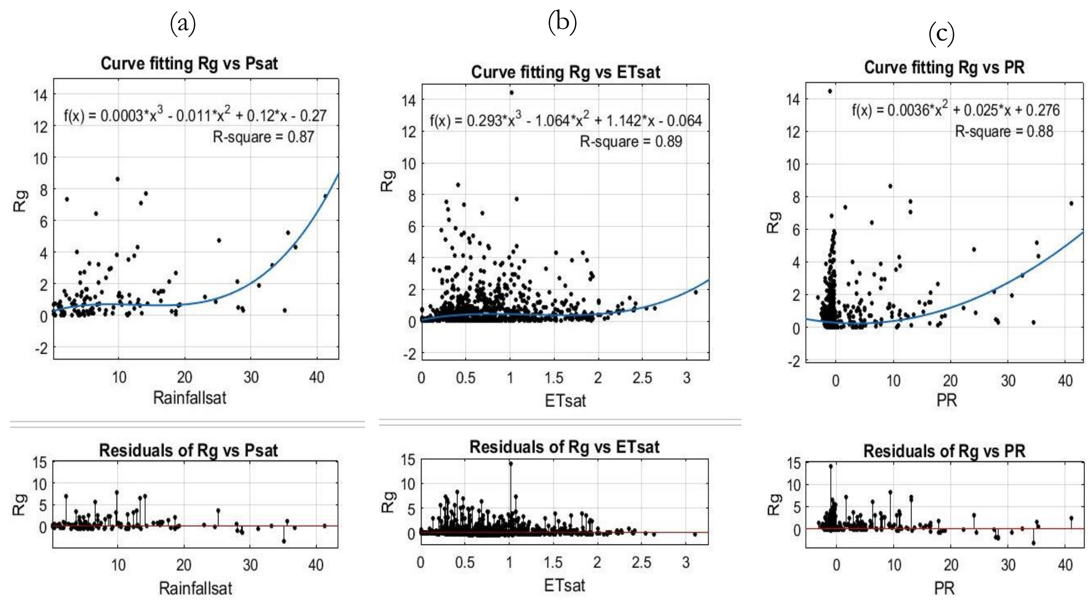

Figure 33: Regression curves of: *Rg* with satellite-based daily: (a) *Psat*, (b) *ETsat*, & (c) potential recharge (PR). All units are in mm day^{-1}.

Curve fitting Rn with Psat, ETsat, and PR on a daily scale

The R^2 of the correlation (daily scale) between the *Rn* and the satellite-based variables; *Psat*, *ETsat*, & PR is found to be 0.51, 0.65, 0.5 respectively (see top Fig. 35a, b & c). The complex unsaturated hydraulic conductivity that non-linearizes the infiltration process may decrease the correlation between the *Rn* and the *P* (S. and Liu, 2000). Regardless of this, the distribution of residuals is more uniform (symmetric) than in the curve between *Rn* with *Psat* than *Rn* with *ETsat* and PR (see bottom Fig. 35a, b & c). In hydrological analyses $R^2 < 0.5$ is considered as weak, between 0.5 and 0.7 is considered as moderate, and >0.7 as strong correlation (e.g., Trang et al., 2017). However, in some studies, temporal analysis of *P* have been done based on moderate correlation (e.g., García-Barrón et al., 2015), and considered $R^2 > 0.6$ as strong correlation.

Another statistical parameter that is used to judge the significance of the correlation between two variables is Pearson coefficient of correlation. A value of Pearson's correlation >0.5 has been considered as strong by Fernández-Montes et al. (2015), and values as low 0.2 have been considered as significant. In this study, the Pearson's correlation between *Rn* and *Psat* is 0.3. Moreover, *Rn* gives more helpful in the management of GW resources (Lubczynski and Gurwin, 2005). The R^2 as a result of the curve fitting of *Rn* and *Psat* 0.51, though, the multivariate curve fitting of *Rn* with *Psat* & *ETsat* gives larger value. For this, the function of single variable regression using *Psat* is not adopted for scaling up on a daily basis. The following function defines the regression of *Psat* against *Rn*. The function for scaling up *Rn* on a daily basis is shown in Equation 17.

f(x) = 0.0003*x^3 - 0.014*x^2 + 0.19*x - 0.35 ………………………………………………………………….. (17)

where, f(x) is the net daily recharge *Rn* scaled up over each point in the DMHR, and x is the daily satellite rainfall (*Psat*) measurement for each pixel in the spatiotemporal *Psat* map of the DMHR.

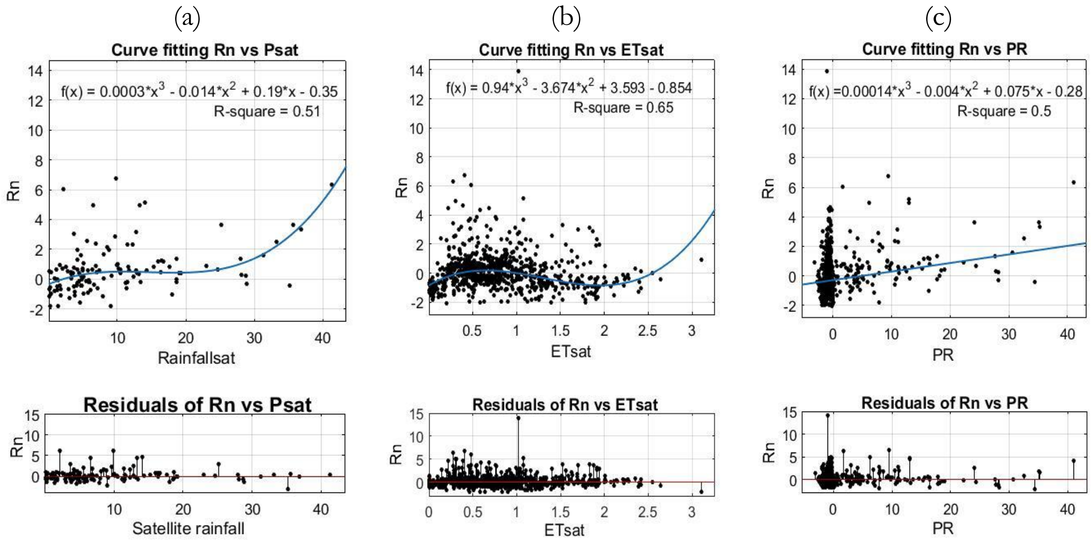

Figure 34: Regression curves of: *Rn* with satellite-based daily: (a) *Psat*, (b) *ETsat*, & (c) potential recharge (PR). All units are in mm day^{-1}.

A significant increment of *Rg* and *Rn* is observed when the daily *Psat* > ~26 mm (see Fig. 34a & 35a). This means when the *Psat* amount is less than ~26 mm, the relative increment of *Rg* and *Rn* for each additional unit of *P* is low in the study area. This is because the first amounts of *P* are used to saturate the soil. Then once the moisture demand of the soil is satisfied there is a significant rise of *Rg* and *Rn*. This is because the first few mm of *P* is utilized to saturate the soil. Then once the soil is saturated, the recharge shows a quick rise. Similarly, a significant increment of *Rg* and *Rn* is observed when the daily *ETsat* > 2.5 mm (shown in Fig. 34b & 35b). This can be explained in two ways; (i) *ET* is higher when *P* is higher; (ii) the relative influence of *ET* on *Rg* or *Rn* is lower than *P*. In other words, the magnitude of increment of *ET* is lower than *P* and so is its direct influence on *Rg* and *Rn* is lower.

Curve fitting Rg with Psat, ETsat, and PR on a 10 daily scale

The correlation test based on 10 daily total of the *Psat*, *ETsat*, and PR fluxes (the figures not presented here) has not shown improvement both in R^2 and the residuals distribution. So this is not considered as an option for upscaling.

Curve fitting Rg with Psat, ETsat, and PR on monthly scale

The R^2 of the monthly total based *Rg* regressed by *ETsat* and PR has decreased from 0.89 and 0.88 to 0.7 and 0.74 respectively, whereas the R^2 regressed by *Psat* has increased from 0.87 to 0.88. Contrarily, the distribution of the plots of the variables (*Rg* and satellite-based variables) and the residuals is not improved as compared to similar regression on a daily scale (refer Fig. 36a, b & c). Therefore, the monthly based correlation of *Rg* and satellite-based variables has generally not shown better significance than in the daily based.

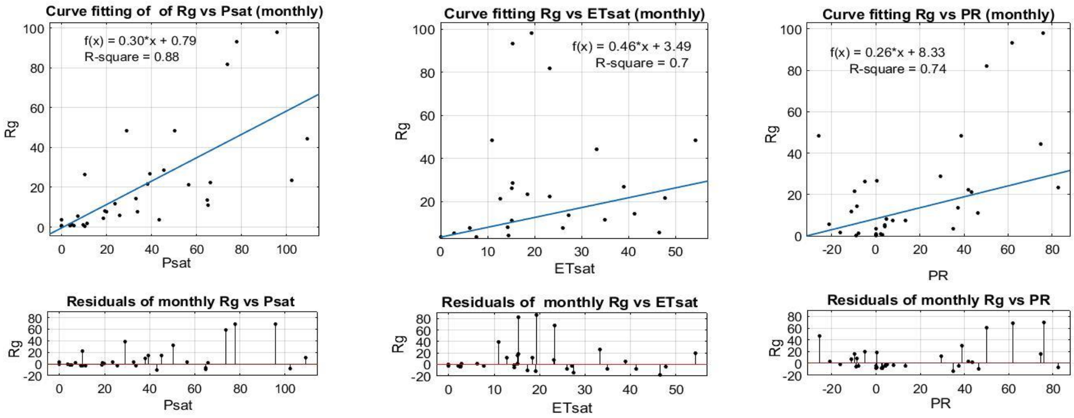

Figure 35: Regression curves of *Rg* with satellite-based monthly *Psat* (left), *ETsat* (centre), & PR (right). All units are in mm month^{-1}.

Curve fitting Rn with Psat, ETsat, and PR on monthly scale

The R^2 of the monthly total based *Rn* regressed by *Psat* and has increased from 0.51 in daily scale to 0.54, whereas the R^2 regressed by PR has decreased from 0.5 on the daily to 0.48 in the monthly scale. The R^2 regressed by *ETsat* has also decreased from 0.65 to 0.21. The diminishing of the R^2 and the wide spreading of the plots of the *Rn* against *ETsat* can be due to the complex interactions of *ETg* and exfiltration. In addition, the R^2 in the similar regression of *Rn* by PR has decreased from 0.5 to 0.48. However, the function is defined by the linear relationship as compared to the daily based (which is polynomial). This means the monthly based correlation of *Rn* with *Psat* and *Rn* with *ETsat* is preferred to the daily based, even if the R^2 has decreased a little bit. Moreover, the distribution of the plots of the variables (*Rn* and satellite-based variables) and the residuals has improved (unlike with the monthly based *Rg* and *Psat*) as compared to similar regression on a daily scale (see Fig. 36c and 37c). This is, however, when a single correlation is done (not comparing with the multivariable correlation). In the study in Sardon Catchment, Hassan et al. (2014) found R^2 of 0.73 between annual *Rn* and *Psat*. Therefore, the R^2 between *Rn* and *Psat* in the present study at a monthly scale is realistic. The function that can be used for scaling up *Rn* on a monthly basis is given in equation 18.

f(x) = 0.68*x - 27.18……………………………………………………………………………………... (18)

where, f(x) is the net monthly *Rn* scaled up at each point (pixel) in the DMHR, and x is the monthly total *Psat* measurement at each pixel in the spatiotemporal *Psat* map of DMHR.

The linearity of the relationship between *Rn* and *Psat* has increased in the monthly scale as compared to the daily scale. This is due to the time required (time lag) for the *P* to reach the ground water (Moon et al., 2004; Chen et al., 2012). Additionally, the study by Hassan et al. (2014) that shows even better correlation on annual basis goes in line with this explanation. A similar finding by Whittecar et al. (2016) indicates that water table fluctuation patterns as a result of recharge replicate reasonably at monthly scales. Apart from this, *P* intensity described by negative linear relationship with recharge (Wang et al., 2015) is not considered in this study. Therefore, the function derived from the correlation of *Rn* and *Psat* monthly temporal scales can be used to define the respective RUF and upscale the *Rn* of Sardon Catchment's model into daily and monthly *Rn* over the DMHR (not done in this study). The test based on cumulative, however, has not resulted in significant correlation.

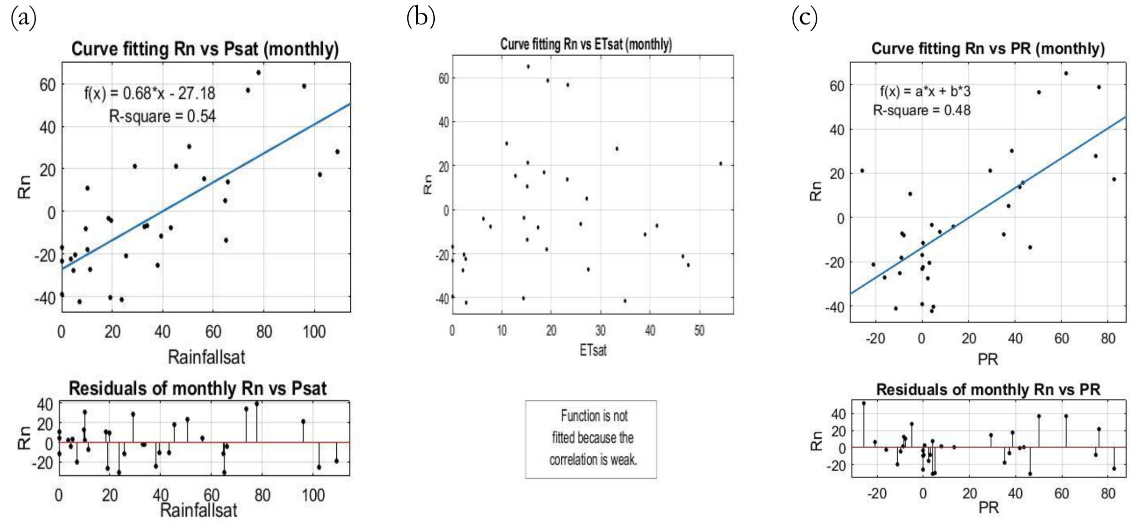

Figure 36: Regression curves of *Rn* with monthly: (a) *Psat* (b) *ETsat* and (c) PR. All units are in mm month^{-1}.

Curve fitting Rg with Psat, ETsat, and PR based on season

The R^2 of the curve fitting (between the daily *Rg* and *Rn* with *Psat*, *ETsat*, and PR) in the dry is found to be low, and so it is not presented here. Only the curve fittings for the wet season (September to May) are presented (see Fig. 38 left & right). Even though the R^2 of the correlation between *Rg* and *Rn* with *Psat*, *ETsat*, and PR in the wet season indicates high values, the residuals are not uniformly distributed. In addition, the curves are more or less horizontal, meaning that the *Rg* and the *Rn* do not vary with variation in *Psat*, *ETsat* or PR. Therefore, the function separately derived from dry and wet season classification is not also used for upscaling.

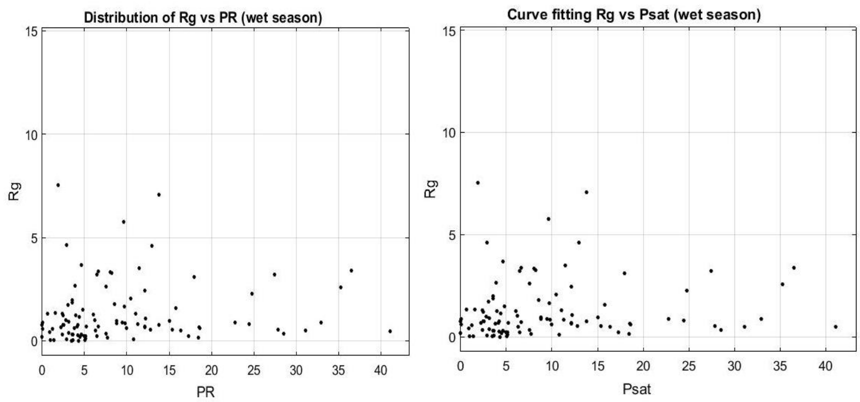

Figure 37: Regression curves of *Rg* with satellite-based wet season daily *Psat*, *ETsat*, and PR. All units are in mm season^{-1}.

Multi-regression of Rn with Psat and ETsat on daily scale

The R^2 of the multivariate function for the daily *Psat* and *ETsat* is 0.63, which is larger than for the single linear regression (0.51) with respect to *Psat* and *ETsat* (see Fig. 39). The patterns of rising observed in the single linear regressions of *Rn* with *Psat* and *ETsat* are maintained. This means the sharp rise of the *Rn* that is observed in the single linear regressions at *Psat* is > ~26 mm and *ETsat* > ~2.5 mm is also observed in the multivariate fitting with *Psat* and *ETsat*. In other words, the multi regression has both increased the R^2 and maintained the individual characteristics of the relationship curves of *Rn* with *Psat* and *ETsat*. Therefore, on a daily basis, the function defined by the multi-regression of *Rn* by *Psat* and *ETsat* is adopted for scaling up net recharge (*Rn*) from Sardon Catchment's model into the DMHR. The following function derived from the multivariate fitting is used for upscaling (Equation 19).

f(x,y) = -0.8486 + 3.281*x + 0.1435*y - 3.294*x^2 - 0.0437*x*y - 0.0107*y^2 + 0.8201*x^3 + 0.02434*x^2*y - 0.000067*x*y^2 + 0.0002684*y^3 ………………………………………………………….... (19)

where, f(x,y) is the net daily *Rn* scaled up over each point in the DMHR, and x and y are the daily *Psat* and *ETsat* measurements respectively at each pixel in the spatiotemporal *Psat* map of DMHR.

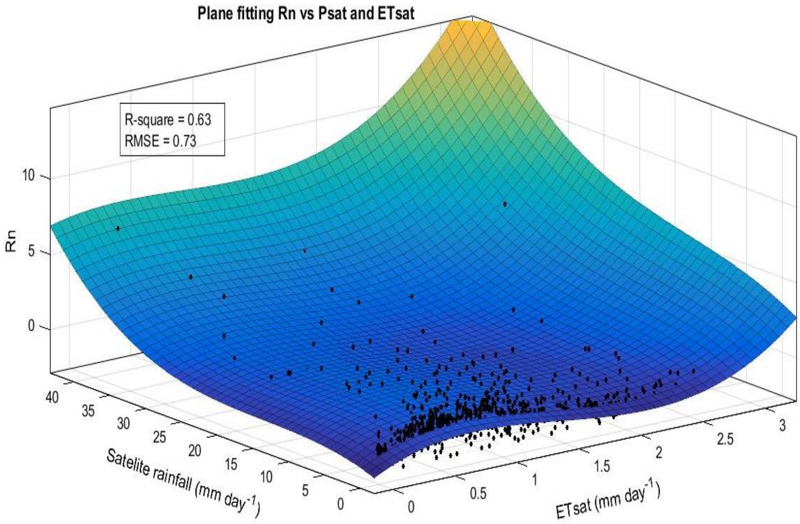

Figure 38: Multivariate regression of daily *Psat* and *ETsat* against *Rn* of Trabadillo ADAS in SC. All units are in mm day^{-1}.

The option to scale up the effective recharge (Re)

A strong linear relationship is not observed between *Psat* with *Rg* and *ETsat* with *ETg*. Therefore scaling up *Re* is not considered for it may introduce high uncertainties in the scaled values.

Final decision on scaling up

The correlation tests show that the multivariable regression on a daily scale and the linear function on a monthly scale are acceptable. The other correlations (including based log-transformation of the variables) have not given significant relationship of *Rn* and the satellite-based fluxes. The linear function defined by regressing *Psat* against *Rn* on a monthly sum basis is an acceptable option, though, it is not included in this study. At the end, it is decided to scale up net recharge (*Rn*) from SC to the DMHR by applying the regressed multivariable function of the *Psat* and *ETsat* on a daily basis (see Fig. 39 and Equation 19).

4.6.2. Comparison of net recharge (*Rn*) from the model and from regression function

The plots of the model net recharge (*Rn*) and satellite *Rn* derived by the function of the curve fitting at daily and monthly scales show more or less similar pattern (see Fig.40 & 41). However, there are still inconsistencies of the pattern (oscillation) between the *Rn* from the model output and the *Rn* derived from the regression function. Nonetheless, the plots on a daily and monthly scale have some inconsistencies. The parts marked by red dotted ellipses show these inconsistencies. The inconsistencies are observed mostly at periods of low and high extremes of the *Rn*. However, the pattern is similar and it is acceptable to use this for scaling up. The black dotted ellipses in Fig. 40 show inconsistencies in the multivariate fitting (*Rn* scaled up with *Psat* and *ETsat*). It can be seen that the *Rn* derived from the *Psat* alone has more inconsistencies of estimate to the *Rn* from the model than the *Rn* derived from combined *Psat* & *ETsat* (multivariate function). Therefore, the multivariate has resulted in both a bit higher R^2 and a better similarity of consistency of *Rn* estimate (see Fig. 40) than the *Rn* from *Psat* alone (univariate function).

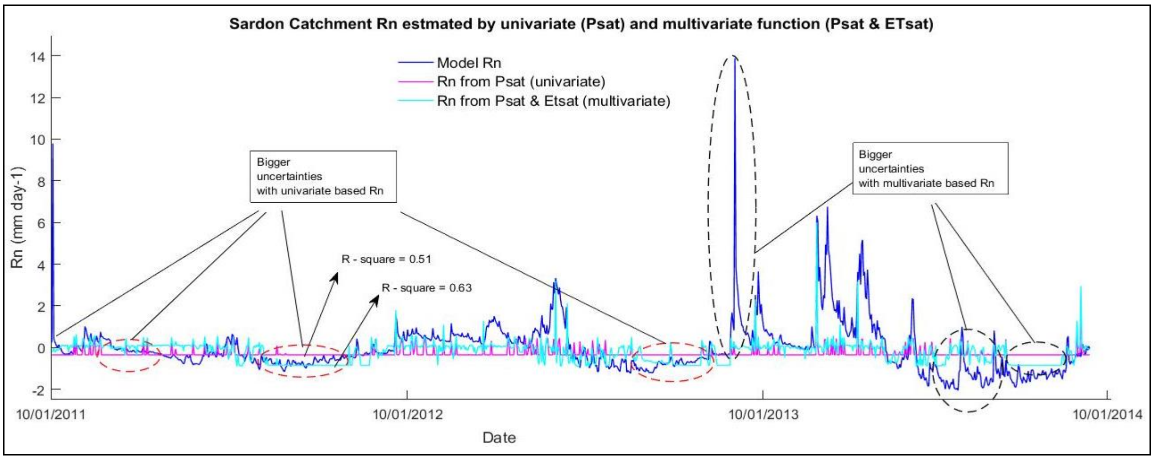

Figure 39: *Rn* derived from (1) Univariate function of daily *Psat* against model *Rn* is shown in magenta and (2) Multivariate function of *Psat* and *ETsat* against model *Rn* shown in cyan.

Apart from the above, the plots of the *Rn* from the model and the *Rn* derived by the function between *Psat* and *Rn* at a monthly scale shows more consistency of estimate. Moreover, this relationship is based on a linear fitting. Therefore, this function can give a good estimation of *Rn* scaled up over the DMHR. Therefore the *Rn* scaled up into the DMHR will follow a similar pattern to Fig. 40 in a daily scale, and Fig. 41 in a monthly scale at each point taken in the area. However, wherever there are extreme *Psat* events that have not occurred in Sardon Catchment ADAS in the study period, the pattern may be different.

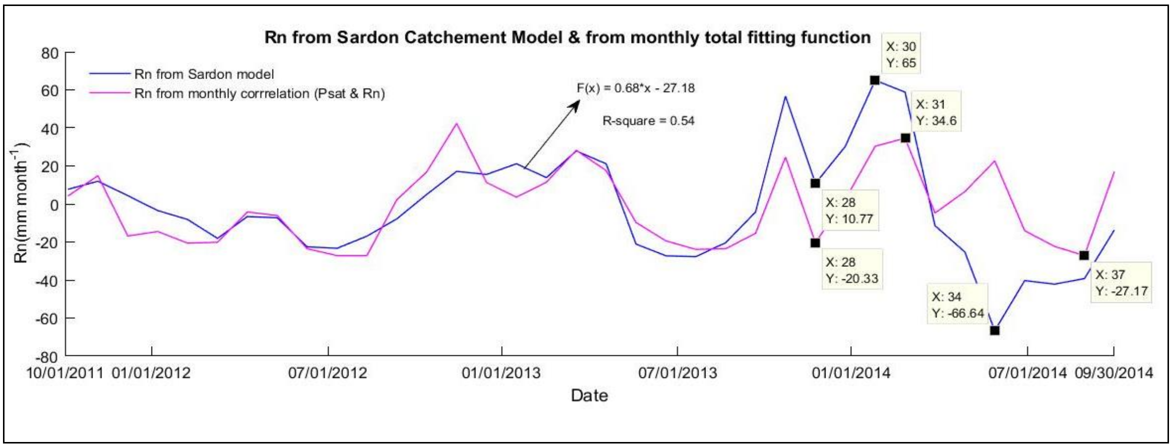

Figure 40: *Rn* of the SC model output shown in blue and *Rn* derived by the function applying the correlation of monthly *Psat* (for SC ADAS station) with SC model *Rn* that is shown in magenta.

In general, the present study the function has uncertainties particularly at low and high extremes of *Rn* from the model. Thus it shows both overestimation and underestimation (see Fig. 40 & 41). The overestimation is related to higher *P* intensity, which in actual ground conditions the recharge (*Rn* from the model) is lower than anticipated. It can be related also to uncertainties in model calibration and uncertainties in fitting the function. Nevertheless, the correlation between the recharge input fluxes (*P* and *ET*) and the model output fluxes (*Rg* and *Rn*) is not as strong as the findings by Gemitzi et al. (2017); Macdonald & Edmunds (2014); and Rossman et al. (2014) who have found a linear relationship of $R^2 > 0.7$ with recharge against rainfall and *ET* at a monthly scale. However, the groundwater evapotranspiration (*ETg*) that has the tendency to affect the linear relationship between recharge and *P* or *ET* is not considered by these studies. Furthermore, the intricate hydrogeological nature of hard rocks in the DM areas can decrease the linear correlation in addition to the uncertainties in the input fluxes estimation and model error. The difference in environmental has also an effect on the correlation. Therefore, scaling up applying the multivariable function of *Rn* with *Psat* & *ETsat* on a daily scale and the univariate function of *Psat* on a monthly scale are acceptable.

4.7. Scaled up Net Recharge (*Rn*) over the DMHR area

The spatiotemporal monthly total net recharge (*Rn*) in the hydrological year of 2011 (Oct 2011 to Sept 2012) ranges from a maximum of 115.2 mm that occurred in Oct to a minimum of - 26.3 mm in July & Aug. This is excluding 4% of the pixels for the study area showing extremes of calculated *Rn* values in limited localities in that year (explanation at the end of this section). The spatial monthly mean of this hydrological year ranges from 14.6 mm in May to - 10 mm in Aug, with a spatiotemporal annual mean (average for the 12 months in the whole study area) of -0.3 mm. This means that there is an average annual recharge deficit of 0.3 mm. This goes in line with the study by Hassan et al. (2014) that indicated negative annual recharge in SC in the years 1999, 2005 and 2012. The standard deviation ranges from 48.3 in May to 2.1 in Jan (see Fig. 42 and Table 11 for details).

The spatiotemporal monthly total *Rn* in the hydrological year of 2012 (Oct 2012 to Sept 2013) ranges from a maximum of 248.4 mm that occurred in May to a minimum of -26.3 mm in July & Aug. Similarly, for the hydrological year 2013 (Oct 2013 to Sept 2014) it ranges from 321.6 mm in Apr to -26.3 mm in July and Aug. This is excluding 3.4 % and 3.6 % of the pixels for the study area showing extremes of calculated values (outliers) in the year 2012 and 2013 respectively. The spatial monthly mean *Rn* of the hydrological year 2012 ranges from 13.9 mm in Jan to -8.7 mm in Aug, with a spatiotemporal annual mean (average of the 12 months in the whole study area) of 2.9 mm. Likewise, the monthly mean for the year 2013 ranges 18.6 mm in Oct to -9.2 mm in Aug, with a spatiotemporal annual mean of 1.4 mm. This means, in the study area, there is an average net positive annual *Rn* of 2.9 mm and 1.4 mm in the hydrological years of 2012 and 2013 respectively. The standard deviation these years ranges from 43.3 in June to 8.6 in Sept and 52.7 in Feb to 2.5 in Nov respectively (Fig. 42 and Table 11).

When *Psat* is above ~40 mm day-1 which have been observed in some areas, the *Rn* scaled up using the multivariate function resulted in exaggerated values in the orders of hundreds. As described in a study by Hassan et al. (2014) the ratio of *ET* to *P* (*ET*/*P*) decreases with extremes of *P*, which actually doesn't go beyond an annual total of ~470 mm even if the *Psat* increases to 1000 mm. So, in a similar way, the polynomial function used for upscaling *Rn* in this study has exaggerated the *Rn* when *Psat* > ~40 mm day-1. However, the extreme *Psat* days occur in very few days of the year and limited localities (pixels). For example, Hassan et al. (2014) have indicated that only 26 extreme *P* events, exceeding 30 mm day-1, occurred in 18 years. The number of pixels with such outliers are also very few (few tens) as compared to the total pixels of 5842 covering the whole study area (see Table 10). Therefore, the result is acceptable.

Extreme scaled *Rn* values are not observed in months Sept to Dec and Aug. The reason is that extreme *Psat* events have not occurred in these months in the current study period. Particularly in August, *P* almost doesn't occur completely. Therefore, a few exaggerated *Rn* pixels can be found due to the concentration of extreme but few *Psat* event days in few localities (pixels), accompanied by very small values of *ETsat* that can't optimize the exponential increment of *Psat* in deriving the RUF to calculate *Rn*. For example, a pixel with *Psat* event as high as 156 mm day^{-1} is found on Feb 22, 2013, & the corresponding *ETsat* is 1.12 mm day^{-1}. Due to this, the max *Rn* depicted from the map in this month is 811.3 mm. Such values are excluded as outliers (Table 10).

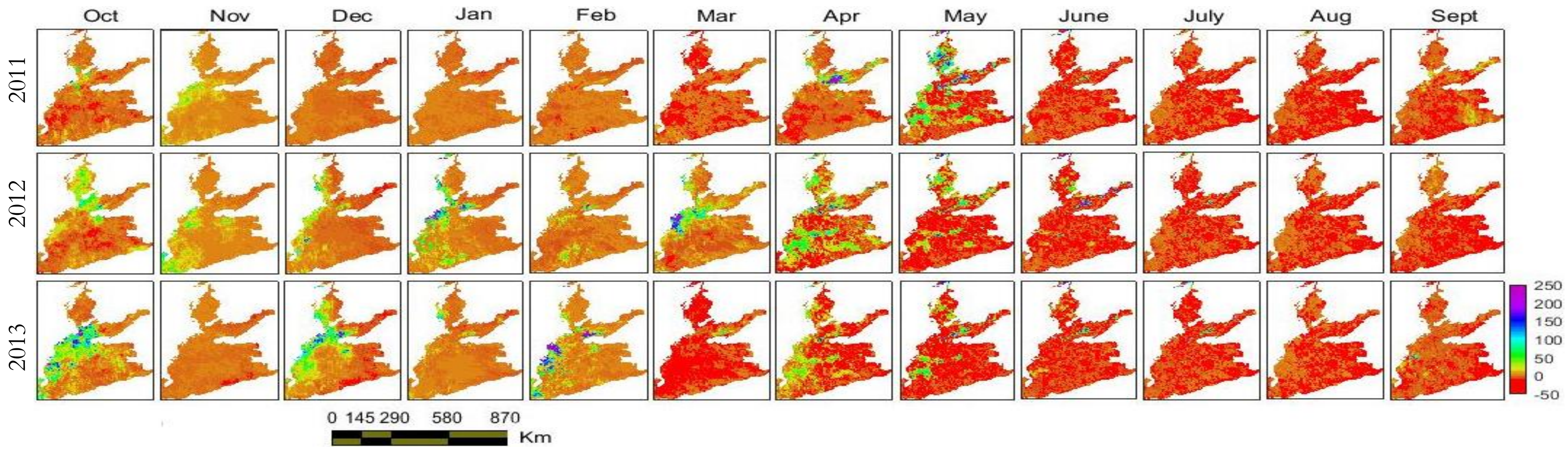

Figure 41: Net recharge (*Rn*) map of dehesa (montado) for the hydrological years 2011to 2013 (Oct 2011 to Sept 2014. This is derived by scaling up the *Rn* of the Sardon Catchment's using the multivariate function defined by regressing with *Psat* and *ETsat*. The maps are first prepared on a daily scale and then are summarized on the monthly total. The numbers labelled on the left of the map are hydrological years. The *Rn* is mostly negative, particularly in the dry seasons (June to Sept).

Table 10: Number of extreme values in the scaled up pixels of the *Rn* map of DMHR. These pixels are extracted from the final scaled up *Rn* map of the DMHR by conditional statements in MATLAB putting a threshold of the PR.

Hydrology Year	Number of days in:											
	Oct	Nov	Dec	Jan	Feb	Mar	Apr	May	June	July	Aug	Sept
2011	3	0	0	0	0	0	41	622	86	98	10	0
2012	0	0	1	25	8	14	8	42	234	58	5	0
2013	48	0	18	0	27	1	8	152	139	75	0	8
2014	3	0	0		0	0	41	622	86	98	10	0

Table 11: Spatiotemporal monthly total max., min., mean, and standard deviation (SD) of the net recharge (*Rn*) in DMHR. The *Rn* is scaled up using the multivariate function from its 3D correlation with *Psat* & *ETsat* with. The values indicate the monthly totals calculated from the daily *Rn* maps. The last row refers to annual averaged *Rn* calculated from the daily *Rn* maps (or the averages of the monthly total *Rn*). All units are in mm month^{-1}.

Hydro. Year	2011 (Oct 2011 to Sept 2012)				2012 (Oct 2012 to Sept 2013)				2013 (Oct 2013 to Sept 2014)			
Month	Max	Min	Ave	SD	Max	Min	Ave	SD	Max	Min	Ave	SD
Oct	65.5	-13.7	0.6	9.2	162.7	-12.4	6.6	15.6	140.6	-10.7	18.6	38.5
Nov	77.4	-3.1	7.0	7.0	121.6	-5.3	8.6	11.7	26.5	-14.7	0.6	2.5
Dec	69.2	-10.6	-0.2	3.1	143.9	-11.6	4.3	14.7	139.7	-17.0	13.9	33.5
Jan	12.7	-10.7	0.8	2.1	236.3	-8.9	13.9	41.7	134.2	-10.9	2.5	8.0
Feb	40.6	-17.1	0.5	3.3	99.5	-9.1	3.7	20.0	200.4	-4.6	17.6	52.7
Mar	35.2	-25.4	-4.4	7.3	294.3	-10.7	12.1	44.1	108.6	-18.8	-8.4	8.2
Apr	169.5	-13.2	5.6	46.8	173.9	-17.0	10.6	29.2	99.7	-18.0	1.4	17.7
May	57.5	-18.6	14.6	48.3	105.7	-21.7	-0.6	25.2	38.5	-25.6	-1.9	27.1
June	22.1	-25.3	-5.9	22.8	10.3	-24.9	-0.5	44.3	25.5	-24.8	-4.2	28.3
Jul	4.3	-26.3	-8.9	11.7	18.3	-26.3	-7.3	20.5	17.4	-26.3	-7.1	19.9
Aug	13.7	-26.3	-10.0	9.9	11.5	-26.3	-8.7	10.6	8.8	-26.3	-9.2	10.7
Sep	54.5	-20.9	-3.6	7.8	39.9	-23.7	-7.4	8.6	39.9	-23.7	-7.4	8.6
Annual Average			-0.3				2.9				1.4	

4.8. Spatiotemporal dynamics of groundwater recharge over the DMHR area.

The net recharge (*Rn*) over the DMHR, i.e., the WLHR in the dehesa (montado), shows a similar pattern but less spatiotemporal distribution as the potential recharge (PR) in this study (compare the PR maps in Fig. 35 to 37 and *Rn* maps Fig. 48 & 49). It is generally higher, in the central east and west parts of the DMHR, where the PR is also higher. Nonetheless, there are also a few unique patterns observed. These variabilities agree to Hagedorn et al. (2011) that says that the spatiotemporal variability of *Rn* at a Catchment scale is caused by rainfall, evapotranspiration, effective porosity & yield of aquifers. Similarly, L. Zhang et al. (2002) says that the accumulation of errors in the measured fluxes in estimating recharge (*Rn* in this case) can lead to large errors in the scaled up recharge. This is because of the complex GW recharge processes that involve hydrogeological and echo-hydrogeological factors among others like slope (topography).

Interestingly, the *Rn* in the study period is spatially and temporally highly variable. The standard deviation, as shown in Table 11 is high. This agrees with the study by Mays (2009) that is mentioned in the previous sections, which says the recharge in semi-arid regions is extremely spatially and temporally variable, at times even the standard deviation exceeding the mean annual recharge. Overall the spatiotemporal mean annual *Rn* shows high variability ranging from –3.9 mm year^{-1} to 35.3 mm year^{-1}. This is within the range of the study by Zomlot *ET* al. (2015), -109 mm year^{-1}and 507 mm year^{-1}.

The non-linearization effect of *ET* on the recharge that is mentioned in section 4.5, is even higher on *Rn* than on PR. For example, the PR in Apr 2012 is > May 2012, while the *Rn* Apr 2012 < may 2012 (Fig. 35b and 48b). This could be due to: (1) time lag for recharge process that ranges from hours or days in shallow ground water with good hydraulic conductivity; (2) uncertainty in the model calibration; and (3) uncertainty in the scaling up function. Another example is that PR Sept 2013 has positive recharge in the majority of the area, and the PR in July and Aug of this year is slightly above 0 mm or negative (Fig. 36a and 49a). However, the *Rn* in Sept 2013 is no different than July & Aug (~0 mm or negative). This could be due to an extended dry period of July and Aug, in which the PR shown in Sept might have been used to saturate the soil or has evaporated.

The dry season (June to Sept) net recharge (*Rn*) ranges from the -16.5 mm year-1 (year 2012) to -24.8 mm year-1 (year 2011). Its contribution to the total annual *Rn* in the whole study period ranges from the highest of -16.5 % of that occurred in the hydrological year 2012 to the lowest of -24.8 % in 2016 (see Table 12). This indicates moisture deficit or no recharge in the DMHR in the dry season. It has been mentioned that the dry season *Rn* in arid and semi-arid environments is negative. Many studies are cognizant to this finding (e.g., Lubczynski and Obakeng, 2004), and interestingly the study in Sardon Catchment by Hassan et al. (2014) shows negative recharge up to -23.4 mm year-1. The dry season *Rn* in the year 2011 is the lowest of all the years in this study because of its lowest *Psat*. However, the *ET* influences it and non-linearizes the coefficient of *P* in expressing the recharge.

The *Rn* in the wet season ranges from 51.8 mm in the hydrological year 2012 to 20.9 mm in the hydrological year 2013. The positive wet season and the negative dry season *Rn* represent distinct seasonal variations of *Rn* in the DMHR. This agrees with the explanations (Shamsudduha, 2009) which says seasonal GW recharge variation is high in shallow aquifers.

Finally, it should be noted that the scaled up *Rn* in the current study gives a good indication of the spatiotemporal dynamics of recharge in the DMHR. Interestingly, it opens options to upgrade it using integrated methods (isotope methods in selected areas, incorporating model results from other sites (than SC), using other additional products of satellite inputs, enhancement with land cover. In addition, the current result may change in the future with a change in climatic, biophysical and socio-economic conditions in the area. Additionally, the recharge in urban areas that is assumed to be zero at the beginning is not adjusted in the final *Rn* maps. This means places within the boundaries of the urban area should be set to zero in the final *Rn* map of the DMHR ((not done in this study). So this can further be upgraded in future studies.

Table 12: Summary of dry and wet season *Rn* in DMHR.

	Hydrological year		
Seasonal *Rn*	2011 (Oct 2011 to Sept 2012)	2012 (Oct 2012 to Sept 2013)	2013 (Oct 2013 to Sept 2014)
Wet season (mm)	20.9	51.8	36.9
% wet season	100.0	100.0	100.0
Dry season (mm)	-24.8	-16.5	-20.5
% Dry season	-6.4	-0.5	-1.2
Over all total (mm)	-3.9	35.3	16.4
Annual average	-0.3	2.9	1.4
SC model annual *Rn*	-90.0	20.9	8.1

The spatial distribution of Rn follows the elevation of the DMHR. This is shown in the elevation and Rn contour maps. The contour interval for elevation & Rn are 250 m and 100 mm yr^{-1} respectively (Fig. 43). The high elevation areas in the central east and central west have higher recharge relative to other parts.

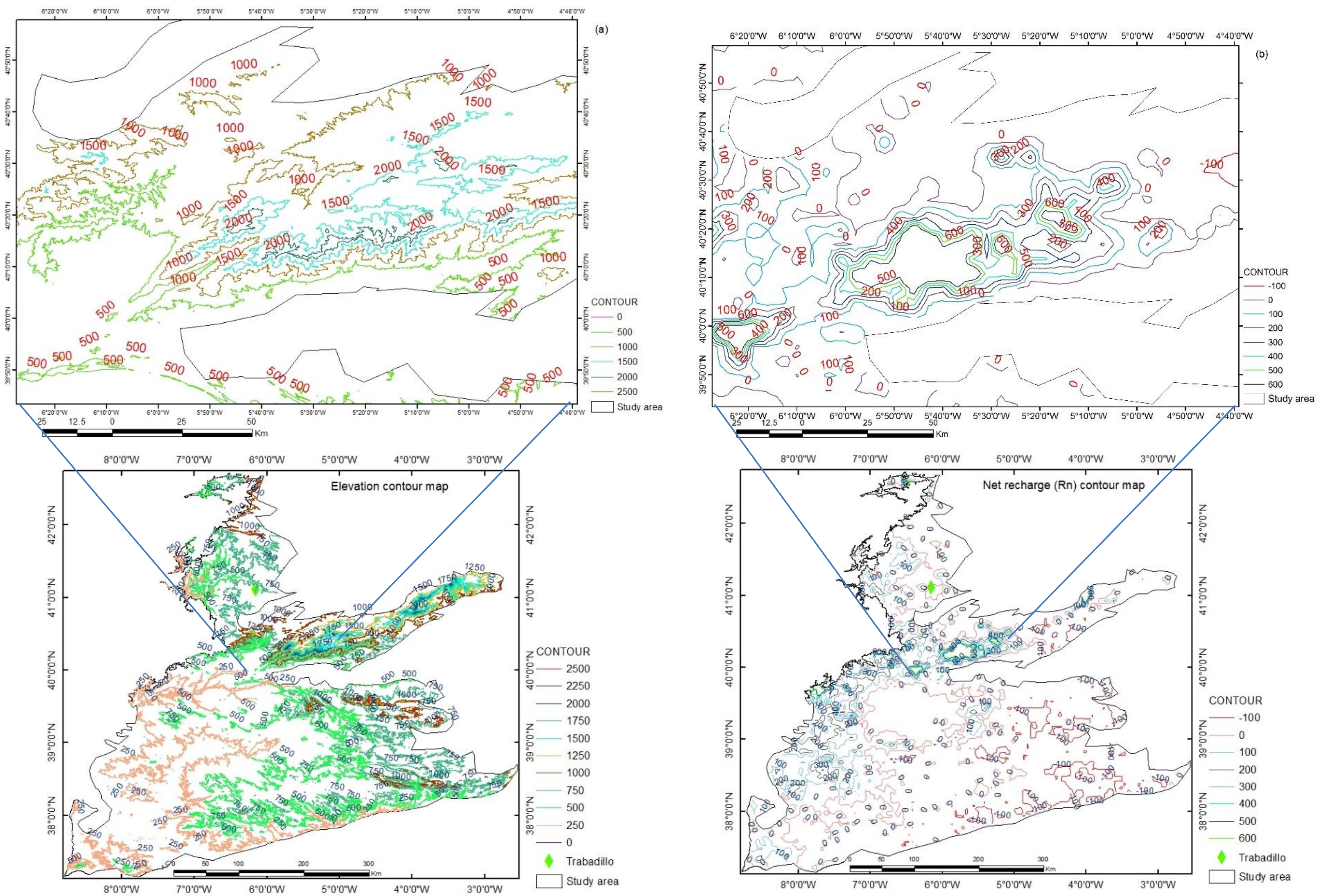

Figure 42: Contour maps of Rn (a) executed at 100 mm interval from the average annual Rn maps of 2011 to 2013 and elevation (b) executed at 250 m interval from the DEM that is downloaded for the IP and clipped to the dehesa (montado) water limited hard rock areas (DMHR). The contours are created in ArcGIS spatial analysis tools.

THIS PAGE IS BLANK

5. CONCLUSION AND RECOMMENDATION

Conclusions

The groundwater recharge dynamics of water limited hard rock systems, like the dehesa (montado) water limited hard rock (DMHR) areas, is complex and prone to changes because of the large spatio-temporal variability in rainfall and evapotranspiration and also large heterogeneity of the medium. Therefore, it is not easily predictable.

An attempt was made to scale the net recharge (*Rn*) from a small area (80 km2) of Sardon Catchment (SC) into a large area (141,430 Km^2) such as the dehesa (montado) hard rock (DMHR) area. The *Rn* of SC was based on transient model calibration and extensive monitoring data, and the scaling up was done by applying *Rn* correlation with remote sensing based CHIRPS rainfall (*Psat*) and evapotranspiration products of LSA-SAF (*ETsat*).

The spatiotemporal *Psat* and *ETsat* in the DMHR, were highly variable within the study period (Oct 2011 to Sept 2014). The *Psat* generally increased from east to west. They were influenced by topographic elevations (through orographic effect in the rainfall forming processes) and movement of frontal winds from the Atlantic Ocean and the Mediterranean Sea. The *ETsat* was high in areas of high rainfall, because of generally large potential evapotranspiration (*PET)*. The dry season *Psat* in the DMHR area was very low (maximum 14.9%), while the *ETsat* was found to be substantial (up to 43.4 %). This caused a negative potential recharge (PR) and negative *Rn* in the dry season. The spatiotemporal PR (*Psat* - *ETsat*) and *Rn* were high where rainfall was high and evapotranspiration low.

The daily *Rn* of SC model solution showed high spatiotemporal variability with *Rn* interchanging between slightly positive or slightly negative values, depending on the season and related PR, as it is expected in arid and semi-arid environments. In that model solution, it was critical to apply spatiotemporally variable input fluxes as driving forces, instead of spatiotemporally invariant input fluxes used in former model solution.

The linear regressions between *Rn* of the SC and *Psat* and *ETsat* of DMHR area (applying different flux inputs and time scales) at the daily or decade time scale was poor; the best linear regression was obtained for monthly correlations of Rn and Psat (R^2 = 0.54). The improvement of R^2 with increase in time scale indicates presence of substantial time lag required for the rainfall to reach the groundwater.

The best correlation result between *Rn* of the SC and the remote sensing input fluxes at different time scales was obtained with the multivariate regression function (R^2 = 0.63) of the *Rn* with the Psat and ETsat at a daily scale. That function was finally used for daily scaling up of *Rn* from SC into DMHR area. The function has resulted, however, uncertainties of estimate when the rainfall amount is >~40 mm day^{-1}. Luckily enough, extreme rainfall days occur very rarely in very limited areas. These extreme values are observed in few pixels (a max of 5% except for 1 month that was 10%) in a few months, so the result is acceptable.

The spatiotemporal dynamics of groundwater recharge in the DMHR area is highly variable and not easily predictable owing to the semi-arid climate of the DMHR area. The maximum *Rn* in the central western and central eastern part of the DMHR area comprising the Tagus Basin, is due to high rainfall in the area in contrast to the southern parts where *Psat* is low and *ETsat* relatively high so the *Rn* is low. The dry season contribution of the *Rn* ranging from -28.4 mm to -23.9 mm (as well as PR ranging from 15.9 mm to -38.6 mm), indicates deficit in the groundwater balance in that season. Moreover, the overall low annual *Rn* (from 35.3 mm year^{-1} to -3.9 mm yr^{-1}) gives an indication of low groundwater replenishment in the DMHR area. In this regard, DMHR area can be susceptible to drought, particularly because of highly variable climate and relatively low storage capacity of hard rocks. Therefore, careful management of the existing groundwater resource is necessary.

Recommendations

The results of this research have revealed the complex, spatio-temporal dynamics of groundwater recharge in DMHR area. The following recommendations are made to further the findings in this study in the future.

- The net recharge (*Rn*) scaled up over the DMHR in this study can be further enriched by classifying the area into recharge zones based on lithology, slope, aspect, land cover, and rainfall intensities that are prevalent in the different parts of the DMHR area. In this regard, the spatial distribution of the *Rn* can be enhanced by assigning weighting factors.
- The result from this study should be integrated with recharge estimate from other techniques. For example, recharge estimates from chloride method and isotopes can be used as calibration of the result of this study.
- In order to make predictions and future forecasts of the *Rn* dynamics at the DMHR area, the upscaling should be done for larger number of years.
- The present study should be enhanced applying additional rainfall (*P*) and evapotranspiration for extended number of years. Additional source of data for P can be from *in-situ* data and combined use of remote sensing rainfall products. Similarly, additional *ET* can be found from *in-situ* data and surface energy balance methods. It should be noted also 10 years (2007 to 2016) *Psat* data and 6 years (2011 to 2016) *ETsat* is already collected in this study. However, the *Rn*.is scaled up from 2011 to 2014 because the SC model is simulated with spatiotemporal data for these years.
- The SC model should be simulated with spatiotemporal data (like it is simulated from 2011 to 2013 in this study and for 2014 by former colleague) for additional number of years (10 years for example), so that *Rn* is scaled up for long duration increases reliability of the present results.
- The recharge in urban areas (assumed to be zero at the beginning) should be constrained to zero in the final *Rn* map of the DMHR by applying conditional statements in GIS or MATLAB taking the boundary maps of the urban areas in the DMHR.
- Results from other surface models like the Gash model are helpful to include rainfall intensity and canopy storage in the computation of interception.

LIST OF REFERENCES

Abera, W., Brocca, L., Rigon, R., 2016. Comparative evaluation of different satellite rainfall estimation products and bias correction in the Upper Blue Nile (UBN) basin. Atmos. Res. 178–179, 471–483. doi:10.1016/j.atmosres.2016.04.017

Albaugh, J., Dye, P., King, J., 2013. Eucalyptus and water use in SA. J. For. Res. 2013, 1–11. doi:10.1155/2013/852540

Alemseged, T.H. and Rientjes, T.H.M., 2015. Evaluation of regional climate model simulations of rainfall over the Upper Blue Nile basin. Atmos. Res. 161–162, 57–64. doi:10.1016/j.atmosres.2015.03.013

Anderson, M.P., Woessner, W.W., 1992. Applied Groundwater Modeling : Simulation of Flow and Advective Transport. URL http://ezproxy.utwente.nl:2201/

Anderson, M.P., Woessner, W.W., Hunt, R.J., 2015. Applied Groundwater Modeling : Simulation of Flow and Advective Transport. Elsevier Science, San Diego.

Arora, V.K., 2002. The use of the aridity index to assess climate change effect on\rannual runoff. J. Hydrol. 265, 164–177.

Basist, A., Bell, G.D., Meentemeyer, V., Rotach, M.W., Zardi, D., Skamarock, W.C., Klemp, J.B., 1994. On the boundary-layer structure over highly complex terrain: Key findings from MAP. J. Comput. Phys. doi:10.1175/1520-0442(1994)007<1305:SRBTAP>2.0.CO;2

Bhatti, H., Rientjes, T., Haile, A., Habib, E., Verhoef, W., 2016. Evaluation of Bias Correction Method for Satellite- Based Rainfall Data. Sensors 16, 884. doi:10.3390/s16060884

Brunner, P., Bauer, P., Eugster, M., Kinzelbach, W., 2004. Using remote sensing to regionalize local precipitation recharge rates obtained from the Chloride Method. J. Hydrol. 294, 241–250. doi:10.1016/j.jhydrol.2004.02.023

C. Bhuiyan Æ Ramesh P. Singh Æ W. A. Flügel, 2016. Modelling of ground water recharge-potential in the hard-rock Aravalli terrain, India: a GIS approach. Env. Earth Sci.

Campos, P., Huntsinger, L., L.Oviedo, J., F.Starrs, P., Daìz, M., B.Standiford, R., 2013. Mediterranean Oak Woodland Working Landscapes Dehesas of Spain and Ranchlands of California. Springer Verlag.

Chen, X., Huang, Y., Ling, M., Hu, Q., Liu, B., 2012. Numerical modeling groundwater recharge and its implication in water cycles of two interdunal valleys in the Sand Hills of Nebraska. Phys. Chem. Earth 53–54, 10–18. doi:10.1016/j.pce.2011.08.022

Chen, X., Su, Z., Ma, Y., Liu, S., Yu, Q., Xu, Z., 2014. Development of a 10-year (2001-2010) 0.1° data set of land-surface energy balance for mainland China. Atmos. Chem. Phys. doi:10.5194/acp-14-13097-2014

Chen, X., Su, Z., Ma, Y., Yang, K., Wang, B., 2013. Estimation of surface energy fluxes under complex terrain of Mt. Qomolangma over the Tibetan Plateau. Hydrol. Earth Syst. Sci. 17, 1607–1618. doi:10.5194/hess-17-1607-2013

Chu, H., 2012. Assessing the relationships between elevation and extreme precipitation with various durations in southern Taiwan using spatial regression models. Hydrol. Process. 26, 3174–3181. doi:10.1002/hyp.8403

Costa, A., Madeira, M., Lima Santos, J., Oliveira, Â., 2011. Change and dynamics in Mediterranean evergreen oak woodlands landscapes of Southwestern Iberian Peninsula. Landsc. Urban Plan. 102, 164–176. doi:10.1016/j.landurbplan.2011.04.002

Custodio, E., Andreu-Rodes, J.M., Aragón, R., Estrela, T., Ferrer, J., García-Aróstegui, J.L., Manzano, M., Rodríguez-Hernández, L., Sahuquillo, A., del Villar, A., 2016. Groundwater intensive use and mining in south-eastern peninsular Spain: Hydrogeological, economic and social aspects. Sci. Total Environ. 559, 302–316. doi:10.1016/j.scitotenv.2016.02.107

Dzikiti, S., Gush, M.B., Le Maitre, D.C., Maherry, A., Jovanovic, N.Z., Ramoelo, A., Cho, M.A., 2016. Quantifying potential water savings from clearing invasive alien Eucalyptus camaldulensis using in situ and high resolution remote sensing data in the Berg River Catchment, Western Cape, South Africa. For. Ecol. Manage. 361, 69–80. doi:10.1016/j.foreco.2015.11.009

Fernández-Montes, S., Gómez-Navarro, J.J., Rodrigo, F.S., García-Valero, J.A., Montávez, J.P., 2015. Covariability of seasonal temperature and precipitation over the Iberian Peninsula in high-resolution regional climate simulations (1001-2099). Glob. Planet. Change. doi:10.1016/j.gloplacha.2016.09.007

Fernández-Montes, S., Seubert, S., Rodrigo, F.S., Rasilla Álvarez, D.F., Hertig, E., Esteban, P., Philipp, A., 2014. Circulation types and extreme precipitation days in the Iberian Peninsula in the transition seasons: Spatial links and temporal changes. Atmos. Res. 138, 41–58.

doi:10.1016/j.atmosres.2013.10.018
Fernández, R.D., Pereira, M.F., 2016. Extensional orogenic collapse captured by strike-slip tectonics: Constraints from structural geology and U[sbnd]Pb geochronology of the Pinhel shear zone (Variscan orogen, Iberian Massif). Tectonophysics 691, 290–310. doi:10.1016/j.tecto.2016.10.023
Francés, A.P., Lubczynski, M.W., Roy, J., Santos, F.A.M., Mahmoudzadeh Ardekani, M.R., 2014. Hydrogeophysics and remote sensing for the design of hydrogeological conceptual models in hard rocks - Sardón catchment (Spain). J. Appl. Geophys. 110, 63–81. doi:10.1016/j.jappgeo.2014.08.015
García-Barrón, L., Camarillo, J.M., Morales, J., Sousa, A., 2015. Temporal analysis (1940-2010) of rainfall aggressiveness in the Iberian Peninsula basins. J. Hydrol. 525, 747–759. doi:10.1016/j.jhydrol.2015.04.036
Gebregiorgis, A.S., Tian, Y., Peters-Lidard, C.D., Hossain, F., 2012. Tracing hydrologic model simulation error as a function of satellite rainfall estimation bias components and land use and land cover conditions. Water Resour. Res. 48. doi:10.1029/2011WR011643
Gemitzi, A., Ajami, H., Richnow, H.-H., 2017. Developing empirical monthly groundwater recharge equations based on modeling and remote sensing data – Modeling future groundwater recharge to predict potential climate change impacts. J. Hydrol. 546, 1–13. doi:http://dx.doi.org/10.1016/j.jhydrol.2017.01.005
Guber, A., Gish, T., Pachepsky, Y., McKee, L., Nicholson, T., Cady, R., 2011. Event-based estimation of water budget components using a network of multi-sensor capacitance probes. Hydrol. Sci. J. 56, 1227–1241. doi:10.1080/02626667.2011.609485
Habib, E., Haile, A., Sazib, N., Zhang, Y., Rientjes, T., 2014. Effect of Bias Correction of Satellite-Rainfall Estimates on Runoff Simulations at the Source of the Upper Blue Nile. Remote Sens. 6, 6688–6708. doi:10.3390/rs6076688
Hagedorn, B., El-Kadi, A.I., Mair, A., Whittier, R.B., Ha, K., 2011. Estimating recharge in fractured aquifers of a temperate humid to semiarid volcanic island (Jeju, Korea) from water table fluctuations, and Cl, CFC-12 and 3H chemistry. J. Hydrol. 409, 650–662. doi:10.1016/j.jhydrol.2011.08.060
Haile, A.T., Habib, E., Rientjes, T., 2013. Evaluation of the climate prediction center (CPC) morphing technique (CMORPH) rainfall product on hourly time scales over the source of the Blue Nile River. Hydrol. Process. 27, 1829–1839. doi:10.1002/hyp.9330
Hassan, S.M.T., Lubczynski, M.W., Niswonger, R.G., Su, Z., 2014. Surface–groundwater interactions in hard rocks in Sardon Catchment of western Spain: An integrated modeling approach. J. Hydrol. 517, 390–410. doi:10.1016/j.jhydrol.2014.05.026
Healy, R.W., Scanlon, B.R., 2012. Estimating groundwater recharge. Cambridge University Press, Cambridge; New York.
Healy, R.W., Scanlon, B.R., 2010. Estimating groundwater recharge. Cambridge University Press, Cambridge.
Herrmann, F., Baghdadi, N., Blaschek, M., Deidda, R., Duttmann Rainer, Jeunesse, L.I., Sellami Haykel, Vereecken Harry, Wendland Frank, 2015a. Simulation of future groundwater recharge using a climate model ensemble and SAR-image based soil parameter distributions - A case study in an intensively-used Mediterranean catchment. Sci. Total Environ. 543, 889–905. doi:10.1016/j.scitotenv.2015.07.036
Herrmann, F., Keller, L., Kunkel, R., Vereecken, H., Wendland, F., 2015b. Determination of spatially differentiated water balance components including groundwater recharge on the Federal State level – A case study using the mGROWA model in North Rhine-Westphalia (Germany). J. Hydrol. Reg. Stud. 4, 294–312. doi:10.1016/j.ejrh.2015.06.018
Hill, M., 1998. Methods and guidelines for effective model calibration: US Geological Survey Water-Resources Investigations Report 98-4005, 90 p. US Geol. Surv. Resour. Investig. Rep. 98-4005 1–98.
Izquierdo, T., 2014. Conceptual hydrogeological model and aquifer system classification of a small volcanic island (La Gomera; Canary Islands). Catena 114, 119–128. doi:10.1016/j.catena.2013.11.006
Krásný, J., Sharp, J.M., 2007. Groundwater in Fractured Rocks : IAH Selected Paper Series, volume 9. CRC Press, Independence.
Kusangaya, S., Toucher, M.L.W., van Garderen, E.A., Jewitt, G.P.W., 2016. An evaluation of how downscaled climate data represents historical precipitation characteristics beyond the means and variances. Glob. Planet. Change 144, 129–141. doi:10.1016/j.gloplacha.2016.07.014
Lobera, G., Besné, P., Vericat, D., López-Tarazón, J.A., Tena, A., Aristi, I., Díez, J.R., Ibisate, A., Larrañaga, A., Elosegi, A., Batalla, R.J., 2015. Geomorphic status of regulated rivers in the Iberian Peninsula. Sci. Total Environ. 508, 101–114. doi:10.1016/j.scitotenv.2014.10.058

Lubczynski, M.W., Gurwin, J., 2005. Integration of various data sources for transient groundwater modeling with spatio-temporally variable fluxes - Sardon study case, Spain. J. Hydrol. 306, 71–96. doi:10.1016/j.jhydrol.2004.08.038
Lubczynski, M.W., Obakeng, O.T., 2004. Monitoring and modeling of fluxes on Kalahari – setup and strategy of the Kalahari Monitoring project . Serowe study case 271–278.
Macdonald, D.M.J., Edmunds, W.M., 2014. Estimation of groundwater recharge in weathered basement aquifers, southern Zimbabwe; a geochemical approach. Appl. Geochemistry 42, 86–100. doi:10.1016/j.apgeochem.2014.01.003
Mahmoudzadeh, M.R., Francés, A.P., Lubczynski, M., Lambot, S., 2012. Using ground penetrating radar to investigate the water table depth in weathered granites - Sardon case study, Spain. J. Appl. Geophys. 79, 17–26. doi:10.1016/j.jappgeo.2011.12.009
Mays, L.W., 2009. Integrated urban water management : arid and semi-arid regions.
Mohammadi, Z., Salimi, M., Faghih, A., 2014. Assessment of groundwater recharge in a semi-arid groundwater system using water balance equation, southern Iran. J. African Earth Sci. 95, 1–8. doi:10.1016/j.jafrearsci.2014.02.006
Moon, S.K., Woo, N.C., Lee, K.S., 2004. Statistical analysis of hydrographs and water-table fluctuation to estimate groundwater recharge. J. Hydrol. 292, 198–209. doi:10.1016/j.jhydrol.2003.12.030
Moreno, A., Pérez, A., Frigola, J., Nieto-Moreno, V., Rodrigo-Gámiz, M., Martrat, B., González-Sampériz, P., Morellón, M., Martín-Puertas, C., Corella, J.P., Belmonte, Á., Sancho, C., Cacho, I., Herrera, G., Canals, M., Grimalt, J.O., Jiménez-Espejo, F., Martínez-Ruiz, F., Vegas-Vilarrúbia, T., Valero-Garcés, B.L., 2012. The Medieval Climate Anomaly in the Iberian Peninsula reconstructed from marine and lake records. Quat. Sci. Rev. 43, 16–32. doi:10.1016/j.quascirev.2012.04.007
Mortimer, L., Aydin, A., Simmons, C.T., Love, A.J., 2011. Is in situ stress important to groundwater flow in shallow fractured rock aquifers? J. Hydrol. 399, 185–200. doi:10.1016/j.jhydrol.2010.12.034
Nosetto, M.D., Jobbágy, E.G., Brizuela, A.B., Jackson, R.B., 2012. The hydrologic consequences of land cover change in central Argentina. Agric. Ecosyst. Environ. 154, 2–11. doi:10.1016/j.agee.2011.01.008
Obakeng, O.T., de Vries, J.J. promoto., Lubczynski, M.W. promoto., 2007. Soil moisture dynamics and evapotranspiration at the fringe of the Botswana Kalahari, with emphasis on deep rooting vegetation, ITC Dissertation;141.
Picos, M., Formation, D.E., 2008. Carboniferous of the cantabrian zone.
Posada, B.O., 2016. Landscapes and Landforms of Spain. doi:10.1007/978-3-319-11800-0
Reyes-Acosta, J.L., Lubczynski, M.W., 2013. Mapping dry-season tree transpiration of an oak woodland at the catchment scale, using object-attributes derived from satellite imagery and sap flow measurements. Agric. For. Meteorol. 174–175, 184–201. doi:http://dx.doi.org/10.1016/j.agrformet.2013.02.012
Rodriguez-Puebla, C., Encinas, a H., Nieto, S., Garmendia, J., 1998. Spatial and temporal patterns of annual precipitation variability over the Iberian Peninsula. Int. J. Climatol. 18, 299–316. doi:10.1002/(SICI)1097-0088(19980315)18:3<299::AID-JOC247>3.0.CO;2-L
Rodríguez-Suárez, J.A., Soto, B., Perez, R., Diaz-Fierros, F., 2011. Influence of Eucalyptus globulus plantation growth on water table levels and low flows in a small catchment. J. Hydrol. 396, 321–326. doi:10.1016/j.jhydrol.2010.11.027
Rossman, N.R., Zlotnik, V.A., Rowe, C.M., Szilagyi, J., 2014. Vadose zone lag time and potential 21st century climate change effects on spatially distributed groundwater recharge in the semi-arid Nebraska Sand Hills. J. Hydrol. 519, 656–669. doi:10.1016/j.jhydrol.2014.07.057
S., H.S.G., Liu, C.W., 2000. Estimation of the effective precipitation recharge coefficient in an unconfined aquifer using stochastic analysis. Hydrol. Process. 14, 811–830.
Salvati, L., Zitti, M., Di Bartolomei, R., Perini, L., 2013. Climate Aridity under Changing Conditions and Implications for the Agricultural Sector: Italy as a Case Study. Geogr. J. 2013, 1–7.
Santisteban, J.I., Schulte, L., 2007. Fluvial networks of the Iberian Peninsula: a chronological framework. Quat. Sci. Rev. 26, 2738–2757. doi:10.1016/j.quascirev.2006.12.019
Shamsudduha, 2009. Recent trends in groundwater levels in a highly seasonal hydrological system: the Ganges-Brahmaputra-Meghna Delta. Hydrol. Earth Syst. Sci. 13, 2373–2385. doi:10.5194/hessd-6-4125-2009
Sharp, J.M., Troeger, U., 2014. Fractured Rock Hydrogeology. CRC Press, London.
Shevlyakov, G.L., Oja, H., 2016. Robust correlation : theory and applications.
Soheili, M., 2014. Groundwater Modelling For Recharge Estimation Using Satellite Based

Evapotranspiration. Salland Case, The Netherlands. MSc Def. ITC. doi:10.13140/2.1.4917.3760
Su, Z., Fernández-Prieto, D., Timmermans, J., Chen, X., Hungershoefer, K., Roebeling, R., Schröder, M., Schulz, J., Stammes, P., Wang, P., Wolters, E., 2014. First results of the earth observation Water Cycle Multi-mission Observation Strategy (WACMOS). Int. J. Appl. Earth Obs. Geoinf. 26, 270–285. doi:10.1016/j.jag.2013.08.002
Sumner, G., Homar, V., Ramis, C., 2001. Precipitation Seasonality in Eastern and Southern Coastal Spain. Int. J. Climatol. Int. J. Clim. 21, 219–247.
Thivya, C., Chidambaram, S., Rao, M.S., Gopalakrishnan, M., Thilagavathi, R., Prasanna, M. V., Nepolian, M., 2016. Identification of Recharge Processes in Groundwater in Hard Rock Aquifers of Madurai District Using Stable Isotopes. Environ. Process. 3, 463–477. doi:10.1007/s40710-016-0137-3
Tian, Y., Peters-Lidard, C.D., Eylander, J.B., Joyce, R.J., Huffman, G.J., Adler, R.F., Hsu, K.L., Turk, F.J., Garcia, M., Zeng, J., 2009. Component analysis of errors in Satellite-based precipitation estimates. J. Geophys. Res. Atmos. 114, 1–15. doi:10.1029/2009JD011949
Timmermans, W.J., Kustas, W.P., Anderson, M.C., French, A.N., 2007. An intercomparison of the Surface Energy Balance Algorithm for Land (SEBAL) and the Two-Source Energy Balance (TSEB) modeling schemes. Remote Sens. Environ. 108, 369–384. doi:10.1016/j.rse.2006.11.028
Trang, N.T.T., Shrestha, S., Shrestha, M., Datta, A., Kawasaki, A., 2017. Evaluating the impacts of climate and land-use change on the hydrology and nutrient yield in a transboundary river basin: A case study in the 3S River Basin (Sekong, Sesan, and Srepok). Sci. Total Environ. 576, 586–598. doi:10.1016/j.scitotenv.2016.10.138
USGS GWRP: Methods for Estimating Ground-Water Recharge In Humid Regions, 2016. URL http://water.usgs.gov/ogw/gwrp/methods/ (accessed 5.23.16).
V, E.S.P.B., 1984. Evapotranspiration from a Eucalyptus 8, 41–56.
Vázquez-Vílchez, M., Jabaloy-Sánchez, A., Azor, A., Stuart, F., Persano, C., Alonso-Chaves, F.M., Martín-Parra, L.M., Matas, J., García-Navarro, E., 2015. Mesozoic and Cenozoic exhumation history of the SW Iberian Variscides inferred from low-temperature thermochronology. Tectonophysics 663, 110–121. doi:10.1016/j.tecto.2015.06.034
Walsh, R.P.D., Lawler, D.M., 1981. Rainfall Seasonality: Description, Spatial Patterns and Change Through Time. Weather 36, 201–208. doi:10.1002/j.1477-8696.1981.tb05400.x
Wang, H., Gao, J.E., Zhang, M., Li, X., Zhang, S., Jia, L., 2015. Effects of rainfall intensity on groundwater recharge based on simulated rainfall experiments and a groundwater flow model. Catena 127, 80–91. doi:10.1016/j.catena.2014.12.014
Wang, T., Franz, T.E., Yue, W., Szilagyi, J., Zlotnik, V.A., You, J., Chen, X., Shulski, M.D., Young, A., 2016. Feasibility analysis of using inverse modeling for estimating natural groundwater recharge from a large-scale soil moisture monitoring network. J. Hydrol. 533, 250–265. doi:10.1016/j.jhydrol.2015.12.019
Webster, R., Oliver, M.A., 2008. Geostatistics for Environmental Scientists: . John Wiley & Sons Ltd.
Weldemichael, M.Y., 2016. Integrated numerical model applying stratiform hydrogeological conceptual model, Sardon catchment study case, Spain.
Wheater, H., Sorooshian, S., Sharma, K.D., 2008. Hydrological modelling in arid and semi-arid areas. Cambridge University Press, Cambridge.
Whittecar, G.R., Dobbs, K.M., Stone, S.A., McLeod, J.M., Thornton, T.L., Smith, J.C., 2016. Use of the Effective Monthly Recharge model to assess long-term water-level fluctuations in and around groundwater-dominated wetlands. Ecol. Eng. 99, 462–472. doi:10.1016/j.ecoleng.2016.11.038
Yong, B., Chen, B., Tian, Y., Yu, Z., Hong, Y., 2016. Error-component analysis of TRMM-based Multi-Satellite Precipitation Estimates over mainland China. Remote Sens. 8. doi:10.3390/rs8050440
Zhang, L., Walker, G.R., Fleming, M., 2002. Surface Water Balance for Recharge Estimation - Part 9.
Zhang, X., Sanderson, D.J., Sanderson, D.J., 2002. Numerical Modelling and Analysis of Fluid Flow and Deformation of Fractured Rock Masses. Elsevier Science, Amsterdam.
Zomlot, Z., Verbeiren, B., Huysmans, M., Batelaan, O., Canone, D., Previati, M., Bevilacqua, I., Salvai, L., Ferraris, S., 2015. Journal of Hydrology : Regional Studies Spatial distribution of groundwater recharge and base flow : Assessment of controlling factors 4, 349–368.